

Multistage Nanoparticle Delivery System for Deep Penetration into Solid Tumor and Electrically Controlled Catalytic Nanowire Growth

By

Cliff R. Wong

B.S. Physics and B.S. Electrical Engineering
Rice University, Houston, 2005

Submitted to the Department of Chemistry
in Partial Fulfillment of the Requirements for the Degree of

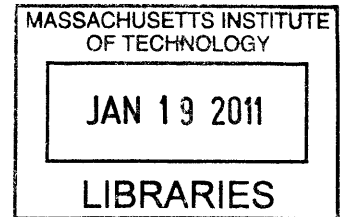
DOCTOR OF PHILOSOPHY

at the


MASSACHUSETTS INSTITUTE OF TECHNOLOGY

February 2011


@ 2011 MASSACHUSETTS INSTITUTE OF TECHNOLOGY
All Rights Reserved




ARCHIVES

Signature of Author 

.....
Department of Chemistry
September 21, 2010

Certified by..... 

.....
Mounji Bawendi
Department of Chemistry
Thesis Supervisor

Accepted by..... 

.....
Robert Field
Chairman, Department Committee on Graduate Students

This doctoral thesis has been examined by a committee of the Department of Chemistry as follows:

Professor Andrei Tokmakoff

Chairman

Professor Mounji G. Bawendi

Thesis Supervisor

Professor Keith Nelson

Multistage Nanoparticle Delivery System for Effective Transport to Solid Tumor and Electrically Controlled Catalytic Nanowire Growth

By

Cliff R. Wong

Submitted to the Department of Chemistry on September 21, 2010 in Partial Fulfillment of the Requirements for the Degree of Doctor of Philosophy in Chemistry

ABSTRACT

Assembly of functional nanocomponents offers promising applications in drug delivery to solid tumors and bottom-up synthesis and integration of nanodevices. This thesis presents a novel multistage nanoparticle delivery system consisting of an assembly of nanoparticles that can change its size to facilitate transport into solid tumors. Current FDA-approved nanotherapeutics, which function based on the enhanced permeation and retention (EPR) effect, suffer from poor penetration into the extravascular regions of the tumor due to the dense collagen matrix, resulting in heterogeneous therapeutic effects and likely contributing to tumor regression and development of resistance. We propose a multistage nanoparticle system that “shrinks” when it extravasates into the tumor and is exposed to the tumor microenvironment, allowing enhanced penetration into the tumor parenchyma. This “shrinkage” is preferentially triggered in the tumor through cleavage by MMPs, proteases highly expressed in the tumor microenvironment. A multistage nanoparticle system allows us to engineer the size and surface properties of each stage independently for preferential transvascular transport into tumors and high diffusion in the tumor’s interstitial space. To our knowledge, this work is the first demonstration of a size-changing nanoparticle delivery system *in vivo*. Multistage nanoparticle delivery systems provide a promising approach to improving the delivery of anticancer agents into solid tumors and as a result the enhancement of the drug’s therapeutic efficacy.

Another area that necessitates the controlled assembly of nanocomponents is in the integration of nanodevices and nanocircuitry. We have developed a method of combining the synthesis and assembly of semiconducting nanowires in a single step using electrically controlled catalytic nanowire growth. Our results demonstrate electric field-modulated nanowire growth that can be used as a simple and inexpensive method for fabricating and integrating nanoscale devices.

Thesis Supervisor: Mounji G. Bawendi, Ph.D.

Title: Lester Wolfe Professor in Chemistry

for family and friends

Table of Contents

Title Page	1
Signature Page.....	3
Abstract	5
Dedication	7
Table of Contents.....	9
List of Figures.....	13
Chapter 1 Introduction	17
1.1 Tumor Biology	17
1.2 Cancer Therapy.....	22
1.3 Drug Transport in Solid Tumors.....	26
1.3.1 Tumor vasculature	26
1.3.2 Transvascular transport	27
1.3.3 Interstitial Transport	29
1.4 Nanomedicine for Cancer Therapy	31
1.5 Multistage Nanoparticle Delivery System.....	36
1.6 Quantum Dots in Biological Applications.....	39
1.6.1 Basic Properties	39
1.6.2 Synthesis and Characterization.....	41
1.6.3 Water-Solubilization Strategies	43
1.6.4 Bio-Conjugation Strategies.....	46
1.7 References.....	47
2. Synthesis and Characterization of Size-Changing Nanoparticle Constructs	51
2.1 Introduction.....	51
2.2 Materials and Methods.....	52
2.2.1 Materials.....	52
2.2.2 Synthesis of DHLA-PEG QD Peptide Silica Nanoparticles	53
2.2.3 Synthesis of DHLA-PEG QD Gelatin Nanoparticles.....	54
2.2.4 Synthesis of Imidazole-PEG QD encapsulated Gelatin Nanoparticles.....	56

2.2.5 Synthesis of Imidazole-PEG QD coated Gelatin Nanoparticles.....	56
2.2.6 Synthesis of Polyacrylic Acid-PEG QD-Peptide-Gelatin Nanoparticles.....	58
2.2.7 Synthesis of Polyacrylic Acid-PEG QD Gelatin Nanoparticles	59
2.2.8 Size Measurement	61
2.2.9 Zeta Potential.....	61
2.2.10 Fluorescence	62
2.3.11 Gel Filtration Chromatography (GFC).....	62
2.3.12 Fluorescence Correlation Spectroscopy (FCS)	62
2.3 Results and Discussion	63
2.3.1 DHLA-PEG QD Peptide Silica Nanoparticles.....	63
2.3.2 DHLA-PEG QD Gelatin Nanoparticles	66
2.3.3 Imidazole-PEG QD encapsulated Gelatin Nanoparticles	70
2.3.4 Imidazole-PEG QD coated Gelatin Nanoparticles	71
2.3.5 Polyacrylic Acid QD-Peptide-Gelatin Nanoparticles.....	73
2.3.6 Polyacrylic Acid-PEG QD Gelatin Nanoparticles.....	74
3.4 References.....	80
3. <i>In Vitro</i> and <i>In Vivo</i> Characterization of Size-Changing Nanoparticle	83
3.1 Introduction.....	83
3.2 Materials and Methods.....	83
3.2.1 Materials.....	83
3.2.2. Gel Filtration Chromatography (GFC).....	84
3.2.3 Fluorescence Correlation Spectroscopy (FCS).	85
3.2.4 ICP-OES.	86
3.2.5 XPS.....	87
3.2.6. <i>In Situ</i> Zymography.....	87
3.2.7 Collagen Gel Diffusion.	88
3.2.8 Intravital Multiphoton Microscopy	89
3.2.9 Blood half-life.....	90
3.3 Results	91
3.4 Discussion.....	110
3.5 References.....	114
4. Electrically Controlled Catalytic Growth of Nanowires.....	117

4.1 Introduction.....	117
4.2 Materials and Methods.....	119
4.2.1 Materials.....	119
4.2.2 Experimental Setup.....	120
4.2.3 Nanowire Synthesis.....	122
4.3 Results and Discussion	122
4.4 References.....	132

List of Figures

Fig. 1.1: Schematic depiction of the multistage nanoparticle drug delivery system	38
Fig. 2.1: Synthetic scheme for DHLA-PEG QD Gelatin Nanoparticles	55
Fig. 2.2: Synthetic scheme for Polyacrylic Acid-PEG QD Gelatin Nanoparticles	59
Fig. 2.3: Gel-Filtration Chromatograms of DHLA-PEG QD Peptide Silica NPs	65
Fig. 2.4: Physical characterization of DHLA-PEG QD Gelatin NPs	68
Fig. 2.5: SEM of DHLA-PEG QD Gelatin NPs	69
Fig. 2.6: Centrifugation of DHLA-PEG Gelatin NP after collagenase.	69
Fig. 2.7: GFC chromatograms of DHLA-PEG QD and Imidazole QD with 95% FBS	70
Fig. 2.8: Schematic depiction of the multistage nanoparticle drug delivery system	71
Fig. 2.9: FCS of Imidazole-PEG QD Gelatin NPs after collagenase	72
Fig. 2.10: GFC of PA Acid-PEG QD Gelatin NPs with grade X glut. after collagenase	75
Fig. 2.11: UV absorption spectra of different grades of glutaraldehyde	77
Fig. 2.12: GFC of PA Acid-PEG QD Gelatin NPs with grade 1:2 glut. after collagenase.....	78
Fig. 2.13: Comparison of size and size change with different grades of glutaraldehyde	79
Fig. 3.1: Experimental setup for intratumoral injection	89
Fig. 3.2: QDGelNP physical and <i>in vitro</i> characterization.	92
Fig. 3.3: DLS size and zeta potential distributions of QDGelNPs and QDs.....	93
Fig. 3.4: High resolution XPS spectra of C1s region for QDGelNPs after PEGylation.....	94
Fig. 3.5: Colloidal stability of QDGelNPs.....	95
Fig. 3.6: GFC of QDGelNPs and QDGelNPs incubated with MMP-2	97
Fig. 3.7: GFC of QDGelNPs and QDGelNPs incubated with FBS	98
Fig. 3.8: Kinetics of MMP-2 induced QD release from QDGelNPs.....	99
Fig. 3.9: FCS cross-correlograms of QDGelNPs before and after MMP-2.....	100
Fig. 3.10: Diffusion of SilicaQDs and QDGelNPs in collagen gel.....	102
Fig. 3.11: Diffusion of QD in collagen gel	103
Fig. 3.12: Particle distribution and SHG at interface of collagen gel experiment.....	103
Fig. 3.13: <i>In situ</i> zymography of gelatinase enzymatic activity in HT-1080 and 4T1	105
Fig. 3.14 <i>In vivo</i> images of QDGelNPs and SilicaQDs after intratumoral.....	106

Fig. 3.15: Heat map of QDGeINP and SilicaQD distributions after intratumoral co-injection .	107
Fig. 3.16: Radial intensity profiles of QDGeINP after intratumoral injection.....	108
Fig. 3.17: Blood concentration of QDGeINPs and SilicaQDs	109
Fig. 4.1: Schematic of the experimental setup for electrically controlled wire growth.....	120
Fig. 4.2: SEM images of 20 nm Bi layers thermally evaporated onto Pt electrodes.....	121
Fig. 4.3: Voltage and electric-field dependence of CdSe-nanowire growth.....	121
Fig. 4.4: Morphology and crystal structure of CdSe nanowires grown by electrical excitation	123
Fig. 4.5: Morphology and crystal structure of CdSe nanowires	124
Fig. 4.6: High-resolution TEM images of CdSe wires	125
Fig. 4.7: Elemental analysis of a wire with STEM.....	127
Fig. 4.8: CdSe wires grown off bismuth layers with different thicknesses	127
Fig. 4.9: CdSe wires grown on a substrate with a conducting back gate	130
Fig. 4.10: CdSe wires grown off single bismuth beads	130
Fig. 4.11: Photoconductivity of CdSe wires	131

Chapter 1

Introduction

1.1 Tumor Biology

A tumor is an abnormal mass of tissue that arises from preexisting cells through uncontrolled cell division. Tumors can be either benign (localized, noninvasive) or malignant (invasive, metastatic, cancerous). Tumor formation is a complex multi-step process driven by a sequence of randomly occurring mutations and epigenetic alterations, the latter being promoter methylation of DNA, that affect the genes controlling cell proliferation, survival, and other traits associated with the malignant cell phenotype. These alterations require activation of oncogenes with dominant gain of function and inactivation of tumor suppressor genes with recessive loss of function. Some of these changes arise as a result of exogenous mutagens such as chemical agents, radiation, and viruses or by random error in the DNA replication process. The rate of expansion of mutant cell clones may also be governed by nonmutagenic tumor-promoting stimuli, including chronic mitogenic stimulation and inflammation. Multi-step tumor progression can be depicted as a form of Darwinian evolution occurring within tissues, in which a sequence of genetic alterations, each conferring one or another type of growth advantage, leads to the progressive conversion of normal human cells to cancer cells. A Darwinian model of cancer progression is attractive but oversimplistic and must be modified to account for critical changes in tumorigenesis that diverges from Darwinian evolution — such as epigenetic alterations, cancer stem cells, and clonal

diversification due to high mutation rates. Weinberg and others (1, 2) have identified seven essential changes (hallmarks) in cell physiology, acquired during multistep tumorigenesis, that together define all types of malignant growth, each of which represents the neoplastic cell surmounting an anticancer defense mechanism built into cells and tissues.

- 1. Self-Sufficiency in Growth Signals.** Mitogenic growth signals (GS) are required for normal cells to move into an active proliferative state, thus regulating cell division to generate the proper number of cells within a tissue or organ. These signals are transmitted into the cell by transmembrane receptors that bind distinctive classes of signaling molecules: diffusible growth factors, extracellular matrix components, and cell-to-cell adhesion/interaction molecules. Tumor cells generate many of their own signals, reducing their dependence on stimulation from their normal tissue microenvironment. This acquired GS autonomy can be achieved by five common mechanisms: alteration of extracellular growth signals (e.g., autocrine signaling loops, GS from recruited stromal cells); alteration of transcellular transducers of those signals (e.g., overexpression of cell surface receptors (e.g., EGF-R/erbB and Her2/neu (3))); structural alteration of receptors ; type switch of extracellular receptors (e.g., switch to integrins that transmit progrowth signals); or alterations of intracellular circuits that translate those signals into action (e.g., mutation in the SOS-Ras-Raf-MAPK cascade).
- 2. Insensitivity to Antigrowth Signals.** Normal tissues produce multiple anti-proliferative signals to maintain cellular quiescence and tissue homeostasis. Developing cancer cells must evade these antiproliferative signals if they are to thrive. Growth inhibitory signals are usually associated with the cell cycle, in particular the G₁ phase where the cells monitor their external environment and decide whether to proliferate, be quiescent (G₀), or enter into a post-mitotic state. Many and perhaps all of these antiproliferative signals are funneled through the retinoblastoma protein (pRb) (4) and its two relatives, p107 and p130. The inhibitory signals (e.g., the soluble signaling molecule TGF- β) result in a hypophosphorylated state of pRb which blocks proliferation by sequestering E2F transcription factor that controls the expression of a large number of genes responsible for progression from G₁

into S phase. When the pRb signaling circuit is disrupted (e.g., through alterations in transcellular transducers (TGF- β R), alterations in cytoplasmic signaling proteins (e.g., p15^{INK4B}, Smads, pRB), or the E7 oncoprotein of human papillomavirus which can sequesters pRB) and E2F is liberated, the cells become insensitive to antigrowth factors, allowing the cell to proceed with the cell division cycle. In addition to avoidance of antigrowth signals, tumors also use diverse mechanisms to avoid cells from entering into a post-mitotic, differentiated state (e.g., overexpression of the c-Myc oncoprotein and activation of the APC/ β -catenin pathway).

- 3. Evading Apoptosis.** In order for a tumor cell population to flourish, it must not only grow rapidly but also avoid cell death. A major source of cell death is apoptosis, programmed cell death. The cell senses the intracellular and extracellular environment for conditions of normality or abnormality that decide cellular fate. Intracellular sensors monitor the cell's well-being and activate apoptosis in response to abnormalities such as anoxia, hypoxia, damage to the genome, signaling imbalances in the growth-regulating machinery, survival factor insufficiency, or loss of anchorage. Extracellular sensors can transmit survival signals (e.g., survival factor IGF-1/IGF-2 by their receptor IGF-1R, IL-3 by its receptor IL-3R, cell-cell and cell-matrix adherence-based signals) or death signals (FAS by FAS receptor (5), TNF- α by its receptor TNF-R1). Loss of the tumor suppressor p53 (changes in the *p53* gene or upstream regulators), which can instigate the apoptotic cascade by sensing cell abnormalities, can make cancer cells become resistant to apoptosis (6), allowing it to survive a variety of cell-physiologic stresses. Cancer cells have developed numerous other methods to inactivate the apoptotic machinery such as activation of the survival signaling pathway PI3-kinase-AKT/PKB (can be activated by extracellular signals IGF-1/2 or IL-3, Ras, or loss of the tumor suppressor pTEN), increase levels of anti-apoptotic Bcl-2, inhibition of caspases, and interference with cytochrome c release.
- 4. Limitless Replicative Potential.** Normal cells in culture were observed to replicate a finite number of times, after which they enter into a nonproliferative state known as senescence (7). However, by disabling the pRb and p53 tumor suppressor proteins in certain cells, the cells are allowed to replicate

for additional generations until they enter into a second state known as crisis. During crisis, end-to-end chromosome fusion (due to telomere shortening) results in karyotypic disarray and almost always cell death (8). However, very rarely, a mutated cell emerges from crisis with acquired unlimited replicative potential, a trait known as immortalization. These rare cancer cells can escape crisis by telomere elongation through either upregulation of telomerase or a mechanism known as ALT (alternative lengthening of telomeres) (9).

5. **Sustained Angiogenesis.** Angiogenesis is the growth of new blood vessels from pre-existing vessels. Virtually all cells in tissue must dwell within 100 μm from capillary blood vessels to receive the oxygen and nutrients crucial for cell function and survival. The cells in tumors initially lack the ability to grow new blood vessels, limiting their ability for expansion. In order to progress to a larger size, tumors must encourage angiogenesis by changing the balance of angiogenesis inducers (e.g., VEGF (10), FGF1/2) and countervailing inhibitors (e.g., thrombospondin-1, β -interferon) (11). This ability to induce and sustain angiogenesis seems to be acquired in a discrete step (or steps) during tumor development termed the “angiogenic switch” (12). It has been shown that upregulation of *ras*, loss of p53, and extracellular proteases that release sequestered GFs in the ECM (e.g. MMPs, Cathepsin D) can shift the balance in favor of angiogenesis inducers. Moreover, integrins and adhesion molecules also play critical roles in angiogenesis (13).
6. **Tumor Invasion and Metastasis.** Primary tumors eventually generate cells that move out, invade nearby tissue, and journey to distant sites where they may form new colonies known as metastases. These distant colonies of tumor cells are the cause of 90% of cancer mortality. The invasion-metastasis cascade is a complex process involving local invasion, intravasation, transport, extravasation, formation of micrometastases, and colonization. Many of these steps can be executed by carcinoma cells that activate the cell-biological program called the epithelial-mesenchymal transition (EMT) (14), which is normally used by cells early in embryogenesis and during wound healing. This program involves changes in the attachment of cells to their microenvironment (e.g., CAMs of the immunoglobulin and cadherin family, integrins) and activation of extracellular proteases

that cleave the ECM creating space for the cells to move (MMPs). Loss of E-cadherin plays the dominant role in influencing epithelial versus mesenchymal cell phenotypes. E-cadherin forms homodimeric (and higher-order) bridges between adjacent cells in an epithelial cell layer. Loss of E-cadherin from the plasma membrane liberates β -catenin molecules, which may then migrate to the nucleus and associate with Tcf/Lef transcription factors (15), thereby inducing expression of genes orchestrating the EMT program.

7. **Avoidance of Immunosurveillance.** The immune system eliminates infectious agents as well as cancer cells through humoral and cellular immunity. Humoral immune responses are likely responsible for preventing virus-induced tumors through suppression of the infectious spread of virus. Cellular immune responses (e.g., cytotoxic T cells) are responsible for eliminating virus-transformed tumor cells that present antigenic viral oligopeptides through MHC class I proteins. The role that immune cells play in suppression of tumors of nonviral origin is more poorly understood. Tumor cells present few antigens that are clearly foreign (weakly antigenic), and thus may escape detection from the tolerance that the immune system develops toward “self” proteins. Some tumor cells attract the attention of immune system by expressing proteins in aberrant amounts or proteins that are normally displayed only on cell surface in embryos or in immunologically privilege sites. Tumor cells escape immune responses, termed cancer immunosurveillance, by immunoselection (e.g., suppression of tumor-associated antigens and generation of weakly antigenic variants through immunoediting) or by immunosubversion (e.g., killing immune cells using pro-apoptotic factors such as TGF- β and FasL, release of chemotactic factor CCL22 which attracts regulatory T cells to suppress activation of the immune system) (1).

+1. **Genomic Instability.** Cancer cells acquire the seven capabilities enabling tumor development through changes in their genome. However, mutation of specific genes is inefficient due to the multiple DNA monitoring and repair mechanisms in somatic cells, bringing into question how cancer can appear at such high frequency in the period of several decades. The fidelity of cell division is

ensured by cell cycle checkpoints and the “caretaker” system that provides DNA maintenance.

Defects in genes that are involved in the maintenance of genomic integrity generate substantially increased risk of tumors. Mutant alleles of the BRCA1 and BRCA2 genes (16), responsible for DNA homology-dependent repair, increase an individual’s susceptibility to breast and ovarian cancer. In hereditary nonpolyposis colorectal cancer (HNPCC), inherited mutations in the DNA mismatch repair pathway lead to high risk of colon cancer. The tumor suppressor p53 (“the guardian of the genome”), in response to DNA damage, can elicit cell cycle arrest or apoptosis. Mutation in the p53 signaling pathway (along with proteins for DNA repair and chromosomal segregation) can lead to genome instability (17) and generation of mutant cells with selective advantages.

1.2 Cancer Therapy

Conventional therapy for cancer can be divided into local therapy (surgery and radiation) and systemic therapy (chemotherapy, hormonal therapy, monoclonal antibodies, and radioactive materials). The modality used depends on the tumor grade, stage of the disease, location of the tumor, and the state of the patient’s health (performance status). The intent of a certain treatment modality may be curative, adjuvant (additional treatment after the primary treatment), neoadjuvant (treatment prior to primary treatment), therapeutic (has survival benefits, may be curative) or palliative (in situations where cure is not possible, used for disease control or relieve of symptoms). Multiple modalities are frequently combined for an additive/synergistic effect.

Surgery is quick, effective, allows recovery of tumor biopsy for pathological analysis, and the main curative therapy for many common solid tumors if the tumor is resected in its entirety. Microscopic invasion of surrounding normal tissue will necessitate analysis of multiple cytosections to ensure the entire tumor is removed. Tumor cells that are not removed can result in local or distant recurrence(s).

However, removal of all the tumor cells is not possible when the tumor has become invasive and has metastasized to other parts of the body prior to surgery, as is often the case due to diagnosis at a late-stage. In addition, surgeons have observed that excision of certain types of primary tumors may be followed by rapid growth of distant metastases. The growth of the metastases may be stimulated by wound healing from the surgery (inflammatory response) and/or cell migration. A growing tumor has also been recognized to suppress the growth of its metastases (e.g., through release of angiostatin into circulation to suppress angiogenesis at metastatic sites).

Radiation therapy uses ionizing radiation (X-rays, γ -rays, protons, neutrons, ions) to shrink tumors through damaging the DNA of cells. The method of delivery may be external (teletherapy) or internal (brachytherapy). Similar to surgery, radiation therapy is localized; however, unlike surgery, the anatomy is preserved. The extent of radiation therapy is limited by its teratogenic, mutagenic, and carcinogenic effects, causing an increased risk of developing secondary leukemia and/or solid tumors. Success of radiation therapy depends on the difference in radiosensitivity between tumor and normal tissue. A major limitation for radiation therapy of solid tumors is deficiency in oxygen, a potent radiosensitizer by formation of DNA-damaging free radicals, resulting in higher resistance to radiation damage compared to surrounding healthy tissue with normal oxygen content.

Systemic chemotherapy is the main treatment available for metastatic, disseminated cancers. The antineoplastic agents used are classified according to their cell cycle activity or their structure. Based on cell cycle activity, these antineoplastic agents can be divided into three groups: Cell-cycle nonspecific agents (kill proliferating or quiescent cells), cell-cycle specific/phase-nonspecific agents (kill proliferating cells regardless of the cell phase), and cell-cycle specific/phase-specific agents (kill proliferating cells only in a specific phase of the cell cycle). It should be noted that the distinction between the classes are often relative. Additionally, the major antineoplastic agents can be classified based on their chemical structure and mechanism of action into the following categories:

1. Alkylating agents (e.g. nitrogen mustards, alkylating-like agents such as cisplatin): form covalent bonds and crosslinks with DNA (in particular, guanine) and other biologically important molecules.
2. Antimetabolites (e.g., folate analogs such as methotrexate, pyrimidine analogs such as 5-FU): structural analogs of a naturally occurring metabolite involved in DNA synthesis.
3. Natural products (from plants, bacteria, and fungi; also synthetic and semisynthetic derivatives of natural products)
 - a. Plant alkaloids (e.g., paclitaxel, docetaxel): interfere with microtubule function necessary for cell division (cause disassembly or increased stability)
 - b. Antitumor antibiotics (e.g., the anthracyclines daunorubicin, doxorubicin, epirubicin): Intercalates between DNA base pairs, inhibits topoisomerases, and/or formation of free oxygen radicals that break DNA.
 - c. Topoisomerase inhibitors (e.g., topotecan, epipodophyllotoxins): Bind to and stabilize DNA/topoisomerase cleavable complex, preventing religation of the DNA strand. A double-strand break occurs when a replication fork encounters this cleavable complex.

Many antineoplastic agents (and also radiotherapy) function by damaging DNA and overwhelming the capability of the DNA repair system, resulting in cell death. Normal cells have a greater ability to repair minor DNA damage and continue living than cancer cells, thus these agents preferentially confer toxicity toward the cancer cells. Furthermore, cell-cycle specific chemotherapeutics are most effective at killing cells that are rapidly dividing (e.g., through interfering with cell division or DNA replication and function) like cancer cells. However, they are also toxic toward fast-dividing normal cells such as those found in the bone marrow (stem cells), digestive tract, hair follicles, *etc.* Certain drugs can also cause damage to specific organs (e.g., cardiotoxicity by anthracyclins, ototoxicity by cisplatin). Consequently, a major limitation of most chemotherapeutics are their narrow therapeutic index. The dosage is restricted by normal tissue tolerance and is given at close to the maximum tolerated dose (MTD). For many drugs, this

dose is so low that the concentration of drugs that can be achieved in the tumor is below the therapeutic level. Furthermore, chemotherapy drugs are oftentimes not delivered effectively throughout the entire tumor in sufficient concentration due to physiological barriers (see section 1.3) and the cellular response to the drug may also be spatially heterogeneous, resulting in eradication of cancer cells from some regions but not others. Exposure of the cancer cells to sublethal concentration of the therapeutic agent may facilitate the development of multidrug resistance (MDR) (18), in which tumor cells exposed to one cytotoxic agent develops cross-resistance to a variety of other structurally and functionally unrelated agents. MDR has been associated with at least two “pumps” that actively efflux drugs from the cell interior, the two ABC transporters, P-glycoprotein and multidrug resistance-associated protein. Altogether, these are some of the primary reasons that treatment of malignant cancer with chemotherapy often leads to recurrence and is ultimately unsuccessful.

Most of the traditional chemotherapy drugs have been discovered empirically. However, in the last 35 years, an abundance of knowledge of the molecular alterations underlying cancer has been accumulated and this knowledge has been applied to identifying and targeting specific molecules needed for carcinogenesis. “Targeted Therapy” refers to rationally designing new drugs which target particular molecules that has a critical role in tumor progression. Many of the current effort have been on kinases and cell-surface receptors since they are druggable targets by small molecules and monoclonal antibodies. Some prominent examples are:

1. Gleevac (imatinib mesylate): a small molecule inhibitor for the mutant protein Bcr-Abl (associated with the Philadelphia chromosome) in chronic myeloid leukemia (CML) (19).
2. Avastin (Bevacizumab): a monoclonal antibody for VEGF, a ligand that promotes angiogenesis (20).
3. Herceptin (Trastuzumab): a monoclonal antibody for Her2/neu (21), a growth factor receptor that becomes constitutively active in some types of breast cancer.

1.3 Drug Transport in Solid Tumors

Tumor tissue can be divided into three compartments: the blood vessels (lymphatics are nonfunctional), tumor cells, and the interstitial space (the space that surrounds the tumor cells). Systemic delivery of therapeutics to solid tumors is a three step process: circulation of blood-borne drugs to the tumor site through the blood vessels, transport across the vessel wall, and passage through the interstitial space to reach the tumor cells. However, delivery of therapeutics is hindered by physiological barriers imposed by the abnormal tumor vasculature and the dense interstitial matrix (IM), resulting in delivery of heterogeneous and sublethal concentration of the drug in the tumor.

In systemic drug delivery, drugs are initially administered through oral, intravenous, subcutaneous, intramuscular, or intraperitoneal injection. Except for intravenous, the drug is absorbed into the blood and delivered to different organs throughout the body. The drug can be cleared from the body mainly through the liver and kidney. Furthermore, the drug may be metabolized in the liver yielding an inactive metabolite; in some cases, the metabolite is the active form. The rate that the drug is removed from the blood influences the circulation half-life (time for the blood concentration to drop by a half of its initial value) which may vary from seconds to days. During the time the therapeutic is in circulation, the drug has an opportunity of being delivered into the tumor. The clearance of the drug from the body after systemic administration and delivery to healthy tissue are major obstacles to tumor drug delivery.

1.3.1 Tumor vasculature

In normal vasculature, blood enters an organ in the order of large arterioles, small arteries, arterioles, precapillary arterioles, and finally capillaries (the smallest vessels). The capillaries are responsible for the exchange of nutrients and wastes between the blood and tissue. The blood leaves the organ in the order of venules, small veins, and large veins. In the tumor, however, except for the large arteries and vein, this tree-structured hierarchy does not exist. Tumor vessels are abnormal structures that

can be described as heterogeneous, tortuous, dilated, and irregularly shaped — defying simple classification. Therefore, they are collectively known as tumor microvessels. This chaotic structure results in heterogeneous blood flow and inefficient delivery of blood-borne substances into the tumor. Blood flow velocity may vary both spatially and temporally with blood sometimes flowing backwards. In many regions of the tumor, blood flow is slower than in normal tissue, resulting in decreased delivery of a systemically administered drug into the tumor. Some of the tumor vessels are too small to allow red blood cells to pass through and the average velocity of red blood cells can be an order of magnitude lower than in normal tissue, both of which contributes to tumor hypoxia. In addition, tumor microvessels lack smooth muscle cells on the blood vessel walls so that these vessels cannot react to vasoactive agents which regulate blood flow in normal vasculature.

1.3.2 Transvascular transport

Once the therapeutics is in the tumor microcirculation, they may cross the vessel wall to enter the tumor's interstitial space (22). The rate of transvascular transport for the drug can be modeled by the Kedem-Katchalsky Equation (23):

$$J_s = J_v(1 - \sigma_f)C_s + PS \Delta C \quad (1.1)$$

The first term is attributed to convective transport and the second term to diffusive transport (Fick's first law). The rate of fluid flow across the microvessel wall J_v can be modeled using Starling's law of filtration:

$$J_v = L_p S(\Delta p - \sigma_s \Delta \pi) \quad (1.2)$$

This equation states the rate of fluid flow across the microvessel wall is proportional to the hydrostatic pressure difference Δp minus the osmotic pressure difference $\Delta \pi$. Starling's law is equivalent to Darcy's law ($v = -K \nabla p$) except the osmotic pressure gradient is also taken into account.

The constants are defined as follows:

v : fluid velocity

K : hydraulic conductivity. Equal to the Darcy permeability to the viscosity

∇p : gradient of the hydrostatic pressure

Δp : hydrostatic pressure difference across vessel wall

$\Delta\pi$: osmotic pressure difference across vessel wall

L_p : hydraulic conductivity of the vessel wall

S : surface area of the vessel wall

σ_s : osmotic reflection coefficient. This term arises because the microvessel wall is permeable to the separation of solutes that maintain the osmotic pressure difference.

σ_f : filtration reflection coefficient.

C_s : average molar concentration of solutes in the vessel wall

P : microvascular permeability coefficient. Here, P is D_{eff}/h , where h is the thickness of the vessel wall

ΔC : difference in concentration across the vessel wall

It is useful to note that J_v/S is the average velocity of fluid across the membrane per unit area.

In normal tissues, the transcapillary filtration and reabsorption of fluid back into the blood vessel occurs according to Starling's law of filtration which depends on the hydraulic and osmotic pressure. The small amount of fluid that is not reabsorbed back into circulation is taken up by lymphatic vessels, which is driven by small shifts in the hydraulic and osmotic pressure. Thus in normal tissues, transport of drugs can be due to both diffusion and convection. In neoplastic tissues, transvascular transport has three unique

features. First, microvascular permeability is generally higher than in normal tissues due to the “leaky” vasculature. But tumor vessel walls are “leaky” in some regions while not in others, which causes heterogeneous perfusion of drugs. Second, the pores in the vessel wall have a higher cutoff size than in normal tissues, allowing particles up to several hundred nanometers to extravasate into the tumor. The liver sinusoids also allow large particles to extravasate but the cutoff size is only ~100 nm. Third, solid mechanical stress induced by the proliferating neoplastic cells in a confined space causes the collapse of lymphatic vessels (24). The lack of functional lymphatics and the hyperpermeable vasculature result in elevated levels of interstitial fluid pressure (IFP), which in turn reduces convective transport across the vessel walls and into the interstitial space, leaving diffusion as the primary mode for transvascular drug transport.

1.3.3 Interstitial Transport

After crossing the vessel wall or after local administration, the drug must pass through and react with components in the tumor’s interstitial space. This region is made up of the interstitial fluid – consisting of nutrients, wastes, growth factors, inhibitors, etc. – and the extracellular matrix – a complex assembly of collagens, elastins, glycoaminoglycans, proteoglycans, and structural glycoproteins. The constituents of the interstitial fluid are similar to those in the plasma except for lower concentrations of oxygen and glucose. Transport across the interstitial space is one of the most difficult steps in drug delivery to tumor cells due to several unique characteristics of solid tumors at the molecular, cellular, and tissue level (23). First, as mentioned previously, low convective transport through the interstitial space leaves diffusion as the primary mode for both transvascular and interstitial transport. In normal tissues, diffusion has been found to be dominant for small therapeutics and convection to be more significant for larger therapeutics like monoclonal antibodies, viruses, and nanoparticles (since diffusion is highly size dependent). Therapeutics larger than 60 nm are not able to effectively diffuse in the interstitial space due to the dense collagen matrix. Because diffusion is the primary mode for transport in the interior of the

tumor, interstitial transport is especially difficult for the delivery of larger therapeutic agents. Second, the pressure gradient drops off precipitously at the tumor margin, causing a convective flow of drugs (along with excess fluid, macromolecules, and tumor cells) to seep out of the tumor periphery and be collected by the lymphatic vessels in the tumor margin and surrounding normal tissue, reducing drug delivery to tumor cells. Third, due to the heterogeneous perfusion of tumor vessels, drugs need to diffuse large distances to reach hypo-vascular regions of the tumor. Fourth, binding (e.g. to DNA, extracellular matrix), sequestration (e.g. in endosomes), and metabolism of drugs hinder the transport of therapeutic agents in the interstitial space.

Drug transport in the tumor in the interstitial space can be depicted as solute transport in porous media filled with discrete obstacles to diffusion – the tumor cells. A complete physical description of diffusion through the interstitial space is exceedingly cumbersome. Effective diffusion coefficients are often used to estimate rates of transport in these situations. The increase in path length induced by physical obstacles in the interstitial space can be described by the tortuosity. Tortuosity is defined as the ratio of effective path length (L , shortest distance between two points through the obstacles) to linear path length (L_o , shortest distance between the same two points disregarding the obstacles): $\tau = L/L_o$. The variables of concern are defined below:

D_{eff} : effective diffusion coefficient measured in tissue

D_{int} : interstitial diffusion coefficient

D_o : diffusion coefficient in free solution

τ : tortuosity

τ_g : geometric tortuosity

τ_v : viscous tortuosity

The Stokes-Einstein relation can be used to determine the diffusion coefficient of an agent in free solution assuming it has a spherical configuration:

$$D_o = \frac{k_B T}{6\pi\mu R_H} \quad (1.3)$$

where k_B is Boltzmann's constant, $k_B = 1.38 \times 10^{-23}$ J/deg, T is temperature in K, μ is the viscosity of water, and R_H is the hydrodynamic radius. The diffusion coefficient measured in tissue is related to the diffusion coefficient in free solution by the tortuosity (25, 26):

$$D_{eff} = \frac{1}{\tau^2} D_o \quad (1.4)$$

The tortuosity is a result of contributions from cellular obstacles and matrix molecules: $\tau = \tau_g \tau_v$. The geometric tortuosity (τ_g) is due to the geometric effects imposed by the organization of tumor cells which can hinder long range diffusion of smaller therapeutics. The viscous tortuosity (τ_v) is due to the frictional effects induced primarily by the dense collagen matrix which assumes greater importance when the size of the therapeutic agents becomes comparable to the dimensions of the channel through which they have to traverse. The diffusion coefficient in the interstitial space D_{int} is related to diffusion in free solution through: $D_{int} = \frac{1}{\tau_v^2} D_o$.

1.4 Nanomedicine for Cancer Therapy

An ideal drug-delivery system possesses two properties: the ability to target and to control the release of drugs. Targeting will ensure the drug is delivered to the tumor with high efficiency and adverse effects in normal tissues are reduced. Targeting is especially important for anticancer drugs, which are also cytotoxic toward normal cells. Controlled release can also reduce or prevent adverse affects.

Nanocarrier delivery systems have provided new tools for the delivery of therapeutics that can facilitate

transport to the tumor and provide controlled release. Specifically, the advantages of nanocarrier delivery systems may include (27):

1. Enhanced Permeation and Retention (EPR) Effect: Because the cutoff size of pores in the tumor vessel wall is generally higher than vessel walls found in normal tissues, nanotherapeutics are able to preferentially accumulate in the “leaky” regions of tumor vasculature more than in normal tissue due to their large size compared to much smaller therapeutics, thus reducing normal tissue toxicity. Furthermore, the lack of functional lymphatics in the tumor interior hinders clearance of the drug from the tumor. All these factors contribute to the phenomenon known as the EPR effect (28).
2. Delivery of hydrophobic drugs.
3. Co-delivery of two or more therapeutics for combination therapy.
4. Co-delivery of therapeutics with imaging modalities for simultaneous visualization of sites for drug delivery.
5. Delivery of large macromolecules into cells.
6. (Active) targeted delivery of therapeutic to the cell/tissue of interest.
7. Protect drugs from binding (to cancer cells or components in the tumor microenvironment), metabolism (degradation), and sequestration.
8. Increase blood circulation time.
9. Controlled drug release.
10. Improved dose scheduling for higher patient compliance.

However, nanotherapeutics also adds to the list of challenges in developing, manufacturing, and gaining regulatory approval of anticancer drugs. The following are several characteristics that are advantageous in designing a nanocarrier drug delivery system (29):

1. The active pharmaceutical ingredient (API) comprises a high weight fraction (loading) of the total nanocarrier system (for example, at least 30%).
2. A large fraction of API used in the first step of the encapsulation process is incorporated into the final carrier (entrapment efficiency).
3. The nanoparticles (NP) can be freeze-dried and reconstituted in solution without aggregation.
4. Biodegradable.
5. Small size. Typically ~100 nm or less for passive tumor targeting and greater than ~6 nm to avoid renal clearance.
6. Characteristics to prevent rapid clearance of the particles from the bloodstream (e.g., a “stealthy” surface to prevent clearance by the reticuloendothelial system or RES).

A nanoparticle drug delivery system needs to exhibit the above characteristics to a large extent.

To date, over twenty nanotherapeutics have been FDA-approved for clinical use. These products are dominated by liposomal drugs and polymer-drug conjugates. Examples of FDA-approved nanoparticle-based therapeutics for solid tumors include Doxil® (~100 nm PEGylated liposomal form of doxorubicin), Abraxane® (~130 nm albumin bound paclitaxel nanoparticle), and DaunoXome® (a 40-60 nm liposomal form of daunorubicin). Despite lower toxicity to normal tissues such as reduced cardiotoxicity in the case of Doxil®, nanotherapeutics still have adverse affects such as palmar-plantar erythrodysesthesia for Doxil® and sensory neuropathy and nausea for Abraxane®.

In the case of the paclitaxel nanosuspension Abraxane®, the nanoparticle formulation of paclitaxel provides several significant advantages over the Cremophor-based formulation Taxol®. Paclitaxel is a very hydrophobic molecule and has been formulated with Cremophore EL and ethanol in order to be given to humans. However, Cremophore EL has been associated with a host of problems including hypersensitivity (requiring premedication such as antihistamines and the steroid dexamethasone), long infusion time (3 hrs), and leaching of plasticizer from IV tubing. On the other hand,

Abraxane® is a formulation of paclitaxel that uses only human serum albumin, a natural carrier for hydrophobic molecules, without the need for any solvents. No premedication is necessary and the drug is given only over 30 minutes with standard IV tubing. Transmission electron microscopy (TEM) of Abraxane® shows a core consisting of paclitaxel, surrounded by an albumin shell. The diameter ranges in size from 100 to 200 with an overall mean size of 130 nm. The zeta potential is -31 mV. It is manufactured by adding a solution of methylene chloride solution containing paclitaxel to an aqueous solution of human serum albumin under low speed homogenization, creating an emulsion (30). The albumin migrates to the interface between the water and methylene chloride of the emulsion. High-pressure homogenization is applied to reduce the size of the particles and stabilize the particles through disulfide bond cross-linking. The methylene chloride is then volatilized and the suspension is sterile-filtered. The resulting aqueous suspension of nanoparticles consists of an amorphous paclitaxel core coated with a 25 nm thick shell of paclitaxel-bound albumin. The size of the albumin nanoparticles is highly concentration dependent. The nanoparticles are initially 130 nm at high concentration (in the original vial). But as the concentration is reduced in plasma, the size very rapidly decreases to 10-15 nm albumin particles.

The Table 1.1 provides a comparison of the pharmacokinetic properties between Abraxane® and Taxol®. The maximum drug concentration C_{max} is higher for Abraxane® because it is given over 30 minutes instead of 3 hours. The reduced area-under-the-curve (AUC) or overall amount of drug in the blood after a dose for Abraxane® has been attributed to faster partitioning out of the vascular compartment. In the case of Taxol®, Cremophor micelles are bound very strongly to paclitaxel, reducing the amount of free paclitaxel in the plasma available for partitioning into the tissue compartment from the central blood compartment. Abraxis BioScience, the company behind Abraxane®, has claimed that Abraxane® can enhance tumor delivery by exploiting the endogenous albumin pathways SPARC (secreted protein acidic rich in cysteine) and endothelial transcytosis via albumin-mediated gp60 receptor.

Drug/dose	C _{max} (ng/mL)	AUC _(0-inf) (ng hr/mL)	t _{1/2} (hr)	Cl (L/hr/m ²)
Abraxane (135 mg/m ² / 30min)	6100	6427	15	21
Taxol (135 mg/m ² /3 hr)	2170	7952	13	18

Table 1.1. Pharmacokinetics comparison between Taxol® and Abraxane®

Nanotherapeutics like Abraxane® and Doxil® have resulted in reduced adverse effects in normal tissues but have provide only modest survival benefits (31-33). This sub-optimal outcome is likely attributed to the physiological barriers imposed by the abnormal tumor vasculature and the dense interstitial matrix which hinder delivery of the drug throughout the entire tumor in sufficient concentration (34, 35).

As previously mentioned, systemic delivery of therapeutics to the tumor is a three step process: blood-borne delivery to different regions of the tumor, transport across the vessel wall, and passage through the interstitial space to reach the tumor cells (36). Abnormalities in the tumor vasculature lead to highly heterogeneous vascular perfusion throughout the tumor. The microvascular density is high at the invasive edge of the tumor but sometimes the tumor center is unperfused, preventing delivery of therapeutics to this region. However, the tumor center's hostile microenvironment (low pH and low pO₂) harbors the most aggressive tumor cells and the tumor will regenerate if these cells are not eliminated. Moreover, exposure of the cancer cells to sublethal concentration of the therapeutic agent may facilitate the development of resistance.

Hyper-permeability of the abnormal vasculature and lack of functional lymphatics lead to elevated levels of interstitial fluid pressure (IFP) (37, 38). This interstitial hypertension in turn reduces convective transport across the vessel wall and into the interstitial space, leaving diffusion as the primary mode for drug transport to the poorly perfused regions. Large 100-nm nanotherapeutics such as Doxil® are suitable for the EPR effect (39) but have poor diffusion in the dense collagen matrix of the interstitial

space (40, 41), resulting in restrictive nanoparticle accumulation around tumor blood vessels and little penetration into the tumor parenchyma. In the case of Doxil®, the liposomal particles are trapped close to the tumor vasculatures. Although the small size (~400 MW) of doxorubicin, which is released from the liposomes, seemingly allow rapid diffusion, doxorubicin cannot migrate far from the particles due to avid binding to DNA and sequestration in acidic endosomes of perivascular tumor cells (42, 43), resulting in heterogeneous therapeutic effects.

1.5 Multistage Nanoparticle Delivery System

To navigate through the multiple obstacles preventing effective drug delivery to solid tumors, we propose a multi-stage approach in which nanoparticles change their size to facilitate transport by adapting to each physiological barrier. The multistage nanoparticles are originally ~100 nms and preferentially extravasate from the leaky regions of the tumor vasculature. After extravasation into tumor tissue, the nanoparticles “shrink” to 10 nm, significantly lowering their diffusional hindrance in the interstitial matrix (25) and allowing penetration into the tumor parenchyma. These smaller nanoparticles can potentially be used as nanocarriers for therapeutics that are released as the particles penetrate deep into the tumor (Figure 1.1). Surface PEGylation of the small nanoparticles allows them to diffuse smoothly in the interstitial matrix by reducing the binding, sequestration, and metabolism that hinder the transport of therapeutic agents (44, 45). Furthermore, 10-nm nanoparticles are not cleared from the tumor as rapidly as much smaller molecular species due to their larger size.

To achieve this size shrinking property, a large nanoparticle should be triggered to release smaller nanoparticles after extravasation into the tumor. Several nanoparticles have been designed to release their contents remotely via an external stimulus (light, heat, ultrasound, magnetic field, *etc.*), but their use to date has been limited to local therapy. Systemic therapy is necessary to treat the metastases, which are the major cause of cancer mortality. Water hydrolysis- (29), diffusion-, or solvent-controlled release

mechanisms can achieve systemic effects but do not give preferential release in the tumor, resulting in increased toxicity in normal tissues. To attain both systemic therapeutic effects and preferential release in tumor tissues, we aim to trigger the size change using an endogenous stimulus characteristic of the tumor microenvironment, such as low pH, low partial oxygen pressure, or high concentrations of matrix metalloproteinases (MMPs). Acidic and hypoxic regions tend to be far from blood vessels (46), not in the perivascular regions where the large nanoparticles are trapped. MMPs, particularly gelatinases A and B (MMP-2 and -9), are key effectors of angiogenesis, invasion, and metastasis including the epithelial-mesenchymal transition (EMT), a cell-biological program which executes many of the steps of the invasion-metastasis cascade. They cleave away the extracellular matrix (ECM), creating space for the cell to move and releasing sequestered growth factors (47, 48). Levels of MMP-2 and -9 are high at the invasive edge of tumors and at the sites of angiogenesis – regions the large nanoparticles are likely to extravasate. These conditions make enzymatic degradation by MMPs a highly favorable trigger mechanism.

Because both MMP-2 and -9 are extremely efficient at hydrolyzing gelatin (denatured collagen), we engineered a 100-nm nanoparticle with a core composed of gelatin and a surface covered with quantum dots (QDs), a model 10-nm nanoparticle. Gelatin nanoparticles have been shown to have a long blood circulation time and high accumulation in tumor tissues (49), properties necessary for the first-stage NP carrier. In order to access the spatial and temporal distribution of the nanoparticles in the tumor milieu, we used ~10 nm QDs as a stand-in for therapeutic nanocarriers, so that the nanoparticles' distribution *in vivo* can be imaged using time-lapse multiphoton microscopy. Compared to traditional organic fluorophores, QDs have high resistance to photo- and chemical-degradation, narrow photoluminescence spectra, broad excitation spectral windows, and large two-photon absorption cross-sections – enabling the use of multiphoton microscopy to image deep into the tumor with high spatial resolution (50).

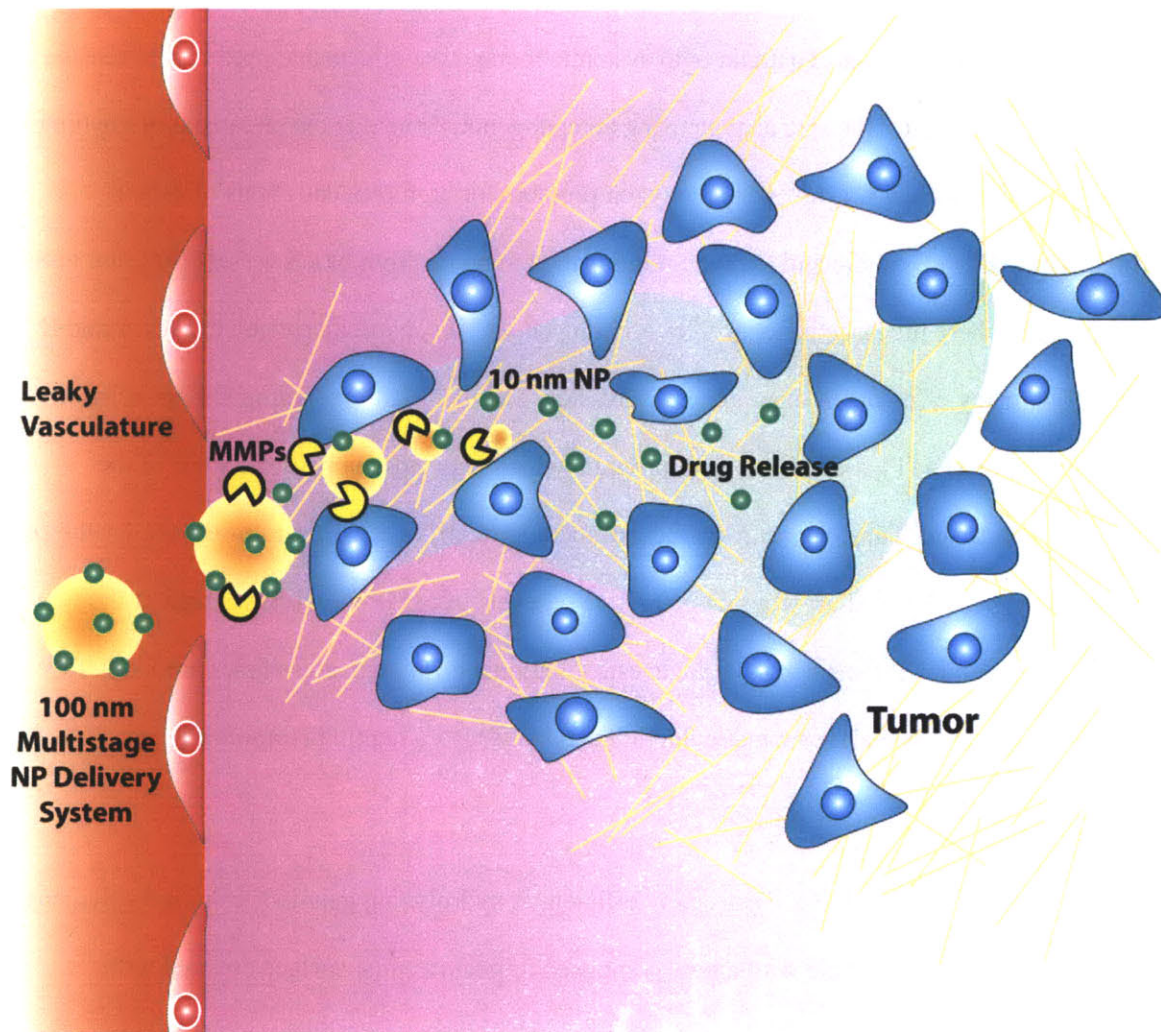


Figure 1.1 Schematic depiction of the multistage nanoparticle drug delivery system. The initial 100-nm multistage nanoparticle delivery system accumulates preferentially around leaky vessels in tumor tissue. Due to its large size, the 100-nm nanoparticle cannot penetrate the dense collagen matrix of the interstitial space. However, endogenous MMPs can proteolytically degrade the gelatin core of the 100-nm nanoparticle, releasing smaller 10-nm nanoparticles from its surface, which can penetrate deep into the tumor due to their small size and PEGylated (“stealthy”) surface. After disseminating all through the tumor, the 10-nm nanoparticles can serve as depots for drugs that are released uniformly throughout the tumor.

1.6 Quantum Dots in Biological Applications

Fluorescence tagging in the life sciences has traditionally relied on organic fluorophores and fluorescent proteins for tracking or analyzing biological molecules by means of their fluorescent emission at a specific frequency. However, these species suffer from narrow excitation range, broad emission spectra, tendency for photobleaching and chemical degradation that limit their uses in bioimaging and sensing. Semiconductor nanocrystals or quantum dots (QD) possess certain properties that offer advantages over their organic counterparts in certain bioapplications. They possess broad excitation spectral window that span from the band edge to the UV region, allowing multiplex imaging through the ability to excite QDs with multiple narrow emissions using a single excitation wavelength. By tuning the size of the QD and using different materials, the emission wavelength of the QD can be tuned from the visible to the near infrared wavelengths. In addition, their large two photon absorption cross section enables their use in multiphoton microscopy for deep imaging with high resolution. QDs have been conjugated to various biomolecules such as peptides, proteins, DNA, *etc.* for applications in imaging, sensing, and diagnostics.

1.6.1 Basic Properties

Semiconductor nanocrystals (QDs) are small solution-grown clusters of atoms that are $\sim 1-10$ nm in size. Their shapes can be spherical, cubic, rod-like (51), triangular, etc. These materials exhibit unique electronic properties different from their bulk counterparts that are attributed to the quantum confinement effect. The quantum confinement effect occurs when the size of the nanocrystal becomes comparable to, or smaller than, the size of the bulk Bohr exciton radius. This effect results in the widening of the effective energy band gap with decrease in nanoparticle size that causes a blue-shift in the first absorption peak and the photoluminescence spectrum. Quantum confinement also results in discrete energy states of higher energy in the valence and conduction band. This phenomenon can be understood by a simple

extension of the one-dimensional particle in a box model to a three-dimensional (or spherical) model where the box represents the QD and the barrier represents the abrupt interface at the QD surface. For a one-dimensional box with infinite barrier and length L , the carrier confinement results in discrete energy levels that are spaced at

$$E_n \propto \frac{n^2}{L^2}, \text{ with } n = 1, 2, 3 \dots \quad (1.5)$$

In the case of a spherical energy barrier with radius a_o , the energy levels for the electron and hole can be written as (52):

$$E_{l,n}^{e,h} = \frac{\hbar^2 \beta_{l,n}^2}{2m_{e,h} a_o^2} \quad (1.6)$$

Where $\beta_{l,n}$ is the n th root of the spherical Bessel function of order l (solution obeying the boundary condition), $m_{e,h}$ is the effective mass of the electron (e) or hole (h), and a_o is the radius of the QD. The confinement results in discrete quantized exciton transitions and an increase in the effective band gap energy with decreasing particle size, which is expressed as

$$E_g(QD) = E_g(bulk) + \frac{\hbar^2 \pi^2}{2m_{e,h} a_o^2} \quad (1.7)$$

It should also be mentioned that these energy levels are also affected by the Coulomb interaction between the confined carriers. However, this term has a weaker dependence on size ($1/a_o$ dependence instead of $1/a_o^2$) so the contribution is small and often treated as a perturbation on the energy values. The relationship between size and spectral shifts in the absorption and fluorescence peaks for CdSe quantum dots has been relatively understood.

Colloidal QDs have also been discovered to exhibit intermittent on/off photoluminescence (blinking) (53). This property has been attributed to Auger recombination though the phenomenon is not

fully understood. Recently, QDs have been shown to be non-blinking by overcoating with a thick CdS shell (54).

1.6.2 Synthesis and Characterization

Solution-phase growth of semiconductor nanocrystals was first carried out within inverse micelles. This approach uses the natural nanoscale structures created by water-in-oil mixtures upon adding an amphiphilic surfactant such as sodium dioctyl sulfosuccinate (AOT), cetyltrimethylammonium bromide (CTAB), and tetraoctylammonium bromide (TOAB). The size of the water-in-oil droplets can be controlled by varying the water content. Metal salts are added to the solution and they migrate to the water droplets, initiating nucleation and growth. However, this method did not produce QDs with good crystalline structure and high quantum yield that is necessary to transition to biological applications.

A major breakthrough occurred in 1993 when Bawendi and coworkers showed that high quality nanocrystals can be synthesized using an organometallic approach based on the pyrolysis of metal-organic precursors (55). This approach yielded QDs with crystalline core, narrow size distribution (~10 percent), and relatively high quantum yield. The synthesis typically used dimethylcadmium (CdMe_2) and trioctylphosphine selenide (TOP-Se) diluted in trioctylphosphine (TOP) and injected into a coordinating solution of trioctylphosphine oxide (TOPO) at 280-300°C. The size distribution can be further improved using size selective precipitation. This synthetic method improved the QD's quantum yields to 5-10% enabling fundamental fluorescence-based studies and research in technological applications.

Peng and coworkers later used less volatile, pyrophoric, and hazardous precursors than CdMe_2 to effectively prepare high-quality nanocrystals (56). They and other groups also pointed out the importance of impurities such as hexylphosphonic acid (HPA) and tetradecylphosphonic acid (TDPA) in coordinating to the metal precursors and controlling the reaction kinetics. In this method, high quality Cd-based nanocrystal was synthesized using high purity TOPO, controlled amounts of metal coordinating ligands, and more benign metal precursors such as CdO, cadmium acetate ($\text{Cd}(\text{OAc})_2$), cadmium hydroxide

(Cd(OH)₂), and cadmium acetylacetonate (Cd(acac)₂). Murray and coworker showed that near-infrared PbSe QDs can also be synthesized using a high temperature synthetic route with oleic acid, TOP:Se, and Lead(II) acetate trihydrate or lead oxide (57, 58).

Precipitation involves addition of a nonsolvent of the QD (methanol, ethanol, acetone, etc) into the QD solution. Centrifugation of the precipitated solution followed by removal of the supernatant purifies the solution of left over reagents from the synthesis and excess ligands. Size selection of the QD sample can be performed by tuning the amount of the nonsolvent added such that only the larger fraction of the QD population precipitates. When using less reactive precursors, precipitation is essential in removing impurities and various metal-coordinating molecules since large amounts of unreacted material are left over in the QD gross solution.

Overcoating the QD with a layer of higher band gap material can passivate the QD surface which greatly improves the quantum yield and stability of the nanocrystal. In 1996, Hines and Guyot-Sionnest overcoated CdSe QDs with ZnS to improve the quantum yield up to >30% (59). Air-stable precursors have also been applied to overcoating as in the case of core synthesis. After overcoating, the absorption and fluorescence spectra red shifts and both the absorption and emission peaks usually broaden. The red-shifting is higher for lower band gap shell material (CdSe vs ZnS) and is attributed to leakage of the exciton wavefunction into the shell layer because of the shell's finite barrier height. The spectral broadening is caused by broadening in the size distribution that occurs during the overcoating step carried out at high temperature. A smaller lattice mismatch in the core and shell material results in less lattice strain at the interface and enables higher quality epitaxial growth of shell material.

General QD characterization techniques include high and low resolution transmission electron microscope (TEM), wide angle X-ray diffraction (XRD), small angle X-ray scattering (SAXS), ICP-OES, absorption, and fluorescence spectroscopy. These measurements can be used to obtain the size,

distribution width, crystal structure, band edge value, emission energy level, and quantum yield of the QD sample.

1.6.3 Water-Solubilization Strategies

QDs can be made water soluble by directly synthesizing them in aqueous solution using inverse micelle or co-precipitation as shown for CdTe QDs. However, these synthesis methods have not produced high enough quality QDs that could be used for *in vivo* applications. QDs prepared using high temperature synthesis routes capped with TOP/TOPO (also with amines and/or acid molecules) have been one of the main methods for synthesizing QDs used for *in vivo* biological applications. Synthesis routes utilizing TOP/TOPO produces an outer layer of hydrophobic ligands after synthesis which makes it necessary to develop water solubilization strategy for transferring the QD to aqueous solution. These strategies can be roughly divided into ligand-exchange and encapsulation.

Ligand exchange involves replacement of the original hydrophobic surface ligands with hydrophilic surface ligands. The hydrophilic ligand is composed of anchor group(s) that bind to the QD surface (typically by thiol or imidazole) and hydrophilic group(s) that render the QD water soluble (PEG, amine, carboxyl). The most basic ligands are monothiol alkyl carboxylic acids such as cysteine (60), mercaptoacetic acid (MAA), mercaptopropionic acid (MPA), mercaptoundecanoic acid (MUA), and poly(ethylene glycol) (PEG) derivatives of these ligands. Cap-exchanges involving these ligands are simple but the resulting QDs are usually unstable in aqueous solution and end up aggregated within a day. The fluorescence quantum yield also decreases due to decrease in surface passivation and aggregation. This instability is due to desorption of the ligand from the QD surface. This problem can be alleviated by using bidentate-thiol ligands such as dihydrolipoic acid (DHLA) (61). DHLA-capped QDs can be stable in aqueous solution for a week. However, DHLA-capped QDs and other carboxyl-terminated QDs are only stable at basic pH due to protonation of the carboxyl groups at low pH and thus loss of surface

charge. This problem can be prevented by the use of PEGylated derivatives that allow for stability at a wide range of pH (62). Additionally, the terminal end of the DHLA-PEG ligand can be functionalized with amine, carboxyl, biotin, *etc.* for further bioconjugation reactions (60). This method provides a functional and modular approach to bind to bio-molecules through biotin-streptavidin or sulfo-NHS (*N*-hydroxysulfosuccinimide)/EDC (1-Ethyl-3-[3-dimethylaminopropyl]carbodiimide hydrochloride) coupling chemistry.

A related technique for water solubilization developed by Weiss and coworkers (63) uses a peptide with multiple cysteines for multidentate binding with the QD surface. The advantage of this technique is that the peptide can be designed using standard Fmoc peptide chemistry to have different lengths and functional groups. In addition, a peptide sequence can be directly built in for biological targeting. The disadvantages are that peptide synthesis is relatively expensive and large amounts of peptides are necessary for cap exchange.

Alivisatos and coworkers first introduced the use of QDs for biology by coating the QD with a layer of silica which can then be functionalized using silane precursors (64). The QDs are first cap-exchanged with a thiol-terminated silane ligand, and then the shells are cross-linked to promote stability. This strategy, however, is time consuming and control of the shell growth is difficult.

Kim *et al.* developed an oligomeric phosphine ligand composed of an inner layer of oligomeric phosphine for passivation of the QD surface and an outer layer of carboxylic acid or PEG for water solubilization (65). However, this approach requires tedious synthesis and purification of the ligand. Other groups have used similar multidentate approaches that use polymers with multiple amines for binding to the QD surface such as polyethyleneimine and poly(ethylene glycol-*b*-2-N,N-dimethylaminoethyl methacrylate) (PEG-*b*-PDMA). Liu *et al.* later developed a polymer synthesized using RAFT polymerization chemistry with multiple imidazole groups for binding to the QD surface and PEG for water solubilization (66). The multidentate binding with imidazole allowed for high stability

compared to thiol-based ligands and was demonstrated to be stable in PBS at room temperature for months. However, due to the protonation of imidazole at low pH, the resulting QDs are not stable below pH ~6. Another disadvantage is that functionalization with amine-PEG results in the amines binding on the QDs' surface instead of being exposed and available for bioconjugation. EDC-coupling of the QDs to biomolecules produces low conjugation yields.

Another method for water solubilization is encapsulation within an amphiphilic molecule, such as block copolymer shells and phospholipid micelles (67). These amphiphilic molecules contain hydrophobic segments that interdigitate with the TOP/TOPO shell and hydrophilic units that impart dispersion in aqueous solution. Di- and tri-block copolymers have been used as the amphiphilic coating shell for QDs. These molecules usually contain a polyacrylic acid backbone and substitution of some of the carboxyl groups with alkyl chains. A balance between the hydrophilic and hydrophobic groups on the surface is necessary for stability in water. Wu *et al.* (68) have used a 40% octylamine-modified polyacrylic acid which is currently used in the commercial QDs sold by Invitrogen. Pellegrino *et al.* (69) have used a poly(maleic anhydride alt-1-tetradecene) for water solubilization. This polymer is first absorbed onto the surface of the QD and then bis(6-aminoethyl)amine is applied to cross-link the polymer for enhanced stability. The anhydride groups are then hydrolyzed for water solubilization. Dubertret *et al.* reported another approach that uses phospholipid derivatives to form a micelle around the QD (67). They first used a mixture of 40% 1,2-dioleoyl-sn-glycero-3-phosphoethanolamine-N-[methoxy(polyethylene glycol)-2000] (mPEG-2000 PE) and 60% 1,2-dipalmitoyl-sn-glycero-3-PC. However, this approach requires rather expensive phospholipids, suffers from instability at low concentrations, and each micelle may contain more than one QD.

The various surface functionalization strategies have strengths and weaknesses that make each of them suitable for different applications. The cap-exchange methods tend to produce the most compact QDs but they suffer from a lower quantum yield (QY) because their original ligand shell has to be ripped off and replaced. Whereas, encapsulation methods tend to produce QDs with higher QY due to the

preservation of their original TOP/TOPO ligand coating but their hydrodynamic diameter tend to be larger. Applying QDs for a certain biological application require careful assessment of the advantages and drawbacks of different water-solubilization strategy.

1.6.4 Bio-Conjugation Strategies

There are four main approaches to conjugate molecules to water soluble QDs: EDC/sulfo-NHS/SMCC coupling, biotin-avidin(streptavidin) binding ($K \sim 10^{-15}$ M), metal-affinity driven self assembly of polyhistidine/thiolated peptides (70) and engineered proteins on the QD surface ($K \sim 10^{-10}$ - 10^{-8} M), and tetracene-neoborene coupling (71). Each of these methods has strengths and weaknesses. EDC coupling usually does not require further modification of the bio-molecule. However, this method may cause aggregation for carboxyl coated QDs (72). Metal-affinity driven self assembly of polyhistidine peptides is based on the high affinity of polyhistidine toward the Group II elements (Cd, Zn) on the QDs' surface. This method have high conjugation efficiencies that allow some control over the valency of bound peptides but they are limited to cap-exchanged QDs that allow accessibility of the polyhistidine on the QD surface such as DHLA-based and monothiol ligands. Biotin-avidin binding is highly efficient, stable, and specific but require conjugation of either biotins or avidins to the biomolecules first. The avidin or streptavidin also adds to the size of the QD-conjugate. Tetracene-neoborene coupling exhibits high specificity but requires a relatively tedious synthesis procedure.

1.7 References

1. L. Zitvogel, A. Tesniere, G. Kroemer, *Nature Reviews Immunology* **6**, 715 (2006).
2. D. Hanahan, R. A. Weinberg, *Cell* **100**, 57 (2000).
3. D. J. Slamon *et al.*, *Science* **235**, 177 (1987).
4. G. J. Hannon, D. Beach, *Nature* **371**, 257 (1994).
5. A. O. Hueber *et al.*, *Science* **278**, 1305 (1997).
6. H. Symonds *et al.*, *Cell* **78**, 703 (1994).
7. L. Hayflick, *Biochemistry-Moscow+* **62**, 1180 (1997).
8. C. M. Counter *et al.*, *Embo J* **11**, 1921 (1992).
9. T. M. Bryan, A. Englezou, J. Gupta, S. Bacchetti, R. R. Reddel, *Embo J* **14**, 4240 (1995).
10. K. J. Kim *et al.*, *Nature* **362**, 841 (1993).
11. P. Carmeliet, R. K. Jain, *Nature* **407**, 249 (2000).
12. G. Bergers *et al.*, *Nat Cell Biol* **2**, 737 (2000).
13. F. G. Giancotti, E. Ruoslahti, *Science* **285**, 1028 (1999).
14. A. E. Vernon, C. LaBonne, *Curr Biol* **14**, R719 (2004).
15. G. Christofori, H. Semb, *Trends Biochem Sci* **24**, 73 (1999).
16. J. D. Fackenthal, O. I. Olopade, *Nature Reviews Cancer* **7**, 937 (2007).
17. A. J. Levine, *Cell* **88**, 323 (1997).
18. P. Borst, R. Evers, M. Kool, J. Wijnholds, *J Natl Cancer I* **92**, 1295 (2000).
19. S. Chu, M. Holtz, M. Gupta, R. Bhatia, *Blood* **103**, 3167 (2004).
20. N. Ferrara, K. J. Hillan, W. Novotny, *Biochemical and Biophysical Research Communications* **333**, 328 (2005).
21. E. H. Romond *et al.*, *New Engl J Med* **353**, 1673 (2005).
22. R. K. Jain, *Cancer and Metastasis Reviews* **6**, 559 (1987).
23. G. A. Truskey, F. Yuan, D. F. Katz, *Transport phenomena in biological systems*. (Pearson Prentice Hall, Upper Saddle River, N.J., ed. 2nd, 2009), pp. xxiii, 860 p.
24. A. J. Leu, D. A. Berk, A. Lymboussaki, K. Alitalo, R. K. Jain, *Cancer Research* **60**, 4324 (2000).
25. A. Pluen *et al.*, *Proc Natl Acad Sci USA* **98**, 4628 (2001).
26. S. Ramanujan *et al.*, *Biophysical Journal* **83**, 1650 (2002).
27. R. K. Jain, T. Stylianopoulos, *Nature Reviews Clinical Oncology* **7**, 653 (2010).
28. H. Maeda, J. Wu, T. Sawa, Y. Matsumura, K. Hori, *Journal of Controlled Release* **65**, 271 (2000).
29. R. Gref *et al.*, *Science* **263**, 1600 (1994).
30. D. Thassu, M. Deleers, Y. Pathak, *Nanoparticulate drug delivery systems*. (Informa Healthcare, New York, 2007), pp. x, 352 p., [8] p. of plates.
31. E. P. Winer *et al.*, *Journal of Clinical Oncology* **22**, 2061 (2004).
32. W. J. Gradishar *et al.*, *J Clin Oncol* **23**, 7794 (2005).
33. M. E. R. O'Brien *et al.*, *Annals of Oncology: Official Journal of the European Society for Medical Oncology / ESMO* **15**, 440 (2004).
34. R. K. Jain, *Scientific American* **298**, 56 (2008).
35. R. K. Jain, *Journal of Controlled Release* **53**, 49 (1998).
36. R. K. Jain, *Annual Review of Biomedical Engineering* **1**, 241 (1999).
37. R. K. Jain, L. T. Baxter, *Cancer Research* **48**, 7022 (1988).
38. Y. Boucher, L. T. Baxter, R. K. Jain, *Cancer Research* **50**, 4478 (1990).
39. S. D. Perrault, C. Walkey, T. Jennings, H. C. Fischer, W. C. W. Chan, *Nano Letters* **9**, 1909 (2009).
40. T. D. McKee *et al.*, *Cancer Res* **66**, 2509 (2006).
41. P. A. Netti, D. A. Berk, M. A. Swartz, A. J. Grodzinsky, R. K. Jain, *Cancer Research* **60**, 2497 (2000).

42. Z. Ouar *et al.*, *Biochemical Journal* **370**, 185 (2003).
43. A. J. Primeau, A. Rendon, D. Hedley, L. Lilge, I. F. Tannock, *Clinical Cancer Research* **11**, 8782 (2005).
44. R. K. Jain, *Cancer Research* **47**, 3039 (1987).
45. A. I. Minchinton, I. F. Tannock, *Nat Rev Cancer* **6**, 583 (2006).
46. G. Helmlinger, F. Yuan, M. Dellian, R. K. Jain, *Nat Med* **3**, 177 (1997).
47. R. Roy, B. Zhang, M. A. Moses, *Experimental Cell Research* **312**, 608 (2006).
48. E. I. Deryugina, M. A. Bourdon, R. A. Reisfeld, A. Strongin, *Cancer Res* **58**, 3743 (1998).
49. G. Kaul, M. Amiji, *Journal of Drug Targeting* **12**, 585 (2004).
50. M. Stroh *et al.*, *Nat Med* **11**, 678 (2005).
51. X. G. Peng, *Advanced Materials* **15**, 459 (2003).
52. H. Mattoussi, J. Cheon, *Inorganic nanoprobes for biological sensing and imaging*. Artech House series engineering in medicine & biology (Artech House, Boston, 2009), pp. ix, 302 p., 21 p. of plates.
53. M. Nirmal *et al.*, *Nature* **383**, 802 (1996).
54. Y. Chen *et al.*, *Journal of the American Chemical Society* **130**, 5026 (2008).
55. C. B. Murray, D. J. Norris, M. G. Bawendi, *Journal of the American Chemical Society* **115**, 8706 (1993).
56. L. H. Qu, Z. A. Peng, X. G. Peng, *Nano Letters* **1**, 333 (2001).
57. H. Du *et al.*, *Nano Letters* **2**, 1321 (2002).
58. W. W. Yu, J. C. Falkner, B. S. Shih, V. L. Colvin, *Chem Mater* **16**, 3318 (2004).
59. M. A. Hines, P. Guyot-Sionnest, *J Phys Chem-Us* **100**, 468 (1996).
60. W. Liu *et al.*, *Journal of the American Chemical Society* **130**, 1274 (2008).
61. A. R. Clapp, E. R. Goldman, H. Mattoussi, *Nat. Protocols* **1**, 1258 (2006).
62. J. P. Zimmer *et al.*, *Journal of the American Chemical Society* **128**, 2526 (2006).
63. F. Pinaud, D. King, H. P. Moore, S. Weiss, *Journal of the American Chemical Society* **126**, 6115 (2004).
64. D. Gerion *et al.*, *Journal of Physical Chemistry B* **105**, 8861 (2001).
65. S. Kim, M. G. Bawendi, *Journal of the American Chemical Society* **125**, 14652 (2003).
66. W. Liu *et al.*, *Journal of the American Chemical Society* **132**, 472 (2010).
67. B. Dubertret *et al.*, *Science* **298**, 1759 (2002).
68. X. Y. Wu *et al.*, *Nat Biotechnol* **21**, 452 (2003).
69. T. Pellegrino *et al.*, *Nano Letters* **4**, 703 (2004).
70. H. Mattoussi *et al.*, *Journal of the American Chemical Society* **122**, 12142 (2000).
71. H. S. Han *et al.*, *Journal of the American Chemical Society* **132**, 7838 (2010).
72. H. Y. Shen, A. M. Jawaid, P. T. Snee, *ACS Nano* **3**, 915 (2009).

Chapter 2

Synthesis and Characterization of Size-Changing Nanoparticle Constructs

2.1 Introduction

We have established three main criteria for the multistage size-changing nanoparticle (NP): the nanoparticles' size must change from 100 nm to 10 nm, their surface before and after MMP-2 cleavage needs to be well PEGylated and neutral (to ensure the difference in transport before and after cleaving is only a result of size change), and their sensitivity to cleavage should be at least as high as other reported MMP-2 probes. Satisfying these three criteria simultaneously presented several design and synthetic challenges. However, by optimizing the coupling scheme and the degree of glutaraldehyde cross-linking, we were able to meet the desired criteria for this system while preserving the simplicity in design to ensure scalability.

Since both the carrier and released nanoparticles need to be highly PEGylated and neutral. We initialized used DHLA-PEG QDs, which had a relatively “sticky” surface (low coverage of PEG), and allowed for encapsulation inside the core of 100-nm gelatin nanoparticle, but the particle after cleavage showed a broad size distribution by gel filtration chromatography (GFC), indicating binding to gelatin/glutaraldehyde fragments. An alternative strategy was to covalently attach the QDs onto the

gelatin NP surface. Though this approach is susceptible to interparticle cross-linking, through careful optimization and utilizing EDC/sulfo-NHS chemistry to conjugate amino-PEG QDs to the carboxylic acid groups on the gelatin NP surface, we produced nearly monodisperse QD-Gelatin NPs that released cleaved QDs sans size increase.

By controlling the length and degree of glutaraldehyde polymerization used to cross-link the gelatin nanoparticles, we were able to optimize the size of the QDs after cleaving and their rate of release while maintaining particle stability. The method for gelatin nanoparticle synthesis developed in (1) produced gelatin NPs with long extended networks of glutaraldehyde on their surface to maintain particle stability in aqueous solution. However, when the same scheme was applied to our design, the QDs remained covalently attached to this large glutaraldehyde polymer after MMP-2 degradation, resulting in QDs that were significantly larger upon release. To produce released QDs without augmenting their size, we constructed a network of numerous short cross-links on the gelatin particles instead. Since glutaraldehyde readily self-polymerizes in solution, we used nearly monomeric glutaraldehyde (grade I) for consistent formation of short glutaraldehyde polymer cross-links. In addition, using grade I glutaraldehyde improved the MMP-2 cleaving rate considerably such that the release is as sensitive as previously reported MMP-2 probes. By modifying the degree of cross-linking on the gelatin nanoparticle, we optimized the QD-Gelatin NPs to be highly responsive to MMP-2 degradation while preserving particle stability in storage for at least 48 days.

2.2 Materials and Methods

2.2.1 Materials

Gelatin type A ~175 bloom from porcine skin, glutaraldehyde solution (grade I, 50%), glutaraldehyde solution (grade II, 25%), glutaraldehyde solution (no grade/grade X, 50%), N-Hydroxysulfosuccinimide Sodium salt (sulfo-NHS), N-(3-Dimethylaminopropyl)-N'-ethylcarbodiimide hydrochloride (EDC),

methoxypolyethylene glycol amine 5,000 (mPEG-amine 5 kDa), agarose, Collagenase from *Clostridium histolyticum* Type I, Trysin 10x solution, α -lipoic acid, Tetraethylorthosilicate 99.999% (TEOS), cyclohexane, polyoxyethylene (5) nonylphenylether (Igepal CO-520), and ammonium hydroxide (28% in water), and Ethylenediaminetetraacetic Acid, Disodium Salt Dihydrate (EDTA) were purchased from Sigma-Aldrich. Acetone, HEPES, and 10x PBS Liquid Concentrate were purchased from EMD Chemicals Inc. (Gibbstown, NJ). Calcium chloride, isopropyl alcohol, and glycine were obtained from Mallinckrodt Baker Inc. (Phillipsburg, NJ). Qdot® 565 ITK™ amino (PEG) quantum dot and GIBCO® Certified Heat-Inactivated Fetal Bovine Serum was obtained from Invitrogen (Eugene, Oregon). Block™ Casein in PBS was purchased from Thermo Scientific (Rockford, IL). Water was obtained using a Barnstead NANOpure® Diamond Life Science UV/UF TOC water system (Thermo Fisher Scientific, Suwanee, GA). MethoxyPEG-silane (MW 5000 and 1000) were obtained from Laysan Bio Inc, silica spheres 100 nm in diameter were purchased from Polysciences. Syntheses of water soluble PIL-coated QDs and CdSe/CdS core/shell QDs are published elsewhere (2). All reagents were used as obtained without further purification.

2.2.2 Synthesis of DHLA-PEG QD Peptide Silica Nanoparticles

QD-Silica Construct. The QD-silica constructs were obtained from Dr. Zoran Popović (3). Prior to synthesis procedure, the amount of QD to be added to silica spheres was estimated by DLS titration. Aliquots of an aqueous stock solution of poly-imidazole-PEG (PIA)-coated QDs (2) (CdSe/CdS, 1-2 μ M, 10 μ L) were added to a stirred solution of a known amount of silica in water. After each addition step, DLS measurements were performed up to the aliquot when the first change in size distribution by volume was observed. The sum of added aliquots preceding the final addition was taken as a maximum loading amount of QDs for that silica batch. On average $30\text{-}50 \times 10^{-12}$ moles of QDs in water per milligram of silica spheres were added. In a typical synthesis experiment for 100 nm silica spheres, 10 mg of spheres (178 μ L of original 5.6% solution from Polysciences) were added to 10 ml water and sonicated for 10 min. To this solution, the previously determined quantity of PIA-coated QDs was added in 10 μ L

aliquots. Then, 15 μL of TEOS and 50 μL of 28% aqueous ammonium hydroxide were added, followed by 25 mg of amino-PEG5kDa-silane and 25 mg of methoxy-PEG5kDa-silane in 1 mL of water. The vigorously stirred reaction mixture was kept at 70°C for 3.5 h and at RT for an additional 12 h after which it was centrifuged three times from water at 10000 RPM for 25 min, dispersed in 5 mL of water, sonicated, and passed through 0.45 μm filter. Obtained particles were stored at 4 C.

QD-Silica-Peptide Construct. We next conjugated the QD-Silica construct with a peptide (HHHHHHGPLGLAGGGC) using sulfo-SMCC. The QD-Silica construct (50 μL of ~ 3 nM) was incubated with 2 mg of sulfo-SMCC for 30 minutes. The QD-Silica-(sulfo-SMCC) conjugate was centrifuged three times from water at 10000 RPM for 10 min and dispersed in ~ 300 μL of water. The purified solution was then combined with 20 mg of the cleavable peptide and incubated for 30 minutes. The QD-Silica-peptide conjugate was centrifuged three times from water at 10000 RPM for 10 min and dispersed in ~ 300 μL of water each time.

QD-Silica-Peptide-QD Construct. The QD-Silica-Peptide construct was added slowly to a solution of 30 μL of ~ 615 nm emitting DHLA-PEG QDs. The solution was allowed to incubate for 30 minutes. The QD-Silica-peptide was centrifuged three times from water at 10000 RPM for 10 min and dispersed in ~ 300 μL of water.

2.2.3 Synthesis of DHLA-PEG QD Gelatin Nanoparticles

Gelatin nanoparticles were prepared from a modification of the two-step desolvation method developed in (1). Gelatin type A (1.25 g) was added to 25 mL of DI water and heated at 45°C until dissolution. The solution was then removed from heat and 25 mL of acetone was added to the solution at 12 mL/min while stirring slowly. After the acetone addition was completed, the stirring was turned off. After exactly 30 seconds, the supernatant containing the low molecular weight gelatin fraction was removed. DI water (25 mL) was added to the remaining precipitate and heated again to 40°C until dissolution. 6 mL of the solution was removed and the pH of the removed fraction was adjusted to ~ 2.5 with HCl solution. A 25 μL of ~ 6 μM solution of DHLA-PEG QDs was added to the gelatin solution.

Under fast stirring and 45°C, 72 mL of acetone was added at 1 mL/min. After the acetone addition was completed, 25 µL glutaraldehyde (no grade/grade X) was diluted in 500 µL of water and added to the gelatin nanoparticles 25 µL at a time over about 3 minutes. Subsequently, the solution was kept at 40°C and fast stirring for various times (from 1 hr to 12 hrs). The acetone was then rotavapped off slowly. The remaining solution was filtered through a 0.2 µm syringe filter. A solution of 10x PBS was added for a final solution of ~1x PBS with a pH of ~7. Instead of centrifugation to purify the nanoparticles, we used GFC to prevent aggregation and an increase in size. A 1 mL solution of the gelatin particles was injected into a Superose™ 6 GL 10/300 column (GE Healthcare, Piscataway, NJ) with 1x PBS as the mobile phase. The peak eluting at the void volume was combined and concentrated using house vacuum very gently. Amino-PEG (50 mg) was added into the DHLA-PEG gelatin particle solution along with EDC (~10 mg). The solution was incubated for 3 hrs and purified again with GFC.

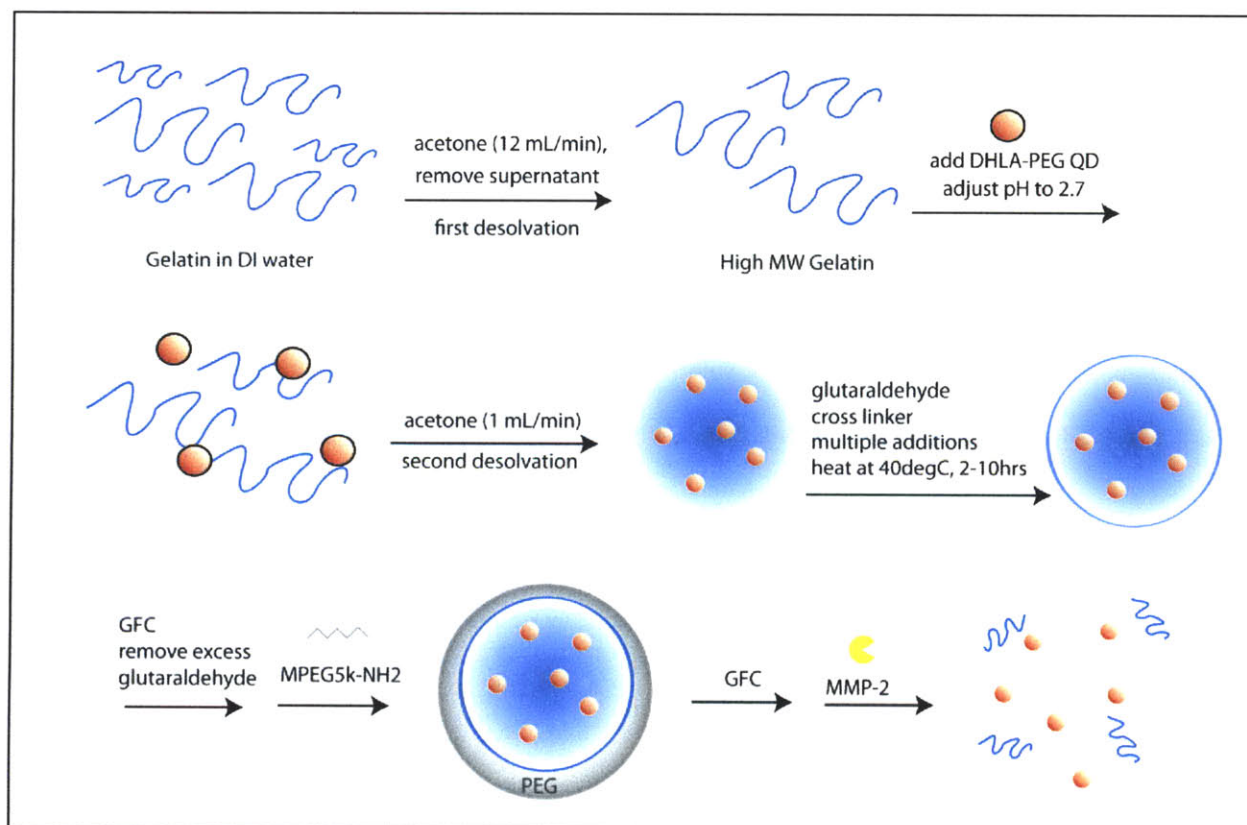


Figure 2.1 Synthetic Scheme for DHLA-PEG QD Gelatin Nanoparticles.

2.2.4 Synthesis of Imidazole-PEG QD encapsulated Gelatin Nanoparticles

Gelatin nanoparticles were prepared from a modification of the two-step desolvation method developed in (1). Gelatin type A (1.25 g) was added to 25 mL of DI water and heated at 45°C until dissolution. The solution was then removed from heat and 25 mL of acetone was added to the solution at 12.5 mL/min while stirring slowly. After the acetone addition was completed, the stirring was turned off. After exactly 30 seconds, the supernatant containing the low molecular weight gelatin fraction was removed. DI water (25 mL) was added to the remaining precipitate and heated again to 40°C until dissolution. 6 mL of the solution was removed and the pH of the removed fraction was adjusted to ~2.7 with HCl solution. A 25 μ L of ~6 μ M solution of imidazole-PEG QDs was added to the gelatin solution. The QDs' fluorescence was lost immediately after addition into the gelatin solution. Under fast stirring and 40°C, 72 mL of acetone was added at 1.5 mL/min. After the acetone addition was completed, 25 μ L glutaraldehyde (no grade/grade X) was diluted in 500 μ L of water and added to the gelatin nanoparticles 25 μ L at a time over about 3 minutes. Subsequently, the solution was kept at 45°C and fast stirring for various times (from 1 hr to 12 hrs). The acetone was then rotavapped off slowly. The remaining solution was filtered through a 0.2 μ m syringe filter. A solution of 10x PBS was added for a final solution of ~1x PBS with a pH of ~7. Instead of centrifugation to purify the nanoparticles, we used GFC to prevent aggregation and an increase in size. A 1 mL solution of the gelatin particles was injected into a Superose™ 6 GL 10/300 column (GE Healthcare, Piscataway, NJ) with 1x PBS as the mobile phase.

2.2.5 Synthesis of Imidazole-PEG QD coated Gelatin Nanoparticles

Synthesis of Gelatin Nanoparticle. Gelatin nanoparticles were prepared from a modification of the two-step desolvation method developed in (1). Gelatin type A (0.625 g) was added to 12.5 mL of DI water and heated at 40°C until dissolution. The solution was then quickly removed from heat and 12.5 mL of acetone was added to the solution at 6.0 mL/min while stirring at 300 rpm. After the acetone addition was completed, the stirring was turned off. After exactly 1 min, the supernatant containing the low molecular

weight gelatin fraction was removed. DI water (12.5 mL) was added to the remaining precipitate and heated again to 40°C until dissolution. Half the solution was removed and the pH of the remaining half was adjusted to 2.7 with a 1 M HCl solution. Under constant stirring at 600 rpm and 40°C, 20.75 mL of acetone was added at 1 mL/min. Following addition of ~17 mL of acetone, the solution appeared cloudy white from the scattering by gelatin particles being formed. After the acetone addition was completed, 30 μ L of 50% glutaraldehyde solution (no grade/grade X) diluted in 1 mL acetone was added to the gelatin solution at 0.05 mL/min to cross-link the particles. Subsequently, the solution was kept at 40°C and 600 rpm stir rate for 7.5 hours. The acetone was then rotavapped off slowly to a final volume of 5-6 mL. The remaining solution was filtered through a 0.2 μ m syringe filter. A 1 M glycine solution (0.2 mL) was added and the solution was stored overnight at 4°C. Instead of centrifugation to purify the nanoparticles, we used GFC to prevent aggregation and an increase in size. A 1 mL solution of the gelatin particles was injected into a Superose™ 6 GL 10/300 column with 1x PBS as the mobile phase. The peak eluting at the void volume was collected with 0.5 mL fractions. The first two concentrated fractions were combined. This 1 mL solution was then taken to the next step for QD conjugation and PEGylation.

Synthesis of Imidazole-PEG QD coated Gelatin NPs. The 1 mL gelatin nanoparticle solution was combined with 20 μ L of 8 μ M Imidazole-amino-PEG QDs, and the solution was stirred at 130 rpm for 30 minutes. Afterwards, the pH was changed to 5 and then immediately adjusted to pH 6. Stirring continued for 30 minutes. EDC (0.4 mg, 2.1 μ mol) and sulfo-NHS (0.4 mg, 1.9 μ mol) was dissolved in 50 μ L of DI water and then added to the gelatin nanoparticle/QD mixture. The reaction proceeded for 3 hours. The resulting mixture was filtered through a 0.2 μ m syringe filter and then purified using GFC with the Superose™ 6 column. The mobile phase used was 50 mM HEPES buffer at pH 7.5 for subsequent *in vitro* characterization of the QD Gelatin NP s or 1x PBS at pH 7.4 for subsequent *in vivo* experiments. The peak eluting at the void volume was collected with 0.5 mL fractions and the first concentrated fraction was used for further experiments.

2.2.6 Synthesis of Polyacrylic Acid-PEG QD-Peptide-Gelatin Nanoparticles

Synthesis of Gelatin Nanoparticle. Gelatin nanoparticles were prepared from a modification of the two-step desolvation method developed in (1). Gelatin type A (0.625 g) was added to 12.5 mL of DI water and heated at 40°C until dissolution. The solution was then quickly removed from heat and 12.5 mL of acetone was added to the solution at 6.0 mL/min while stirring at 300 rpm. After the acetone addition was completed, the stirring was turned off. After exactly 1 min, the supernatant containing the low molecular weight gelatin fraction was removed. DI water (12.5 mL) was added to the remaining precipitate and heated again to 40°C until dissolution. Half the solution was removed and the pH of the remaining half was adjusted to 2.7 with a 1 M HCl solution. Under constant stirring at 600 rpm and 40°C, 20.75 mL of acetone was added at 1 mL/min. Following addition of ~17 mL of acetone, the solution appeared cloudy white from the scattering by gelatin particles being formed. After the acetone addition was completed, 30 μ L of 50% glutaraldehyde solution (grade X) diluted in 1 mL acetone was added to the gelatin solution at 0.05 mL/min to cross-link the particles. Subsequently, the solution was kept at 40°C and 600 rpm stir rate for 5 hours. The acetone was then rotavapped off slowly to a final volume of 5-6 mL. The remaining solution was filtered through a 0.2 μ m syringe filter. A 1 M glycine solution (0.2 mL) was added and the solution was stored overnight at 4°C. Instead of centrifugation to purify the nanoparticles, we used GFC to prevent aggregation and an increase in size. A 1 mL solution of the gelatin particles was injected into a Superose™ 6 GL 10/300 column with 1x PBS as the mobile phase. The peak eluting at the void volume was collected with 0.5 mL fractions.

QD-peptide. A 45 μ L of a 8 μ M Qdot® 565 ITK™ amino (PEG) QDs solution was mixed with sulfo-SMCC (0.2 mg) in 0.5 mL of PBS solution. The sulfo-SMCC was fully dissolved first in PBS before addition to QDs. The reaction was allowed to proceed for 30 minutes and then the solution was dialyzed 2x with a 50 kDa spin dialysis filter. The cleavable peptide linker (0.267 mg) was then added (1000x fold excess) and allowed to react for 2 hours. The solution was again dialyzed 2x with a 50 kDa spin dialysis filter to remove excess peptides.

QD-peptide Gelatin construct. The QD-peptide construct from the previous step was added to 200 μL of Gelatin NP after the first GFC purification. The pH was adjusted to ~ 6 and then 0.45 mg of EDC and 0.15 mg of sulfo-NHS were added. After reaction overnight, a 1 M NaOH solution was added to change the pH to 8 and then incubated for 30 minutes. Next, 25 μL of 50 mM glycine was added and stirred for 1 hour to quench the reaction. The solution was purified using GFC with the Superose™ 6 GL 10/300 column.

2.2.7 Synthesis of Polyacrylic Acid-PEG QD Gelatin Nanoparticles

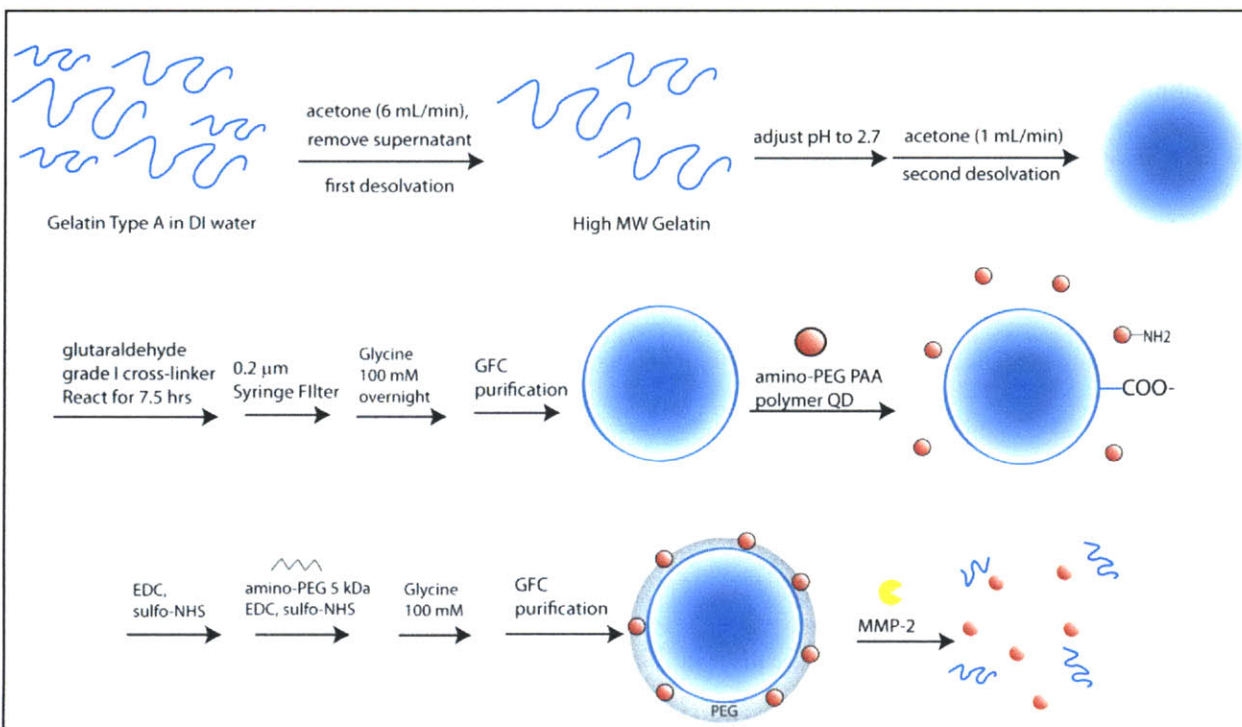


Figure 2.2. Synthetic scheme for Polyacrylic Acid-PEG QD Gelatin Nanoparticles

Synthesis of Gelatin Nanoparticle. Gelatin nanoparticles were prepared from a modification of the two-step desolvation method developed in (1). Gelatin type A (0.625 g) was added to 12.5 mL of DI water and heated at 40°C until dissolution. The solution was then quickly removed from heat and 12.5 mL of acetone was added to the solution at 6.0 mL/min while stirring at 300 rpm. After the acetone addition was completed, the stirring was turned off. After exactly 1 min, the supernatant containing the low molecular

weight gelatin fraction was removed. DI water (12.5 mL) was added to the remaining precipitate and heated again to 40°C until dissolution. Half the solution was removed and the pH of the remaining half was adjusted to 2.7 with a 1 M HCl solution. Under constant stirring at 600 rpm and 40°C, 20.75 mL of acetone was added at 1.0 mL/min. Following addition of ~17 mL of acetone, the solution appeared cloudy white from the scattering by gelatin particles being formed. After the acetone addition was completed, 30 μ L of 50% glutaraldehyde solution (grade I) diluted in 1 mL acetone was added to the gelatin solution at 0.05 mL/min to cross-link the particles. Subsequently, the solution was kept at 40°C and 600 rpm stir rate for 7.5 hours. The acetone was then rotavapped off slowly to a final volume of 5-6 mL. The remaining solution was filtered through a 0.2 μ m syringe filter. A 1 M glycine solution (0.2 mL) was added and the solution was stored overnight at 4°C. Instead of centrifugation to purify the nanoparticles, we used GFC to prevent aggregation and an increase in size. A 1 mL solution of the gelatin particles was injected into a Superose™ 6 GL 10/300 column (GE Healthcare, Piscataway, NJ) with 1x PBS as the mobile phase. The peak eluting at the void volume was collected with 0.5 mL fractions. This was repeated once more and the first concentrated fractions from both GFC runs were combined. This 1 mL solution was then taken to the next step for QD conjugation and PEGylation.

Synthesis of Polyacrylic Acid-PEG QD Gelatin Nanoparticles. The 1 mL gelatin nanoparticle solution was combined with 20 μ L of 8 μ M Qdot® 565 ITK™ amino (PEG) QDs, and the solution was stirred at 130 rpm for 30 minutes. Afterwards, the pH was changed to 5 and then immediately adjusted to pH 6. Stirring continued for 30 minutes. EDC (0.4 mg, 2.1 μ mol) and sulfo-NHS (0.4 mg, 1.9 μ mol) was dissolved in 50 μ L of DI water and then added to the gelatin nanoparticle/QD mixture. The reaction proceeded for 3 hours. Afterwards, a solution of mPEG amine 5 kDa (20 mg, ~4 μ mol) dissolved in 50 μ L of DI water was added to the gelatin/QD solution. Then an additional solution of EDC (0.4 mg) and sulfo-NHS (0.4 mg) dissolved in 50 μ L of DI water was added. After two hours, the pH was adjusted to 8 and stirring continued for 1 hour. A 1 M glycine solution (50 μ L) was added to quench the reaction. After 30 minutes, the resulting mixture was filtered through a 0.2 μ m syringe filter and then purified using GFC

with the Superose™ 6 column. The mobile phase used was 50 mM HEPES buffer at pH 7.5 for subsequent *in vitro* characterization of the QD-Gelatin NPs or 1x PBS at pH 7.4 for subsequent *in vivo* experiments. The peak eluting at the void volume was collected with 0.5 mL fractions and the first concentrated fraction was used for further experiments.

2.2.8 Size Measurement

SEM. SEM samples were prepared by desalting the nanoparticle suspension two times using GFC with DI water as the mobile phase. Then a 1:1 mixture of the resulting nanoparticle suspension in DI water and acetone was drop-casted on a p-doped silicon substrate (University Wafer, South Boston, MA). The sample was dried in air overnight, and then the surface was sputter coated with ~3 nm of gold-palladium. Images were taken on a FEI/Philips XL30 field emission gun environmental scanning electron microscope. Size analysis was performed by manually measuring 170 particles using ImageJ.

DLS. The measurements of nanoparticle hydrodynamic diameter were carried out on a DynaPro Titan Dynamic Light Scatterer in pH ~7.5 50 mM HEPES buffer at 25°C. The result is the average of five measurements of 10 acquisitions each.

2.2.9 Zeta Potential

The measurements of nanoparticle ζ -potential were carried out on a Malvern Instruments ZetaSizer ZS90 with the Universal Dip Cell at 25°C. For the measurements, 20 μ L of nanoparticle suspension was dispersed in 800 μ L of 50 mM HEPES buffer at either pH ~7.5 or ~6.0. The result is the average of five measurements of 20 acquisitions each.

2.2.10 Fluorescence

Fluorescence spectroscopy was measured on a FluoroMax-3 (Horiba Jobin Yvon Inc., Edison, NJ). For fluorescence microscopy of the size-changing NPs on a silicon substrate, a Nikon Eclipse ME600 epifluorescence optical microscope equipped with a Nikon DXM1200 digital camera was used.

2.3.11 Gel Filtration Chromatography (GFC)

The samples before and after cleaving with trypsin or collagenase were directly analyzed by GFC with a Superose™ 6 GL 10/300 column (GE Healthcare, Piscataway, NJ) or a YMC-Pack Diol-200 (8 x 250 mm) on an Agilent 1100 series HPLC with an in-line degasser, autosampler, diode array detector, and fluorescence detector (Roseville, CA). The injection volume was 45 μ L and the mobile phase was 1x PBS (pH 7.4) at a flow rate of 0.5 mL/min. The GFC chromatograms were detected by fluorescence detection at 250 nm excitation wavelength and 565 nm emission wavelength or the entire emission spectrum from 500-650 nm was collected.

2.3.12 Fluorescence correlation spectroscopy (FCS)

FCS measurements were carried out on a custom-built inverted confocal microscopy setup equipped with a Nikon Plan Apo VC (60x, 1.2 N.A.) water immersion objective. The 514 nm laser line from an argon-krypton-ion laser (Innova 70C, Coherent Inc., Santa Clara, CA) at 6.2 μ W (measured at the back aperture of the objective) was used for excitation. The emission was collected through the same objective and spatially filtered by focusing through a 25 μ m pinhole. Following a 550 nm long-pass filter, the fluorescence was split using a 50-50 beamsplitter and recorded using avalanche photodiodes (SPCM-AQR-13, Perkin Elmer, Shelton, CT). Cross-correlation was performed using a digital correlator (ALV7004-FAST, ALV, Langen, Germany) and correlogram fitting was performed from lag time (τ) 7.0 x 10⁻⁴ ms to 2.35 x 10⁴ ms using the ALV software. Sample carriers were formed by sealing a silicone perfusion chamber (PC8R-2.5, Grace Bio-Labs Inc., Bend, OR) over a 22 x 50 mm glass coverslip (VWR, Pittsburgh, PA). The cover slip surface was pretreated with casein/PBS solution to prevent non-

specific binding. HEPES (50 mM, pH 7.5) was used as the solvent. The QD suspension was diluted to ~0.2 mg/mL. The temperature during the measurement was ~296°K. Five to ten measurements with acquisition times of 60 seconds each were performed for each sample.

FCS Analysis. In our confocal setup, the axial dimension of the focal volume is significantly larger than the lateral dimensions. Hence, it is sufficient to fit the cross-correlation function using the isotropic 2D translational diffusion model,

$$g(\tau) = \frac{1}{N_p} \frac{1}{(1+\tau/\tau_D)} \quad (3.1)$$

This allows us to obtain the correlation time for each measurement. Then we calculate the diffusion coefficient using the equation:

$$D = \omega^2/4\tau_D \quad (3.2)$$

The radius of the confocal detection volume (ω) was obtained using 0.10 μm calibration standards (R100, Thermo Scientific) and the QDs. Diffusion coefficients from repeated measurements were averaged. Hydrodynamic radius was obtained from the mean diffusion coefficient using the Einstein-Stokes equation:

$$D = \frac{k_B T}{6\pi\eta r} \quad (3.3)$$

The value used for viscosity (η) of water at 295.6°K was 9.4×10^{-4} Pa·s.

2.3 Results and Discussion

2.3.1 DHLA-PEG QD Peptide Silica Nanoparticles

Our first attempt to synthesize size-changing NPs was to conjugate DHLA-PEG QDs to the surface of PEGylated SilicaQD NPs through MMP-2 cleavable peptides. The SilicaQD NPs were coated with green-emitting non-cleavable QDs while the cleavable QDs were red-emitting. The two colors allowed us to ascertain the cleavage through the separation of the two colors in our *in vitro* and *in vivo*

experiments. A disadvantage of this structure was that the cleavable peptide was buried in between the red QDs and silica NPs. Moreover, both NPs were shrouded in a forest of PEG, which is known to reduce the enzymatic degradation of peptides. An advantage is the simplicity of observing the cleavage *in vivo* through separation of the red and green fluorescence in the tumor. The synthetic scheme initially involves conjugation of a peptide linker with a polyhistidine tag at the N-terminal, a cysteine at the C-terminal, and an MMP-2 cleavable sequence in between. The thiols on the peptides' cysteines were conjugated to the amino-PEGs activated with sulfo-SMCC on the surface of the SilicaQD NPs. DHLA-PEG QDs were then introduced and they self-assembled onto the SilicaQD NP surface due to the strong binding of polyhistidine onto the surface of DHLA-PEG QDs. The solution was then centrifuged three times with the supernatant containing the free QDs removed and replaced with fresh buffer solution each time. The resulting solution was only weakly fluorescent. The QDs experienced a large drop in quantum yield because of the dilute QD solution and low concentration of free DHLA-PEG ligands after the centrifugation process. Low concentration of free ligands and low QD concentration speeds up the desorption of DHLA-PEG ligands from the QD surface, increasing surface trap sites and particle aggregation. One can add back free DHLA-ligands to mitigate this effect. The cleavable construct was analyzed with GFC using fluorescence detection before and after incubation with collagenase and trypsin (Figure 2.3). The chromatograms obtained before and after incubation with proteases did not show any significant differences. The problems associated with this construct are the low fluorescence intensity and possibly difficulty with cleaving due to the poorly accessible cleavable peptide.

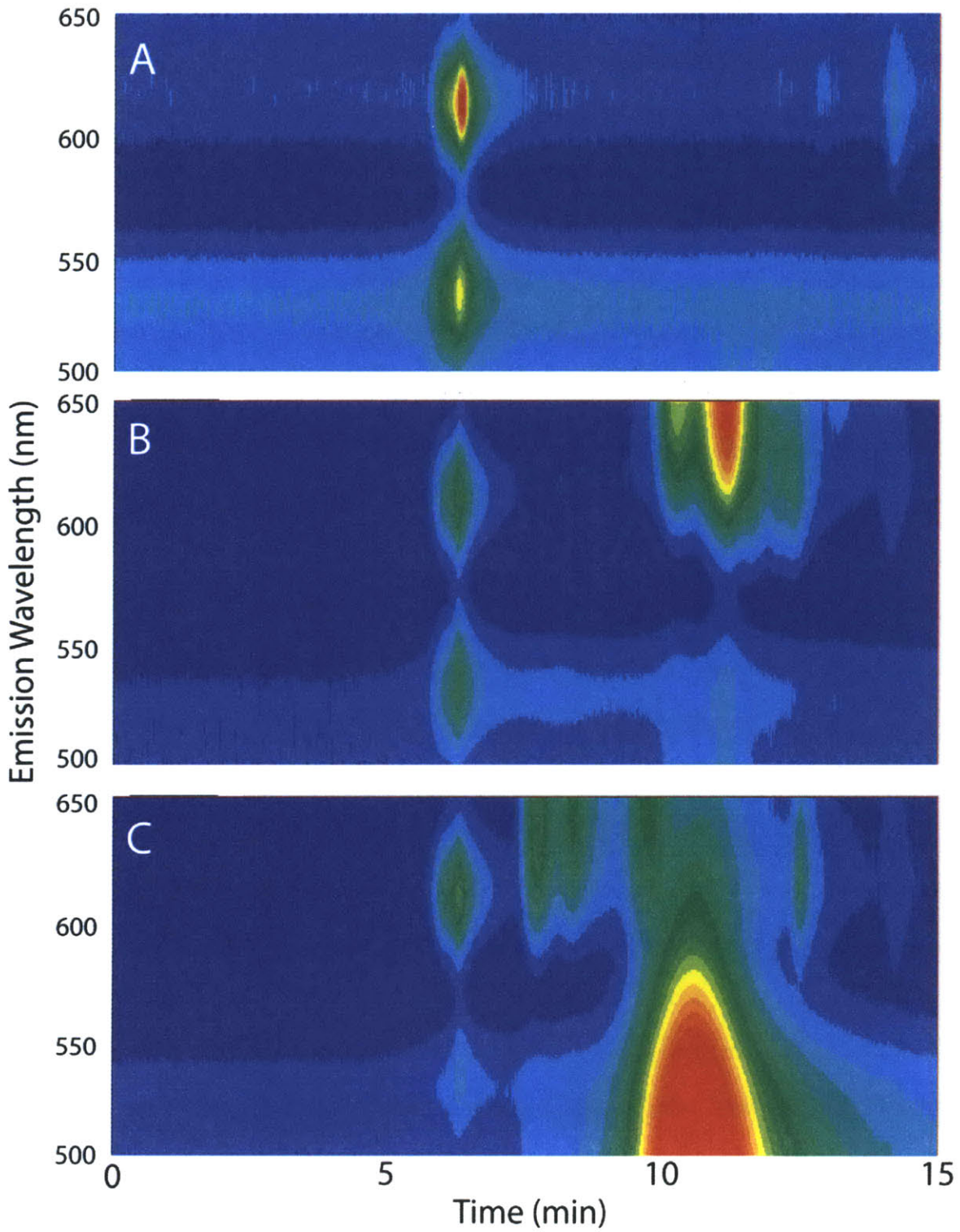


Figure 2.3. Gel-Filtration Chromatograms of DHLA-PEG QD Peptide Silica NPs before cleaving (A) and after cleaving with trypsin (B) and with collagenase (C).

2.3.2 DHLA-PEG QD Gelatin Nanoparticles

We next attempted to construct our size-changing NP to be more sensitive to cleaving. Besides using only peptide linker(s) between the 10-nm small QDs and 100-nm large NPs, another strategy is to design the nanoparticle such that cleavage of each peptide can reduce the steric hindrance for the cleavage of the remaining uncleaved peptides. For example, cleavage of peptides can compromise the PEG fortress on the large NPs' surface or debulk the large NPs, initiating a cascade effect that makes it easier for proteases to access and cleave the rest of the peptides. The more peptides that are critical to maintaining the PEG on the large NPs' surface and/or the structure of the large NPs themselves, the more sensitive the NPs will be to the proteases. Thus the large NPs can be synthesized to be well PEGylated to repel adsorption by serum proteins (avoid opsonization and clearance by RES) but at the same time be highly sensitive toward proteases. We will refer to this enhancement as gain. One scheme of synthesizing such a structure is to conjugate PEG onto the surface of the large NP through a cleavable peptide such that cleavage of peptide also removes a PEG molecule and reduces the PEGylation on the NP surface, making it easier to cleave off additional PEG molecules and small NPs. Such a structure can yield modest gain but synthesis may be expensive and tedious. A substantial amount of cleavable peptide needs to be conjugated to relatively large PEG (> 2 kDa) and then purified with HPLC. Another possible structure is to synthesize a large 100-nm NP that is composed entirely of cleavable peptides and with PEG either incorporated in the particle core and/or the particle surface. Such a structure would yield very high gain; once the cleavage occurs on the surface, the structural integrity of the NP becomes compromised. The protease can penetrate into the NP and cleave from the inside outward, avoiding the thick outer PEG layer. To our knowledge, synthesis of such a NP that also meets our other requirements such as size has not been reported to date. However, instead of using cleavable peptides, gelatin, which is very sensitive to cleavage by MMP-2 and MMP-9, have been made into NPs and explored as a possible nanotherapeutic material due to its nontoxic and low immunogenic properties. In addition, gelatin is low cost, abundant,

and already used as a blood substitute and common additive in pharmaceuticals. These qualities make gelatin highly favorable as the core material for our large NP.

We first attempted to encapsulate the DHLA-QDs into the core of gelatin NPs. The gelatin NPs were synthesized using a method known as two-step desolvation. This method first dissolves gelatin in DI water and then adds a non-solvent (acetone in our case) of gelatin that is miscible with water such that the gelatin precipitates out of solution in a controlled fashion. In the first desolvation step, acetone is added into the gelatin solution causing the high molecular weight (MW) gelatin to precipitate and collect onto the bottom of the reaction vessel. The low MW gelatin is removed because this fraction is known to cause particle instability if it is incorporated into the final gelatin NP. The high MW fraction is then redissolved in water and the pH adjusted (typically to ~ 2.7) such that it is far from the gelatin's isoelectric point. During the second desolvation step, the addition of acetone (non-solvent) causes the gelatin to phase separate from solution again. But this time, the gelatin has a higher charge (due to the large difference in pH from the isoelectric point) and thus higher electrostatic repulsion from each other. Instead of precipitating together all out of solution to the bottom of the reaction vessel, the gelatin forms small clumps or nanoparticles instead because of their electrostatic repulsion. afterward, a solution of glutaraldehyde (grade X) is added to cross-link the gelatin NPs so that they are stable after transferring them back into water. After reaction for several hours (varied from 2 to 10), the gelatin NPs are purified using GFC.

By adding a solution of DHLA-PEG QDs into the gelatin solution before the second desolvation step, we were able to encapsulate the DHLA-PEG QDs into the gelatin NPs during the NP formation process. Because the DHLA-PEG QDs are relatively “sticky” to proteins (Figure 2.8), these QDs bound to the gelatin (Figure 2.7) and were incorporated with high efficiency. Dynamic light scattering (DLS) measurements of these particles showed a hydrodynamic diameter of 96.6 nm (Figure 2.4c). The QD-Gelatin NPs preserved the fluorescence spectrum of the QDs that they were synthesized from (Figure 2.4b). The absorption spectrum was dominated from scattering by the large large gelatin NPs (Figure

2.4d). Scanning electron microscopy (SEM) confirmed the particles were not aggregated and relatively monodisperse.

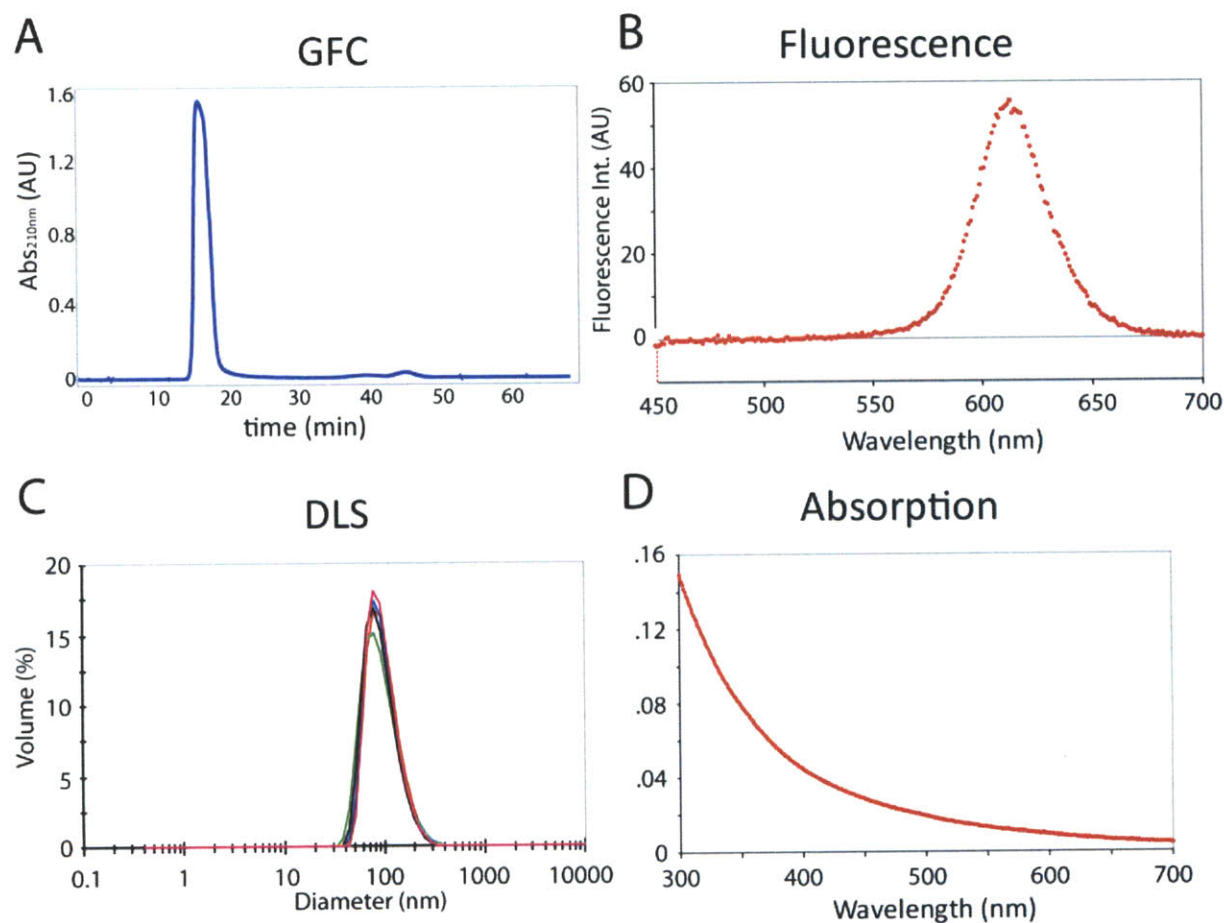


Figure 2.4 Physical Characterization of DHLA-PEG QD Gelatin NPs. (A) Gel-filtration chromatogram, (B) fluorescence spectrum, (C) dynamic light scattering, and (D) absorption (scattering) spectrum

Centrifugation, scattering, and GFC were used to determine the size change of the NPs.

Incubation of these NPs with trypsin followed by centrifugation of the particles for 5 minutes at 3 krpm indicated a size change had occurred (Figure 2.6). However, GFC analysis of the sample after cleaving with collagenase showed the cleaved QDs had broad size distribution. GFC analysis of only DHLA-PEG QDs incubated with gelatin and collagenase showed a similar chromatogram, suggesting the cleaved gelatin fragments can bind to the surface of the DHLA-PEG QDs and result in large sized structures (Figure 2.7).

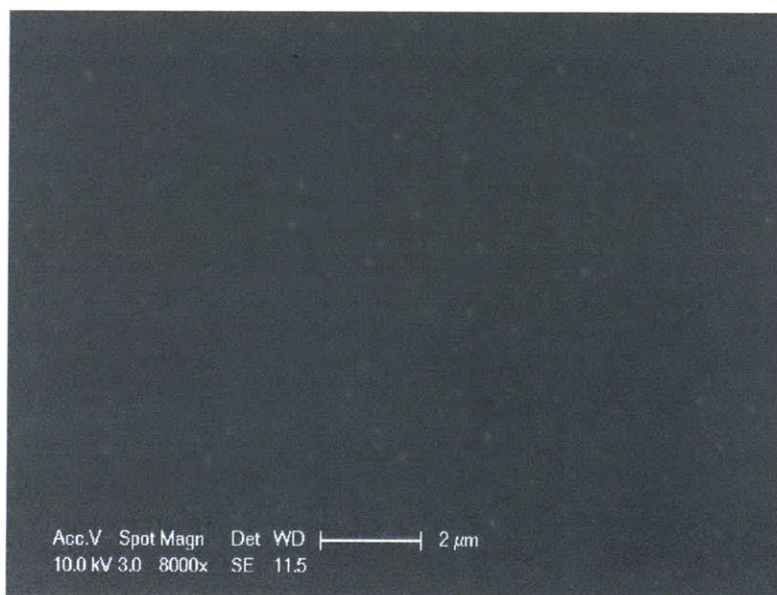


Figure 2.5. SEM of DHLA-PEG QD Gelatin NPs

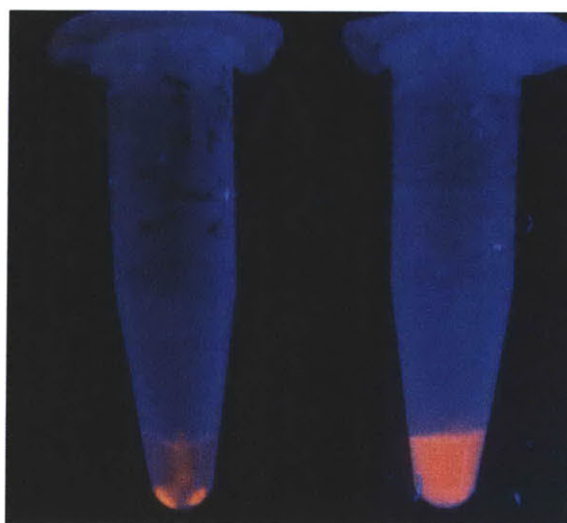


Figure 2.6. Images of DHLA-PEG QD Gelatin NP solution after centrifugation and before (left) or after (right) incubation with trypsin.

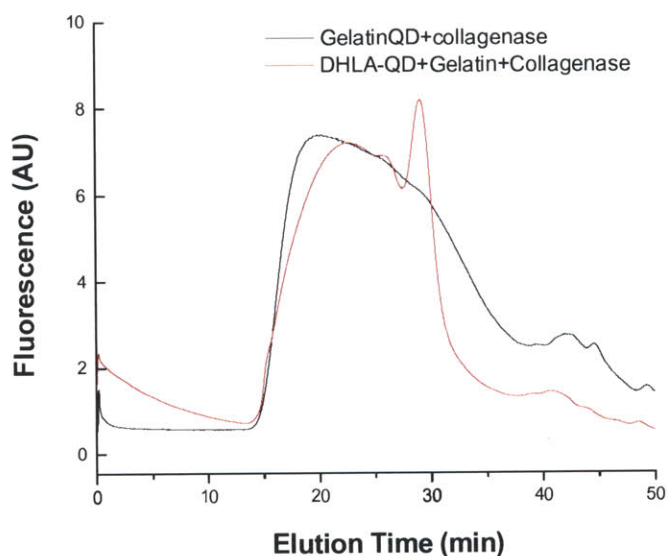


Figure 2.7. GFC chromatogram comparison of DHLA-PEG QD Gelatin NP after incubation with collagenase and DHLA-PEG QD with Gelatin after incubation with collagenase.

2.3.3 Imidazole-PEG QD encapsulated Gelatin Nanoparticles

The synthesis of the imidazole PEG QD encapsulated Gelatin NPs was the same as the previously discussed DHLA-PEG QD-Gelatin nanoparticles except the DHLA-PEG QDs were replaced with imidazole-PEG QDs (PIA) (2), which are much less “sticky” to proteins. The immediate problem we encountered with the PIA QDs was their instability at the low pH range usually used (~ 2.7) for the second desolvation step during gelatin NP synthesis. The imidazoles on the water-solubilizing polymers are the key linkages that bind the polymer onto the QDs’ surface. At pH lower than the pK_a of imidazole (~ 6), the imidazoles become protonated and the polymer begins to dissociate from the QDs’ surface, resulting in loss of QD fluorescence and precipitation of the QDs. The QDs lost their fluorescence rapidly after being introduced into the low pH gelatin solution. The second desolvation can also be performed at high pH (~ 12), which the QDs are very stable in. However, because the PIA QDs are much less “sticky” (high coverage of PEG) to the gelatin (Figure 2.8), most of the QDs were not incorporated into the gelatin NP.

2.3.4 Imidazole-PEG QD coated Gelatin Nanoparticles

Instead of encapsulating the “non-sticky” PIA QDs in the gelatin NP core, we conjugated the PIA QDs to the surface of the gelatin nanoparticle. The gelatin NPs were first formed, purified using GFC, conjugated to the PIA QDs, and then purified using GFC again. We conjugated amine-functionalized PIA QDs to the carboxylic acid groups on the surface of the gelatin NP using EDC/sulfo-NHS coupling chemistry.

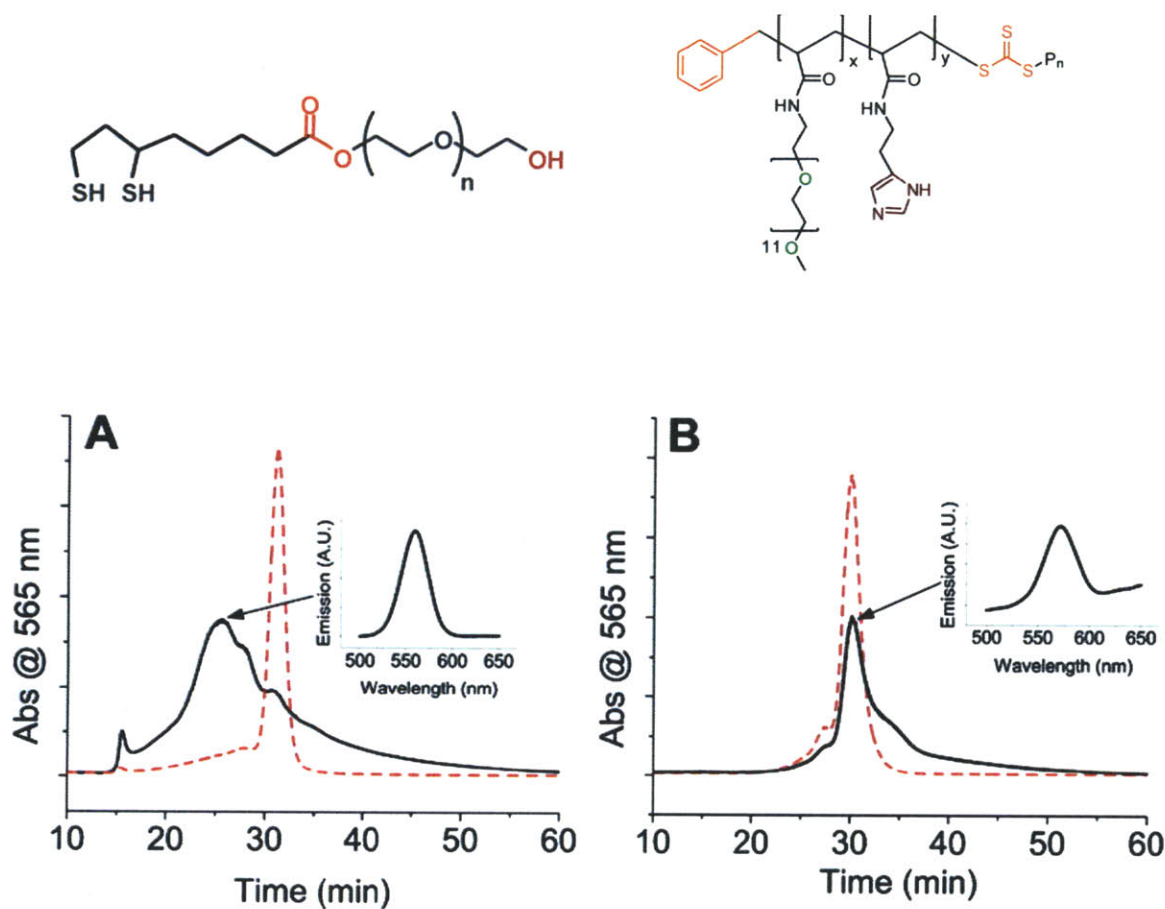


Figure 2.8. Comparison of GFC chromatograms of DHLA-PEG QD with 95% FBS (A) and imidazole-PEG QD with 95% FBS (B).

However, the amines which we expected to be available for conjugation were actually binding to the surface of the QDs, greatly reducing their conjugation efficiency. The conjugation efficiency was very

low resulting in only 1-5 QD per gelatin nanoparticles when ~80 QDs were introduced per gelatin NP (measured from ICP-OES of QDs and Mie Scattering of Gelatin NPs). Using fluorescence correlation spectroscopy (FCS), we were able to measure the size of the cleaved QDs after incubation with collagenase (Figure 2.9). The FCS measurement showed the cleaved QDs were 27.9 nm (Table 2.1), almost three times bigger than the size of the individual QDs. We postulated the large size was due to attachment of the cleaved QDs to the large glutaraldehyde network that is not cleavable by proteases. We also attempted to observe the cleaving *in vivo* for these cleavable constructs using the HT-1080 tumor model. However, due to the low fluorescence intensity, we had difficulty imaging these particles in the tumor. These two problems brought about a necessity to experiment with other QD gelatin NP constructs.

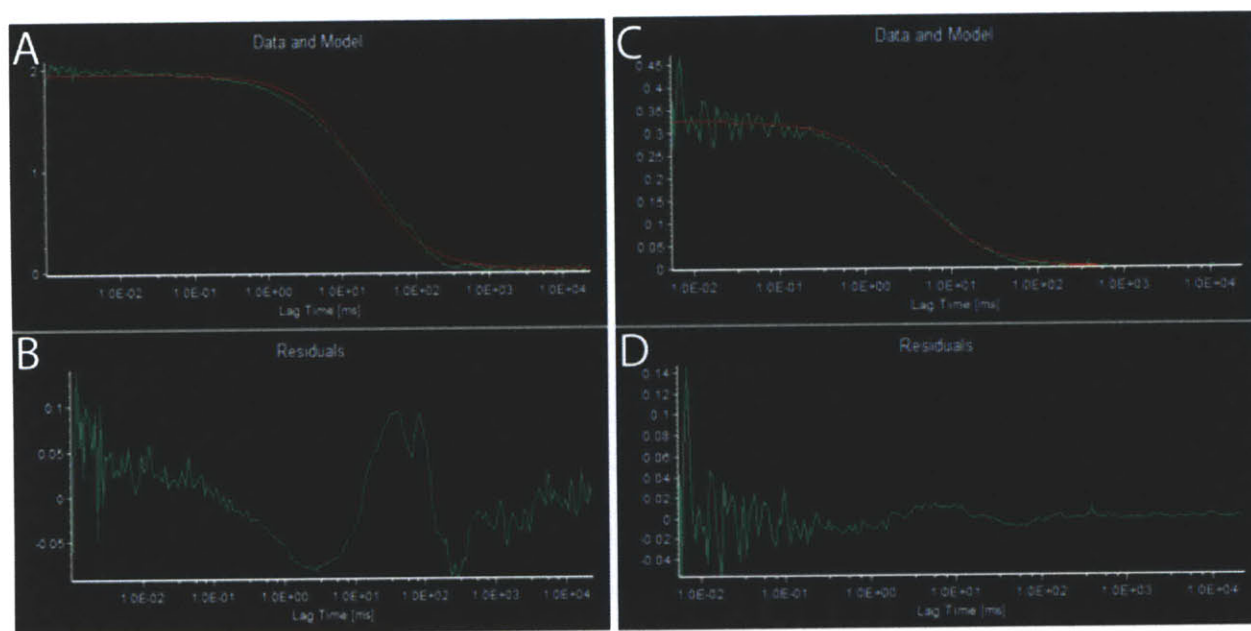


Figure 2.9. FCS correlograms of Imidazole-PEG QD Gelatin NPs synthesized using grade X glutaraldehyde before incubation with collagenase (A) with residuals (B) and after incubation with collagenase (C) with residuals (D).

Sample	FCS (corr. time)	DLS (nm)	DLS/FCS
GelatinQD	18.19	137.2	7.5426
Gelatin QD After Collagenase	3.769		
QD	1.405	10.58	7.5302
SilicaQD	18.05	131.3	7.2742

Size after cleaving with collagenase by FCS: 27.9 nm

Table 2.1. Size of QDs, SilicaQDs, and Imidazole-PEG QD Gelatin NPs before and after cleaving with collagenase,.

2.3.5 Polyacrylic Acid QD-Peptide-Gelatin Nanoparticles

Instead of imidazole-PEG QDs, we switched to Invitrogen Qdot® 565 ITK™ amino (PEG) QDs based on the polyacrylic acid (PAA) PEG polymer for water solubilization. The PAA QDs (emitting at 565 nm) exhibited a high quantum yield (~70%) and the amines were more readily available for conjugation, thus resulting in brighter size-changing NPs. Conjugation of the PAA directly to the surface of the gelatin NP using EDC/sulfo-NHS coupling chemistry will be discussed in detail in the next section. Because we believed the QDs were still attached to the large cross-linked glutaraldehyde network after cleaving, we attempted to conjugate the QDs to the surface of the gelatin NP through a cleavable peptide linker. The protease may be able to cleave the peptide linker and free the QDs from the glutaraldehyde network. In order to prevent the QD from conjugating directly to the gelatin NP surface, we tried to saturate the surface of the QD with cleavable peptides first before conjugating to the surface of the gelatin NP. The synthesis resulted in large amounts of aggregates, probably a result of interparticle cross-linked structures. Because both the QDs and gelatin NPs are multivalent, the conjugation is inevitably susceptible to interparticle cross-linking. One way to avoid interparticle cross-linking is to use a monovalent nanoparticle for the 10-nm nanoparticles, but an efficient method of synthesizing monovalent QDs has not yet been developed. Another strategy to avoid interparticle cross-linking is to use a large

excess of the QDs and add the gelatin NPs to the QDs slowly. However, in order to get high loading, the gelatin NPs need to have high number of reactive sites on their surface, which increases the number of QDs necessary to prevent interparticle cross-linking. Thus to obtain both high loading and prevent interparticle cross-linking, we need a very large excess of QDs to the gelatin NPs. Such a synthesis scheme is very wasteful and is not practical for scale-up. It is possible to salvage the free small nanoparticles after each reaction and use them again for subsequent reactions. But this method leads to possible problems with the quality of the small nanoparticles after each reaction cycle. A practical way to carry out this reaction is to react with only a limited number of reactive sites on the surface of the large nanoparticles so that the probability of interparticle cross-linking is minimized and a very large excess of QDs is not necessary. We lowered the amount of conjugation reagent to minimize interparticle cross-linking which appeared successful. But this construct still yielded cleaved QDs that were much larger than individual QDs. The problem may be that the peptides did not fully saturate the QD surface. We moved on to another scheme, but it should be noted that further increase of the QD loading will require careful optimization of the conjugation efficiency while avoiding interparticle cross-linking.

2.3.6 Polyacrylic Acid-PEG QD Gelatin Nanoparticles

We conjugated the amines on the PAA QDs directly to the carboxylic acid groups on the gelatin NP surface using EDC/sulfo-NHS chemistry. GFC analysis of this construct after incubation with collagenase showed most of the QDs eluted at the void volume (Figure 2.10); this result suggests most of the QDs were not fully cleaved but still linked to a larger structure. Because gelatin should be completely degraded by collagenase, the most likely explanation for the broad distribution is the presence of long glutaraldehyde cross-links that are still conjugated to the QDs. Several strategies to solve this issue that we attempted were:

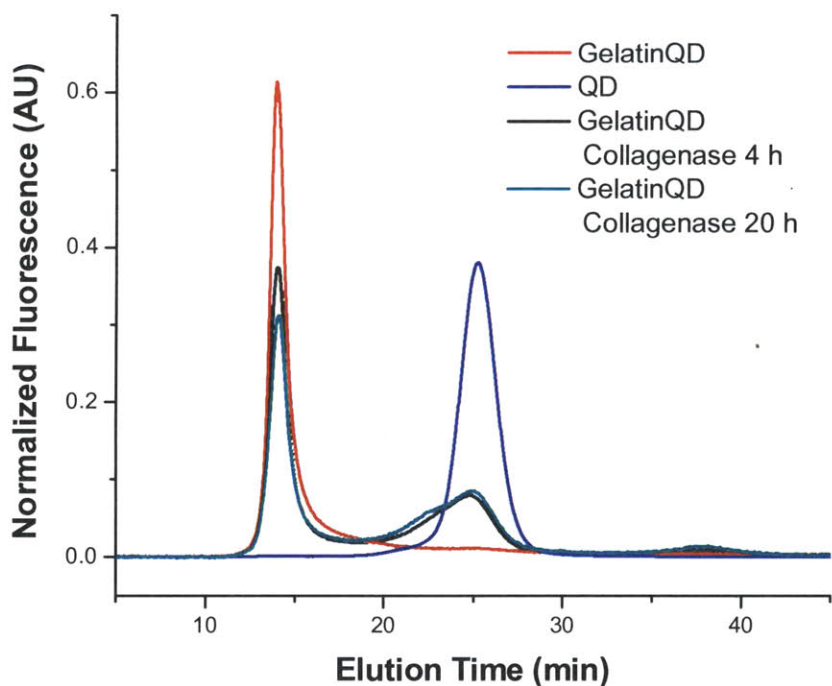


Figure 2.10. Incubation of Polyacrylic Acid-PEG QD Gelatin NPs (grade X glutaraldehyde) with collagenase for 4 hours (A) and 20 hours (B).

1. Conjugate QDs to gelatin NPs through a cleavable peptide as discussed in the previous section (2.3.5). However, we experienced problems with interparticle cross-linking and did not observe an improvement in the size of the QD after cleaving. More optimization may be necessary to saturate the surface of the QD with peptide.
2. Coating the surface of the gelatin NP with a layer of gelatin. The gelatin layer allows collagenase to cleave completely in between the gelatin NP and QDs, bypassing the glutaraldehyde. The problem we observed was that coating the gelatin nanoparticle with gelatin caused the size to increase substantially.
3. Another strategy was to cross-link the gelatin nanoparticle with many short cross-links instead of a few large glutaraldehyde cross-links. Thus when the collagenase cleaves the gelatin, the fragment(s) of gelatin still attached to the QD are too small to add to the size of

the QD. The challenge with this strategy is that using short cross-links tend to result in unstable gelatin NPs. A balance must be made such that the gelatin NPs is stable but yet falls apart completely after incubation with the protease.

Out of the three options above, the third one was shown to be effective in minimizing the size of the cleaved QDs to be the same as individual QDs. There are three major grades of glutaraldehyde (Figure 2.11, Table 2.2): grade I, grade II, and grade X (which does not have its grade specified). Grade I glutaraldehyde is predominantly monomers and produced small cleaved QDs but produced the broadest size distribution for the gelatin NP. Grade II and grade X appears nearly the same through absorption spectroscopy, but they exhibit different size distributions of cleaved QDs. The pH used in the desolvation step also has an influence on the size of the gelatin NP after cleaving. A pH of 3.0 yielded cleaved QDs with a small size, whereas a pH of 3.3 yielded cleaved QDs that were mostly still aggregated (Figure 2.13). Initially we used grade II or a 50:50 mixture of grade I:grade II for cross-linking the gelatin nanoparticle at pH 3.0 which produced the largest percentage of small cleaved QDs (Figure 2.12). However, when we used MMP-2 to cleave the Gelatin-QD nanoparticles, the cleaving rate was extremely slow such that it was nearly negligible after 12 hours. Since the amount of MMP-2 used is much smaller than collagenase due to its substantially higher cost, the sample needed to be much more sensitive in order to be cleaved by the commercial MMP-2. We were able to achieve highly sensitive gelatin NPs by using grade I glutaraldehyde for cross-linking the gelatin nanoparticle. Grade I glutaraldehyde needed longer reaction times and double the amount previously applied to achieve gelatin particle stability. More thorough characterization of this construct's size-changing properties *in vitro* and *in vivo* will be discussed in the next chapter.

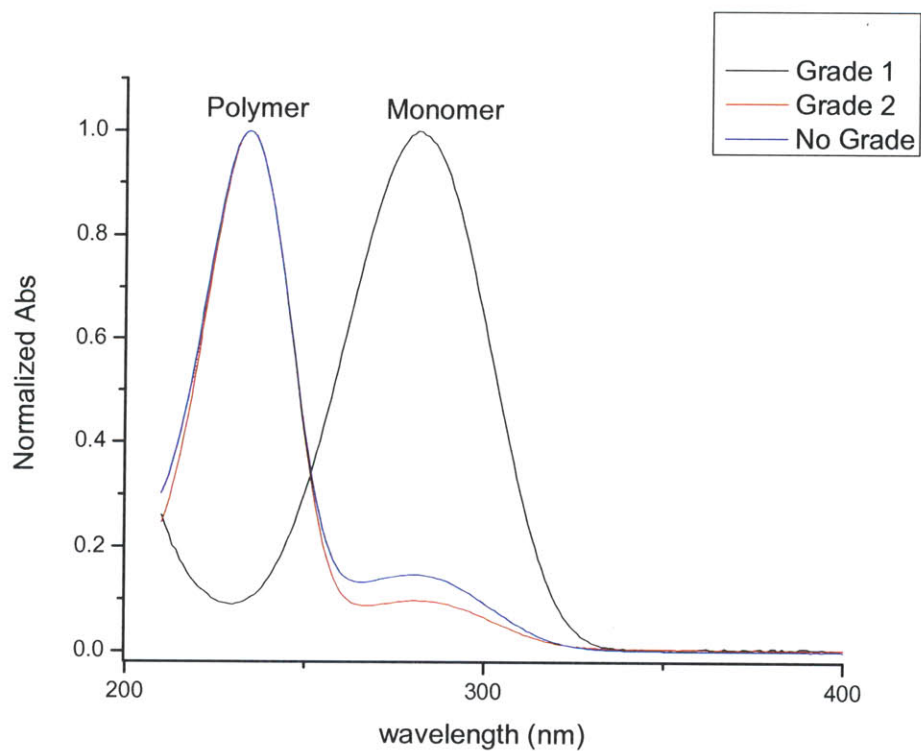


Figure 2.11. UV absorption spectra of different grades of glutaraldehyde.

Grade	Abs 235 nm	Abs 280 nm	A235/A280
G1	0.105	0.994	0.105634
G2	0.997	0.097	10.27835
GX	0.997	0.147	6.782313

Table 2.2. Comparison of absorbance at 235 nm (polymer) and 280 nm (monomer) for different grades of glutaraldehyde

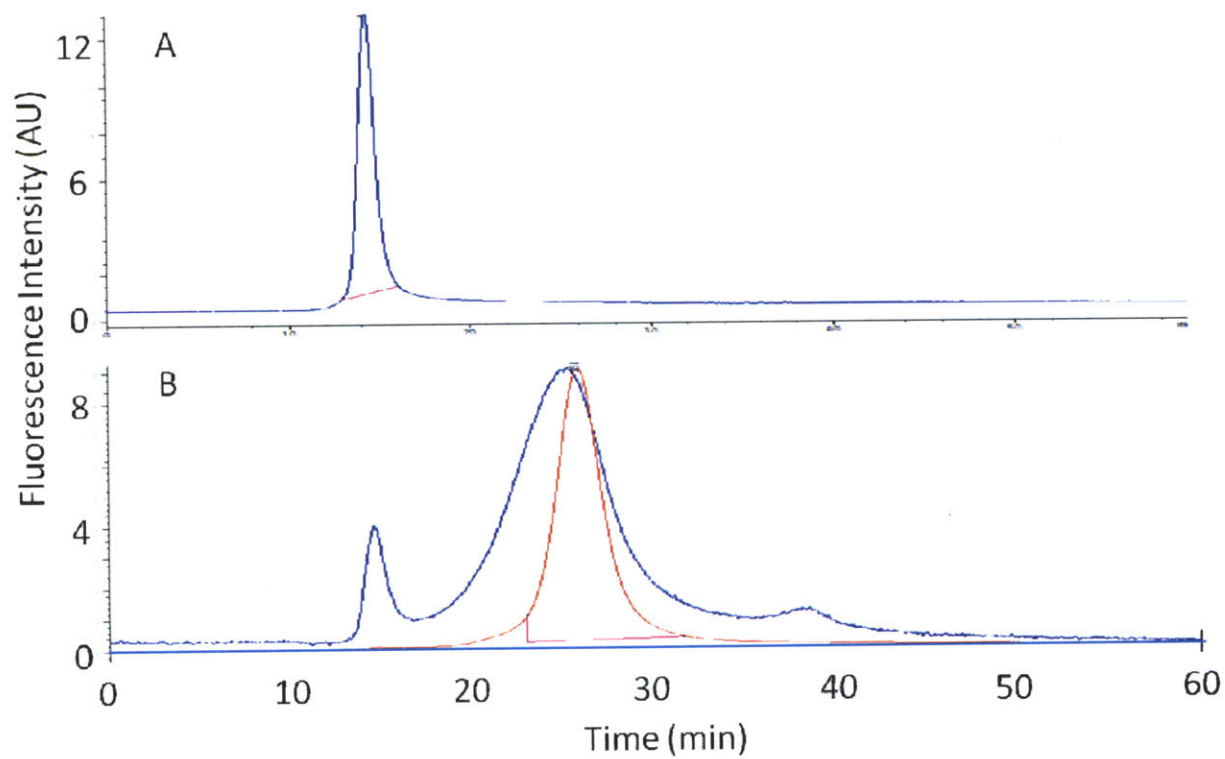


Figure 2.12. GFC chromatogram of Polyacrylic Acid-PEG QD Gelatin NPs (1:1 ratio of G1:G2 glutaraldehyde) with collagenase. (a) Gelatin QD before collagenase. (b) Gelatin QD after cleaving with collagenase (blue) and QD (red) is given as reference.

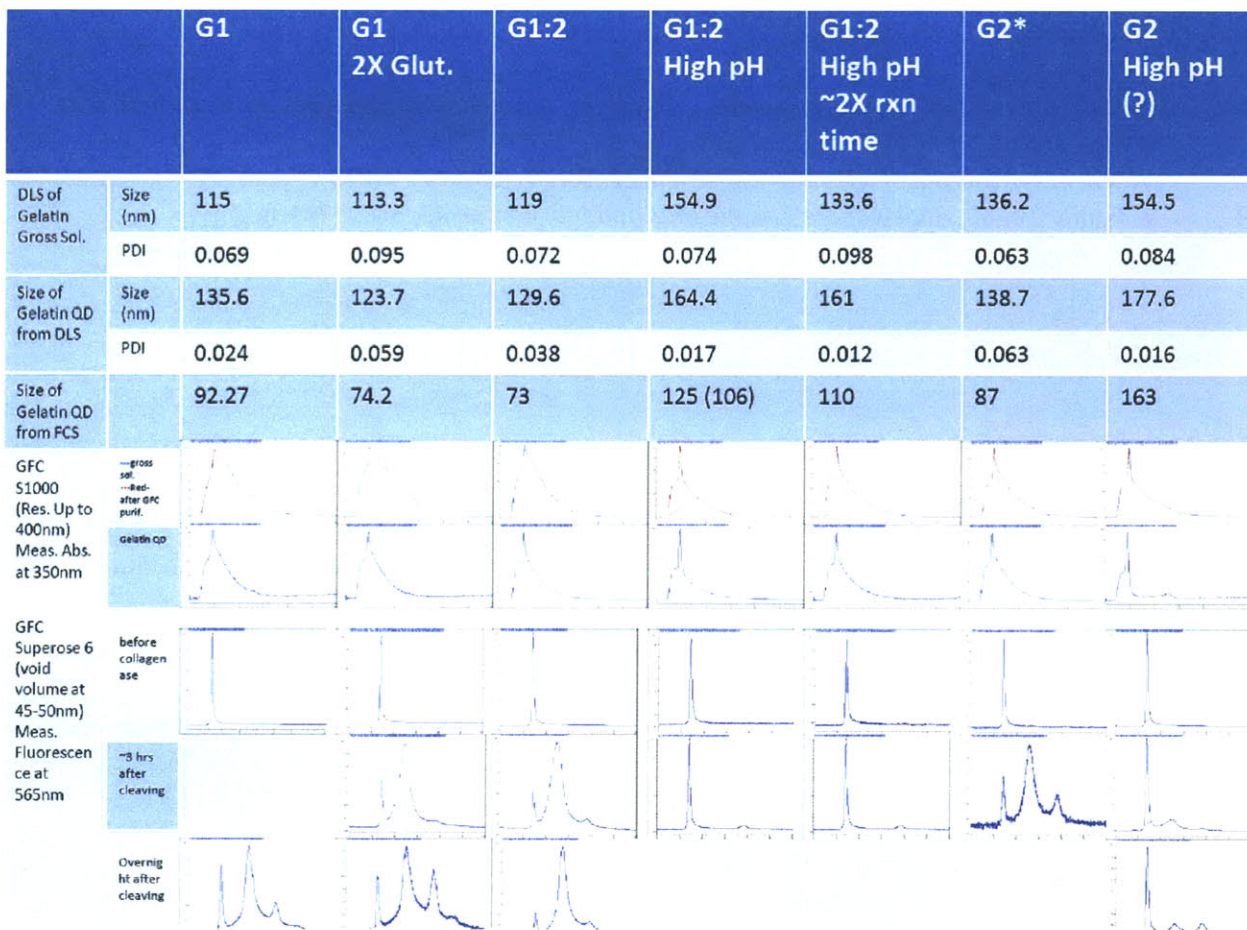


Figure 2.13. Comparison of size and size-changing properties of Polyacrylic Acid-PEG QD Gelatin NPs synthesized with different grades of glutaraldehyde, pH, and reaction time. The pH used during synthesis for all samples was at 3.0 except for those specified as ‘high pH’ in which pH 3.3 was used. The reaction time used during synthesis for all samples was at 4 hours except for those specified as ‘~2x rxn time’ in which the reaction time was 7.5 hours.

3.4 References

1. C. J. Coester, K. Langer, H. Von Briesen, J. Kreuter, *Journal of Microencapsulation: Micro and Nano Carriers* **17**, 187 (2000).
2. W. Liu *et al.*, *Journal of the American Chemical Society* **132**, 472 (2010).
3. Z. Popović *et al.*, *Angewandte Chemie International Edition* **49**, 8649 (2010).

Chapter 3

***In Vitro* and *In Vivo* Characterization of Size-Changing Nanoparticle**

3.1 Introduction

Exploration of different size-changing NP constructs in the last chapter revealed that the most effective structure consisted of a gelatin NP core cross-linked with grade I glutaraldehyde and conjugated on the surface with polyacrylic acid-PEG QDs. This construct bested the others in terms of the size of the cleaved QDs, the kinetics of cleaving, the NPs' fluorescence intensity, and the structure's overall simplicity. In this chapter, we present further characterization of the *in vitro* and *in vivo* size-changing properties of this construct, which will be referred to as quantum dot gelatin NP or QDGelNP.

3.2 Materials and Methods

Note: The experiments were performed in collaboration with Dr. Triantafyllos Stylianopoulos, Jian Cui, and John Martin.

3.2.1 Materials

Hydrochloric acid fuming 37% TraceSelect, Nitric Acid >69.0% TraceSelect, and

Ethylenediaminetetraacetic Acid, Disodium Salt Dihydrate (EDTA) were purchased from Sigma-Aldrich.

HEPES, and 10x PBS Liquid Concentrate were purchased from EMD Chemicals Inc. (Gibbstown, NJ).

Calcium chloride, and glycine were obtained from Mallinckrodt Baker Inc. (Phillipsburg, NJ). ICP-OES cadmium standard 2% HNO₃ 1,000 mg/L was purchased from Perkin Elmer (Shelton, CT). GIBCO® Certified Heat-Inactivated Fetal Bovine Serum was obtained from Invitrogen (Eugene, Oregon). Block™ Casein in PBS was purchased from Thermo Scientific (Rockford, IL). Reagent grade deionized water used for ICP-OES experiments was purchased from Ricca Chemical Company (Arlington, Texas). Water for all other experiments was obtained using a Barnstead NANOpure® Diamond Life Science UV/UF TOC water system (Thermo Fisher Scientific, Suwanee, GA). Active Human Recombinant MMP-2 was purchased from EMD Chemicals Inc. (Gibbstown, NJ).

3.2.2. Gel Filtration Chromatography (GFC)

GFC was performed on the QDGelNPs before and after incubation with MMP-2 for various lengths of time. Four samples of 0.1 mg QDGelNP in 50 mM HEPES, 2 mM CaCl₂ were incubated with 230 ng of MMP-2 for 0.25, 2.25, 5, or 12 hours at 37°C. At the end of the incubation time, EDTA solution was added to give a final concentration of 20 mM EDTA to inhibit further MMP-2 degradation. The samples before and after cleaving with MMP-2 were directly analyzed by GFC with a Superose™ 6 GL 10/300 column (GE Healthcare, Piscataway, NJ) on an Agilent 1100 series HPLC with an in-line degasser, autosampler, diode array detector, and fluorescence detector (Roseville, CA). The injection volume was 45 µL and the mobile phase was 1x PBS (pH 7.4) at a flow rate of 0.5 mL/min. The GFC chromatograms were detected by fluorescence detection at 250 nm excitation wavelength and 565 nm emission wavelength, allowing us to measure only the elution profile of the QDs. Due to changes in the QD fluorescence intensity over time and scattering effects, the chromatograms' integrated intensities from 13 to 38 min were normalized to unity. We then analyzed the percentage of QDs that were released over time. The peak corresponding to the free QDs was integrated (from 18-38 min) and then corrected for peak tailing from the peak at void volume. A simple peak tailing correction was done by assuming that for a certain integrated area of the peak at void volume, a fixed percentage of that integrated area will be

added to the peak for free QDs. This fixed percentage (26.5%) was obtained using QDGelNP before cleaving, which should elute completely at the void volume if not for peak tailing.

3.2.3 Fluorescence Correlation Spectroscopy (FCS)

FCS measurements were carried out on a custom-built inverted confocal microscopy setup equipped with a Nikon Plan Apo VC (60x, 1.2 N.A.) water immersion objective. The 514 nm laser line from an argon-krypton-ion laser (Innova 70C, Coherent Inc., Santa Clara, CA) at 6.2 μW (measured at the back aperture of the objective) was used for excitation. The emission was collected through the same objective and spatially filtered by focusing through a 25 μm pinhole. Following a 550 nm long-pass filter, the fluorescence was split using a 50-50 beamsplitter and recorded using avalanche photodiodes (SPCM-AQR-13, Perkin Elmer, Shelton, CT). Cross-correlation was performed using a digital correlator (ALV7004-FAST, ALV, Langen, Germany) and correlogram fitting was performed from lag time (τ) 7.0 $\times 10^{-4}$ ms to 2.35 $\times 10^4$ ms using the ALV software. Sample carriers were formed by sealing a silicone perfusion chamber (PC8R-2.5, Grace Bio-Labs Inc., Bend, OR) over a 22 \times 50 mm glass coverslip (VWR, Pittsburgh, PA). The cover slip surface was pretreated with casein/PBS solution to prevent non-specific binding. HEPES (50 mM, pH 7.5) was used as the solvent. The QDGelNP suspension was diluted to ~ 0.2 mg/mL. The temperature during the measurement was $\sim 296^\circ\text{K}$. Five to ten measurements with acquisition times of 60 seconds each were performed for each sample.

FCS Analysis. In our confocal setup, the axial dimension of the focal volume is significantly larger than the lateral dimensions. Hence, it is sufficient to fit the cross-correlation function using the isotropic 2D translational diffusion model,

$$g(\tau) = \frac{1}{N_p} \frac{1}{(1+\tau/\tau_D)} \quad (4.1)$$

This allows us to obtain the correlation time for each measurement. Then we calculate the diffusion coefficient using the equation:

$$D = \frac{\omega^2}{4\tau_D} \quad (4.2)$$

The radius of the confocal detection volume (ω) was obtained using 0.10 μm calibration standards (R100, Thermo Scientific) and the QDs. Diffusion coefficients from repeated measurements were averaged. Hydrodynamic radius was obtained from the mean diffusion coefficient using the Einstein-Stokes equation:

$$D = \frac{k_B T}{6\pi\eta r} \quad (4.3)$$

The value used for viscosity (η) of water at 295.6°K was 9.4×10^{-4} Pa·s.

3.2.4 ICP-OES

The concentration of QD in a QDGelNP sample was determined by measuring its Cd content and then comparing it to the Cd content in a QD sample of known concentration. The QDGelNP and QD standard solutions were first completely dissolved in aqua regia ($\text{HCl}:\text{HNO}_3 = 3:1$) solution, and then its Cd content was determined using a Horiba Jobin Yvon Activa ICP-OES instrument. QDGelNP in solution (300 μL) was heated to 130°C in a glass vial until the water has completely evaporated. Fresh aqua regia solution (250 μL) was added to the dried QDGelNP sample. The solution was covered with parafilm and sonicated for 5 minutes. Afterwards the solution was heated overnight at 65°C. DI water (1.75 mL) was added the next day using VWR® Labmax™ Bottle-Top Dispenser. Samples made from cadmium ion calibration standards and known amount of QDs were prepared by the same method. These solutions were prepared so that their Cd concentration would fall above and below the QDGelNP sample's Cd concentration. The calibration was linear with an error of less than 2%. The ICP-OES intensity was the average of five (30sec) exposures. A calibration curve for the amount of QD was created using the QD standard solutions to give a value for the mole of Cd per mole of QD. This value was used to determine the amount of QD in the QDGelNP solution.

3.2.5 X-ray Photoelectron Spectroscopy (XPS)

QDGeINPs with and without PEGylation were transferred to DI water by centrifugation at 10,000 rpm for 10 min and washed with DI water three times. The particles were then drop-casted on a p-type silicon substrate (University Wafer, South Boston, MA) and dried overnight in vacuum. The samples were characterized using a Kratos AXIS Ultra Imaging X-ray Photoelectron Spectrometer (Kratos Analytical, Chestnut Ridge, NY) with a monochromatized Al K α X-ray source. High resolution analysis of the C1s spectra was performed to determine the chemical composition from the hydrocarbon (C-C or C-H at 285.0 mV), ether (C-O at 286.4 mV), carbonyl (C=O at 288.2 mV), and carboxyl (C=O at 289.1 mV) envelopes. Deconvolution of the spectra determined the area under the peak for each chemical species and thus their relative composition.

3.2.6. *In Situ* Zymography

The procedure developed in (1) was used. Cryostat section of an HT-1080 tumor was air-dried for 10 min. DAPI was added to a 1% (w/v) low gelling temperature agarose in PBS to give a final concentration of 1.0 μ g/mL. This solution was then combined with a 1.0 mg/mL solution of DQTM gelatin (Invitrogen, Eugene, OR) in a 10:1 ratio. The combined mixture (40 μ l) was put on top of the tumor section and enclosed with a coverslip. After gelation of the agarose at 4°C, the gel and the tumor section was incubated for 2 hours at room temperature. The cell nuclei stained with DAPI and unquenched FITC from MMP digestion of DQTM gelatin were imaged on a confocal microscope. Fluorescence of FITC was detected with excitation at 460–500 nm and emission at 512–542 nm. DAPI was detected with excitation at 340–380 nm and emission at 425 nm.

3.2.7 Collagen Gel Diffusion

Collagen hydrogels were prepared by mixing the following components in order on ice: 141.75 μL of 8.6 mg/ml rat tail collagen I (354249, BD Biosciences), 3.8 μL of 1 N sodium hydroxide, and 19.5 μL of 0.17 M EDTA. The final concentration of collagen was 7.38 mg/ml and EDTA was 20 mM. After vortexing, the gel was added to partially fill a microslide capillary tube (Vitrocom Inc. No. 2540, Mt. Lakes, NJ), then incubated overnight at 37°C. QDGelNPs (0.1 mg) were incubated with 230 ng of activated MMP-2 for 12 hours in 50 mM HEPES 2 mM CaCl_2 . At the end of 12 hours, EDTA was added to give a final concentration of 20 mM. A 20 μL mixture of the QDGelNPs either before or after incubation with MMP-2 and SilicaQDs was added into the capillary tube and placed in contact with the surface of the collagen gel. The concentration of the two particles and sensitivity of the avalanche photodiodes (APD) were adjusted so that both particles gave similar signal intensities. The sample was left in ~ 295 K for 12 hours and then imaged using a multiphoton laser scanning microscope. Image analysis was performed using ImageJ. The concentration profile for the QDGelNPs after cleaving was fitted to the following one-dimensional model to obtain the diffusion coefficient in the collagen gel (2):

$$C(x, t) \propto \text{erfc}\left(\frac{x}{2\sqrt{D_{eff}t}}\right) \quad (4.4)$$

where erfc is the complementary error function. The nonlinear curve fitting was performed using fminsearch in Matlab®. The diffusion coefficient ratio (D/D_o) was compared to reported values in (3) and (4). In (4), D/D_o was found to be ~ 0.35 for an 11.2 nm QD in 9.37 mg/mL collagen gel. In (3), a value of ~ 0.95 for D/D_o was obtained for a ~ 10 nm particle in 2.4 mg/mL collagen gel. Values for D/D_o obtained for higher concentrations of collagen gel from (3) were not used because these concentrations were prepared by centrifuging low-concentration gels and these results did not match gels prepared directly from high-concentration solutions. By simple linear interpolation of these two values, we obtained a D/D_o for ~ 10 nm NP in 7.38 mg/mL collagen of 0.52.

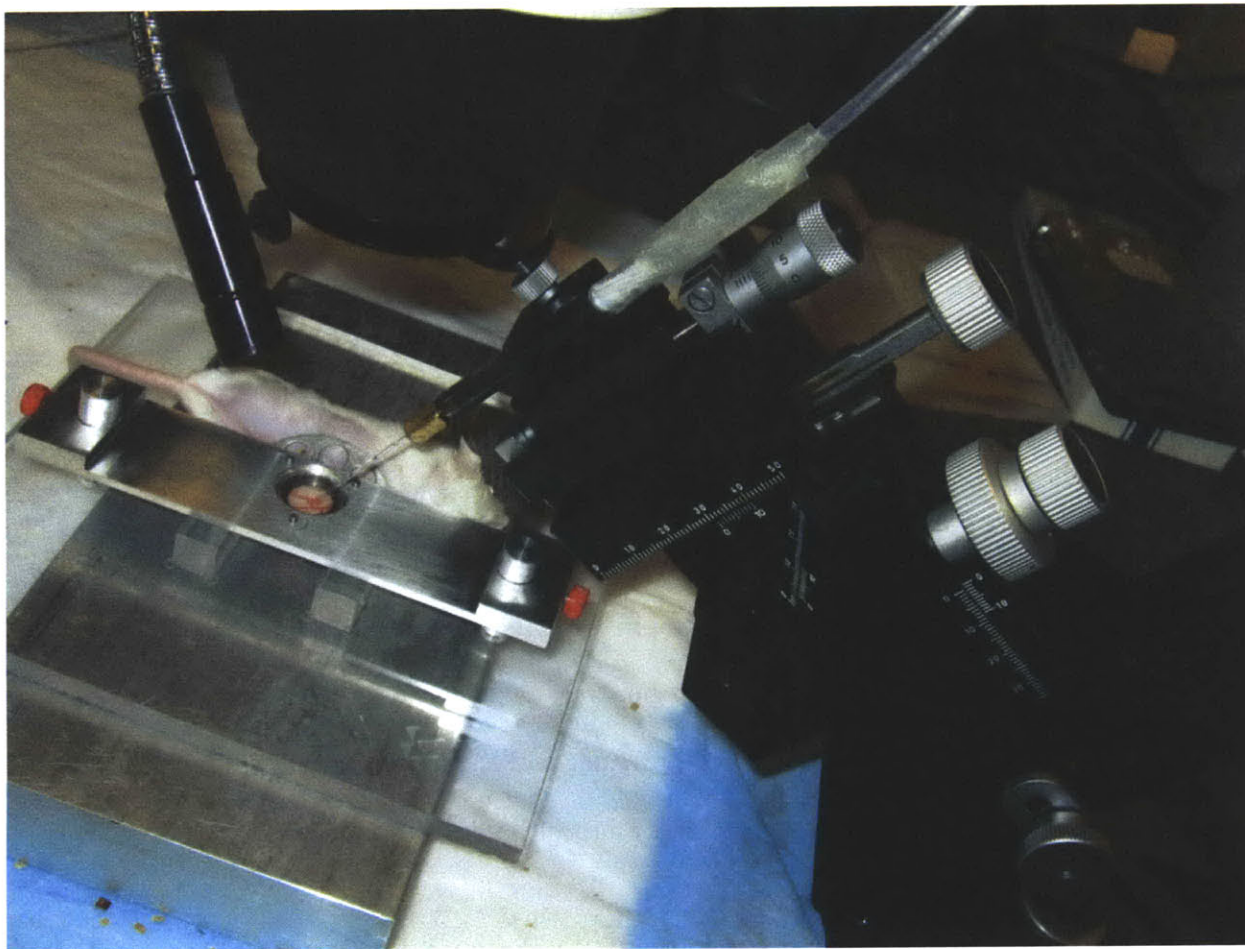


Figure 3.1. Experimental setup for intratumoral injection

3.2.8 Intravital Multiphoton Microscopy

All animal procedures were done following the guidelines of the Public Health Service Policy on Humane Care of Laboratory Animals and approved by the Institutional Animal Care and Use Committee of the Massachusetts General Hospital. Human fibrosarcoma HT-1080 cells were implanted in the dorsal skin of severe combined immunodeficient (SCID) mice for *in vivo* imaging (5, 6). When tumors reached 5 mm in diameter, we injected a 1 μ L mixture of QDGelNPs and SilicaQDs ($\sim .05 \mu$ L/min) into the tumor at constant pressure using a glass micropipette connected to a syringe filled with silicone oil (Figure 3.1).

Images were obtained with a custom-built multiphoton microscope using a Ti:Sapphire laser (Mai-Tai Broadband; Spectra-Physics, Mountain View, CA) at 900 nm, a 20x(0.5NA; Olympus) water-immersion objective, and photon-counting photomultiplier tubes (H7421-40; Hamamatsu). Detection of QDGeINPs was performed via a 530DF100 emission filter and SilicaQDs via a 610DF75 emission filter. Collagen fibers were imaged with second-harmonic generation (2, 7, 8) via a 450DF100 emission filter. The laser power was set to 500 mW. Three dimensional image stacks containing 21 images of 5 μm thickness were obtained wherever fluorescence intensity from the injected particles was detected. A maximum intensity z-projection of each colored stack generated a 2D image. Images of consecutive adjacent regions in the x and y directions were combined into a montage, generating a single image of the entire injection site.

The intensity profiles along the dotted lines in Figure 3.14 were extracted using ImageJ and then normalized such that the backgrounds (a “dark” region from all three time-lapse images) had the same intensity. The background was subtracted and the resulting profiles was fitted (Figure 3.15) to the model for diffusing substance initially distributed uniformly through a sphere of radius a (9) to obtain the diffusion coefficient:

$$C(r, t) = \frac{1}{2} C_o \left\{ \operatorname{erf} \frac{a-r}{2\sqrt{Dt}} + \operatorname{erf} \frac{a+r}{2\sqrt{Dt}} \right\} - \frac{C_o}{r} \sqrt{\frac{Dt}{\pi}} \left[\exp \left\{ -\frac{(a-r)^2}{4Dt} \right\} - \exp \left\{ -\frac{(a+r)^2}{4Dt} \right\} \right] \quad (4.5)$$

where C_o is the initial concentration in the sphere. It should be noted that the diffusion coefficient obtained in collagen gel was obtained at ~ 295 K while the *in vivo* experiment was measured at the slightly higher body temperature of ~ 310 K.

3.2.9 Blood half-life

The procedure in (10) was used. Nanoparticle circulation times were measured in non-tumor bearing female SCID mice. Each mouse was anesthetized with a ketamine/xylazene solution before intravenous infusion of nanoparticles by retro-orbital injection. For each time point, starting 1 min before the injection of particles, we collected 13 μL of blood via tail-vein nick and mixed this sample with 3 μL 50 mM EDTA in a plastic 96-well plate. To measure particle concentrations in the blood over time, we imaged in these samples using multiphoton microscopy to measure average intensities. To quantify the

clearance half-life, we fit a biexponential curve, taking into account tissue absorption and plasma clearance, to the data from each mouse.

3.3 Results

The multistage quantum dot gelatin nanoparticles (QDGelNPs) are composed of a gelatin core with amino-PEG QDs conjugated to the surface using EDC/sulfo-NHS coupling chemistry. Another layer of 5 kDa PEG is conjugated to the surface of the gelatin nanoparticles to confer long blood circulation time. X-ray photoelectron spectroscopy (XPS) was used to determine the presence of PEG chains on the QDGelNPs surface (Figure 3.4). Dynamic light scattering (DLS) of the QDGelNPs before and after PEGylation (but before purification) indicate an increase in diameter from 78.3 ± 0.2 nm to 93.7 ± 0.5 nm. DLS of the final structure after purification and size selection using GFC revealed a single particle distribution with a hydrodynamic diameter of 97.9 ± 2.1 nm and a polydispersity of 41.2% (Figure 3.3). This value agreed well with the average diameter of 99 ± 1 nm estimated from scanning electron microscopy (SEM) (Figure 3.2c and 3.2d). Inductively coupled plasma optical emission spectroscopy (ICP-OES) determined a concentration of 15 pmol of QDs per mg of QDGelNPs. The QDGelNPs showed excellent colloidal stability; their diameter by DLS remained nearly unchanged while in storage at $\sim 4^\circ\text{C}$ over 48 days – from 95.7 ± 4.1 nm on day 1 to 101.1 ± 2.5 nm on day 48 (Figure 3.2b, Table 3.2).

We designed both the initial 100-nm NPs and the released 10-nm NPs to have a neutral surface charge, ensuring the difference in transport before and after cleaving is only a result of size change. In addition, previous report suggested neutral particles are optimal for diffusion in the interstitial matrix (4). The ζ potential of the ~ 100 nm QDGelNPs at pH 7.5 was -6.29 ± 0.22 mV and at pH 6 was -5.00 ± 0.12 mV. The ζ potential of the ~ 10 nm QDs used for the second stage NP was -5.13 ± 0.16 mV at pH 7.5 and -4.36 ± 0.17 mV at pH 6 (Figure 3.3c and 3.3d, Table 3.1). These results confirm the charge neutrality of both particles in the pH range found in normal tissues and solid tumors.

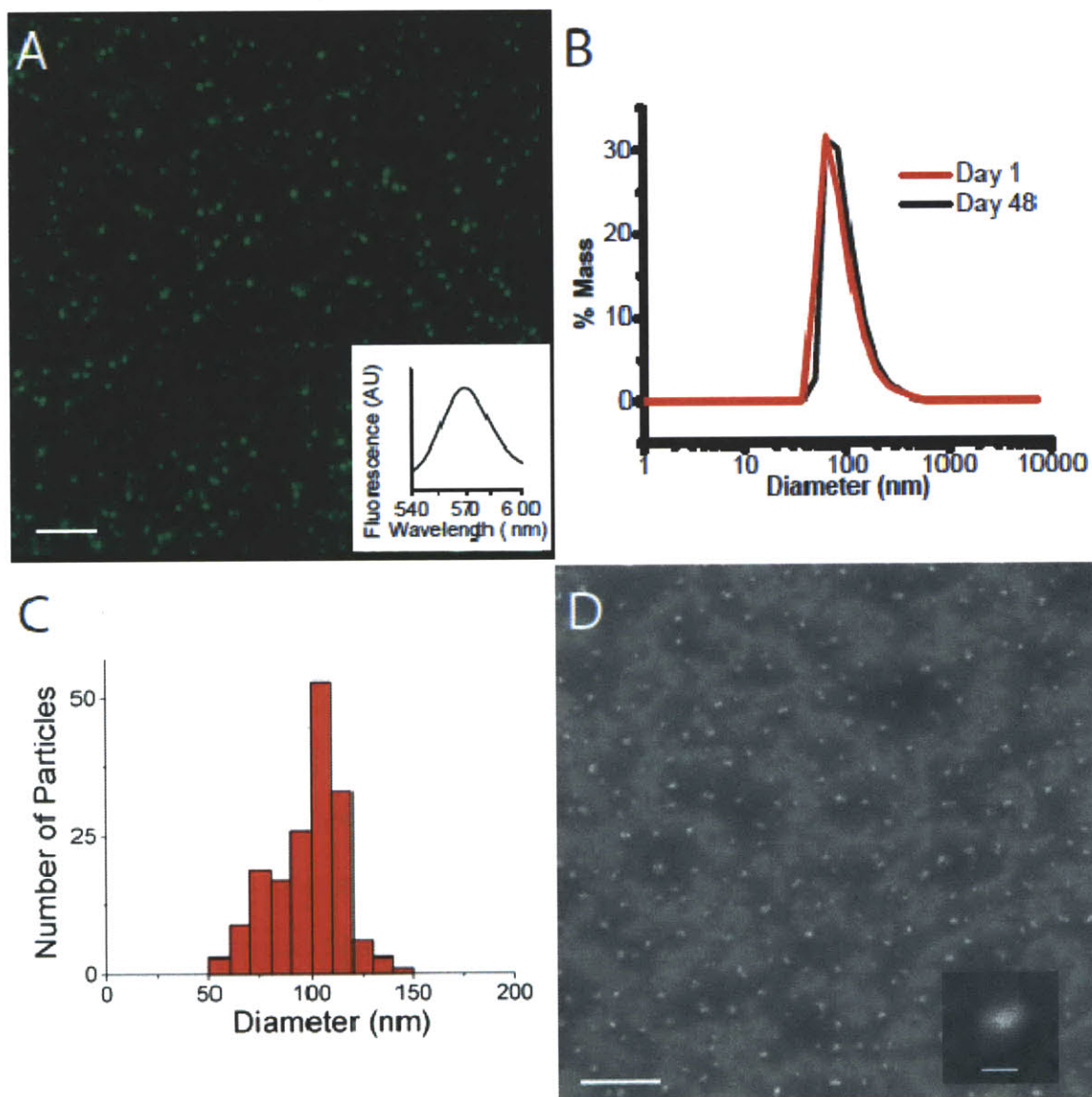


Figure 3.2. QDGelNP physical and *in vitro* characterization. (A) Epifluorescence image of QDGelNPs on a silicon substrate at 100x magnification. Scale bar 5 μm. (B) DLS distribution of QDGelNP on day 1 and day 48 after synthesis and storage at 4°C. (C) Histogram of QDGelNPs' size distribution from image analysis of SEM image. (D) SEM image of QDGelNPs at 15,000X magnification. Scale bar 1 μm. (Inset, bottom) SEM image of individual QDGelNP at 35,000X magnification. Scale bar 100 nm. (D)

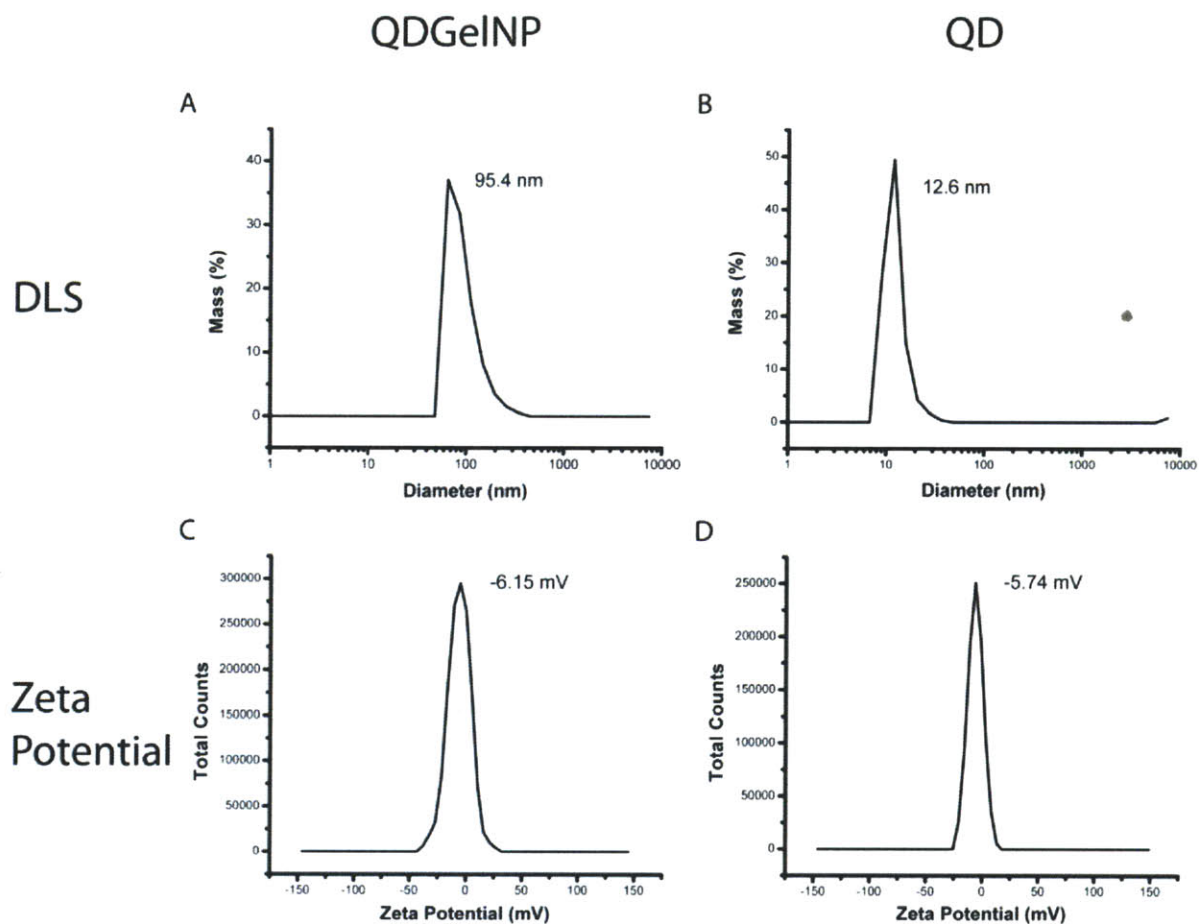


Figure 3.3. DLS size and zeta potential distributions of QDGeINPs and QDs. DLS mass percent particle size distributions of QDGeINPs (A) and QD (B). Zeta Potential distributions of QDGeINPs (C) and QDs (D).

	QDGeINP	QD
Diameter (M ± SEM, nm)	97.9 ± 2.1	12.5 ± 0.1
Percent Polydispersity	41.2%	31.0%
Zeta Potential at pH ~7.5 (M ± SEM, mV)	6.29 ± 0.22	5.13 ± 0.16
Zeta Potential at pH ~6.0 (M ± SEM, mV)	7.70 ± 0.16	4.36 ± 0.17

Table 3.1. Mean value and S.E.M. of five DLS size or zeta potential measurements for QDGeINPs and QDs

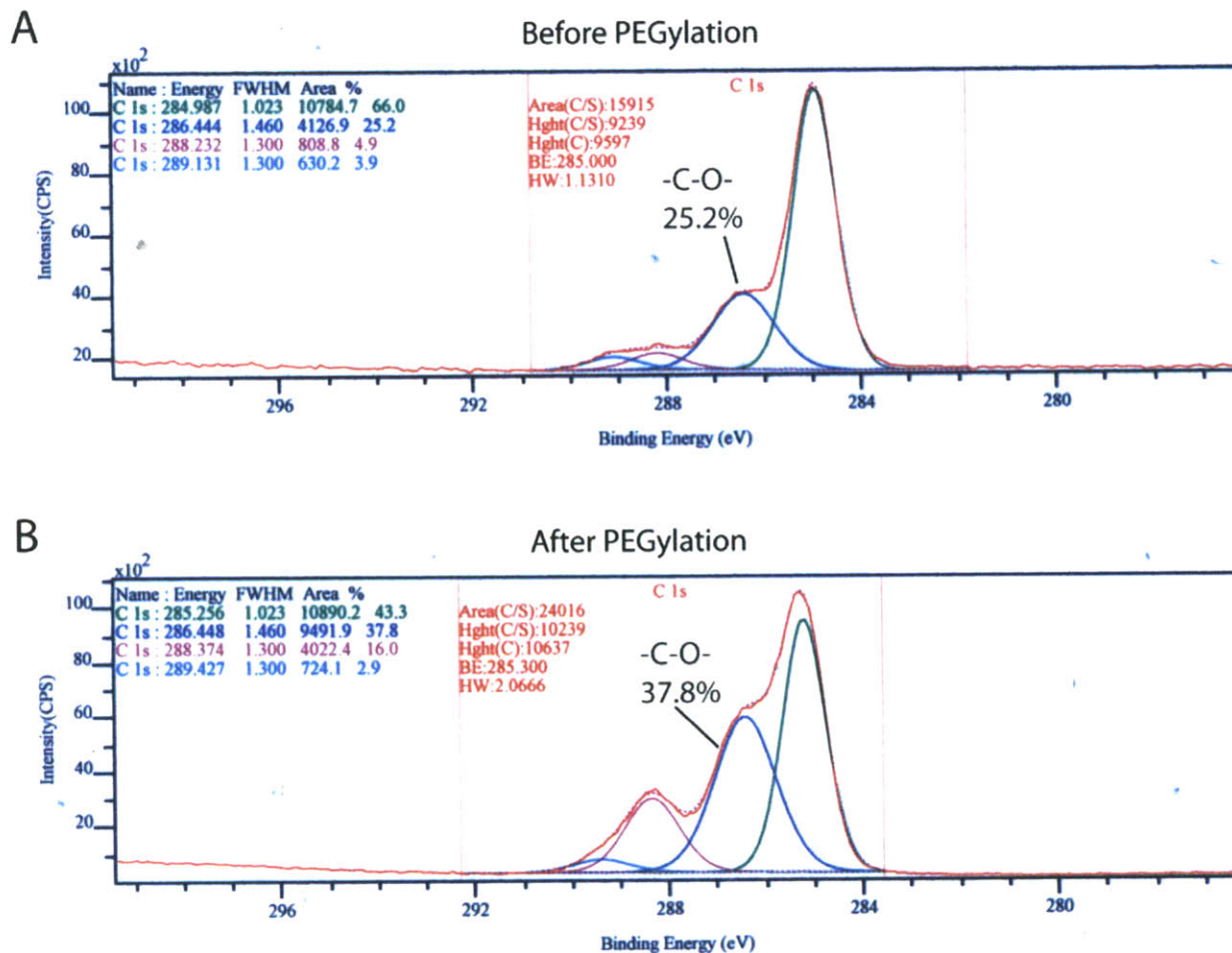


Figure. 3.4. High resolution XPS spectra of C1s region for QDGeINPs before PEGylation (A) and after PEGylated (B). Peak deconvolution of the spectra show the intensities for the C-H (hydrocarbon), C-O (ether), C=O (carbonyl), and C(=O)-O (carboxy) peaks at 285.0, 286.4, 288.2, and 289.1 eV binding energies, respectively. The greater percent area for the C-O peak after PEGylation (B) is attributed to the additional C-O bonds in the PEG surface coating.

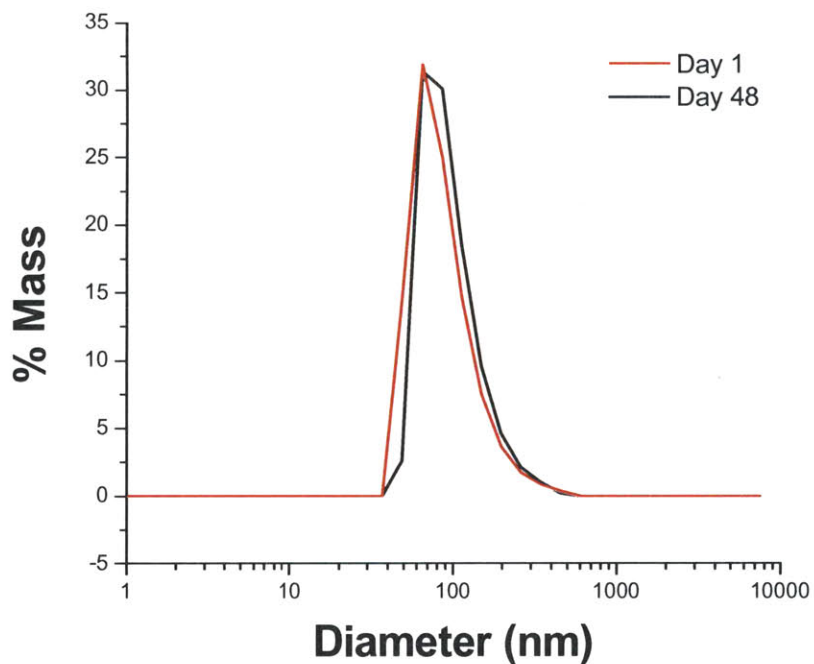


Figure 3.5. DLS distribution of QDGelNP on day 1 and day 48 after synthesis and storage at 4°C.

	Day 1	Day 48
Diameter (M ± SEM, nm)	95.7 ± 4.1	101.1 ± 2.5
Percent Polydispersity (M ± SEM, %)	53.4 ± 3.8	50.9 ± 2.4

Table 3.2. Mean value and S.E.M. of five DLS size measurements for QDGelNP on day 1 and day 48 after synthesis and storage at 4°C.

***In Vitro* Size Change**

We next investigated the ability of MMP-2 to change the size of QDGelNPs *in vitro* using GFC. GFC chromatograms using fluorescence detection (ex: 250 nm, em: 565 nm) were obtained from incubation of 0.1 mg of QDGelNPs with 230 ng (0.16 μM) of MMP-2 at 37°C (Figure 3.6b). A previous report has estimated the extracellular concentration of MMP-2 in HT-1080 (human fibrosarcoma) xenograft tumor tissue *in vivo* to be ~ 1 mM (11), significantly higher than the concentration used in our *in vitro* experiment. The QDGelNPs initially eluted at the GFC column's void volume but after incubation with MMP-2 for various times up to 12 hours, the peak shifted to a longer elution time corresponding to the smaller size of individual QDs, whereas incubation with 50% fetal bovine serum (FBS) showed no such shift (Figure 3.7). We assessed that 50% of the QDs were released in ~ 1.5 hours and the percent of freed QDs saturated at $\sim 90\%$ (Figure 3.8a), regardless of longer incubation times or addition of more MMP-2. We repeated this experiment with the incubation time kept constant at 12 hours but the amount of MMP-2 was varied (Figure 3.8b). Under this condition, only ~ 25 ng of MMP-2 was necessary to release 50% of the QDs. These results demonstrated the MMP-2 triggered size change occurred in an efficient and nearly complete manner.

We then verified that the released QDs diffuse optimally in the interstitial matrix, that residual gelatin/glutaraldehyde on their surface, imparted by cleavage of the gelatin NPs, do not lead to extraneous binding interactions or significant size increase. To investigate this possibility, we used FCS to directly measure the hydrodynamic diameter/diffusion coefficient of the QDs before and after cleaving the gelatin core (Figure 3.9, Table 3.3). The hydrodynamic diameter by FCS before cleaving was 81.1 ± 2.3 nm ($D = 5.6 \pm 0.2 \times 10^{-8} \text{ cm}^2 \text{ s}^{-1}$), which is consistent with the DLS measurement of 90.9 ± 1.3 nm for this batch. After MMP-2 digestion, the hydrodynamic diameter decreased to 9.7 ± 0.3 nm ($D = 4.7 \pm 0.2 \times 10^{-7} \text{ cm}^2 \text{ s}^{-1}$), which is the size of individual QDs, indicating the size increase of the released QDs from gelatin/glutaraldehyde fragments was negligible.

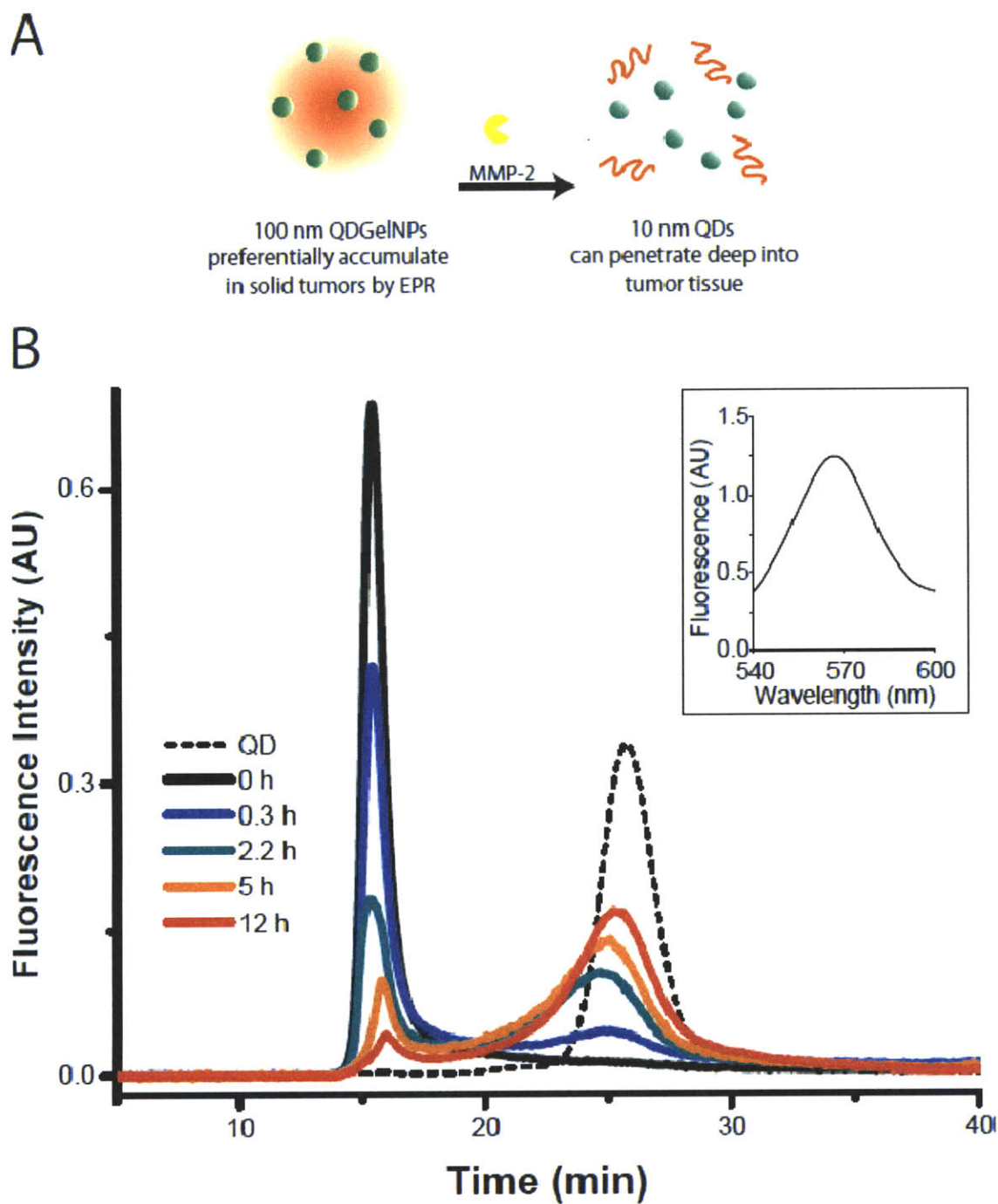


Figure 3.6. QDgelNPs change their size in response to MMP-2. (A) Schematic of 100 nm QDgelNPs changing size to 10 nm QD NPs by cleaving away the gelatin scaffold with MMP-2, a protease highly expressed in tumor tissue. (B) GFC chromatograms of QDgelNPs at various times after incubation with MMP-2. Fluorescence signal at 565 nm is collected. (Inset) Fluorescence spectrum of the peak at void volume for 2.2 hours cleaving time shows that the signal originates from QDs on the QDgelNPs.

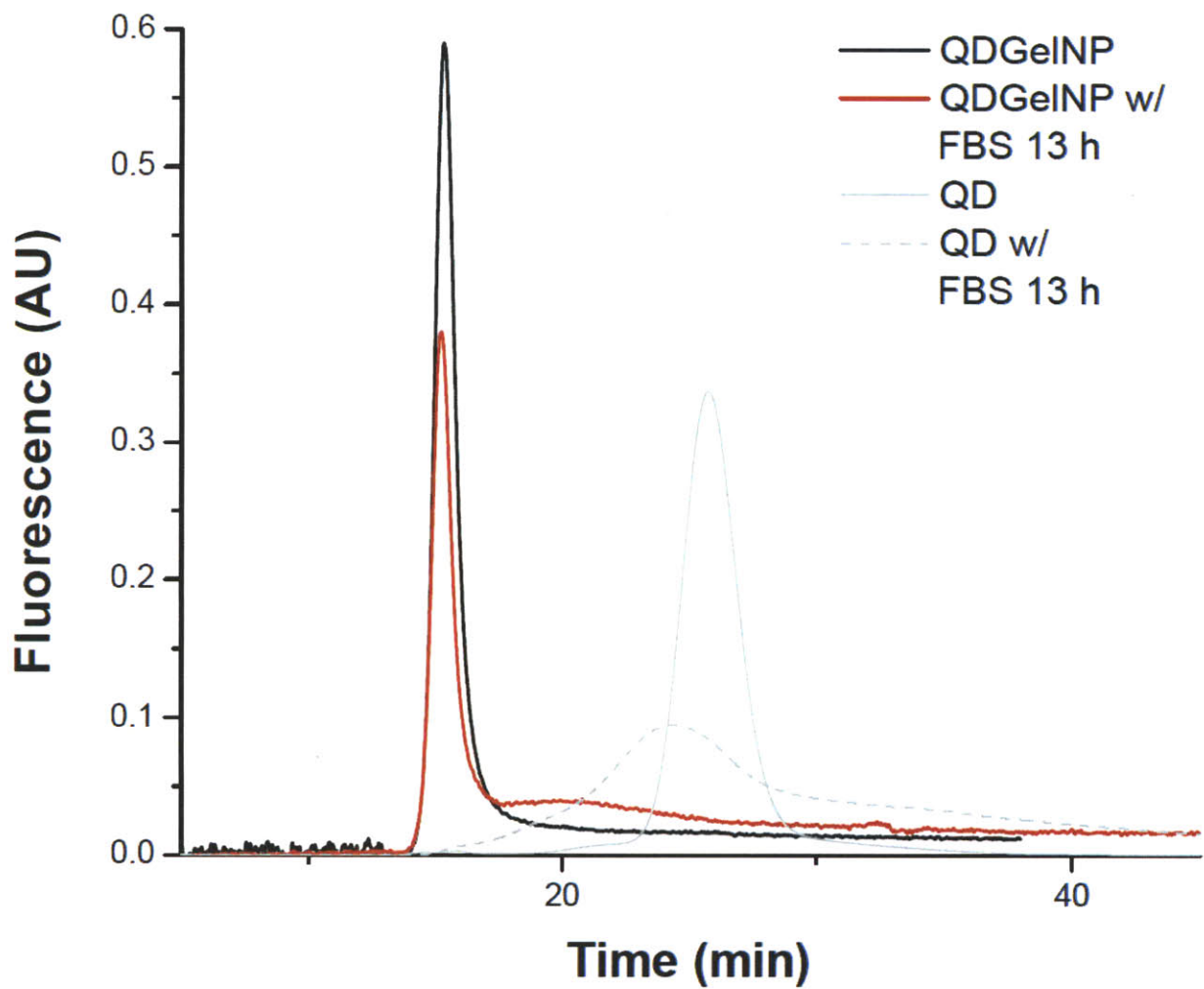


Figure 3.7. GFC chromatograms of QDGeINPs and QDGeINPs incubated with 50% FBS for 13 hours indicate no peak corresponding to release of individual QDs. Chromatograms of QDs and QDs incubated with 95% FBS are provided as reference.

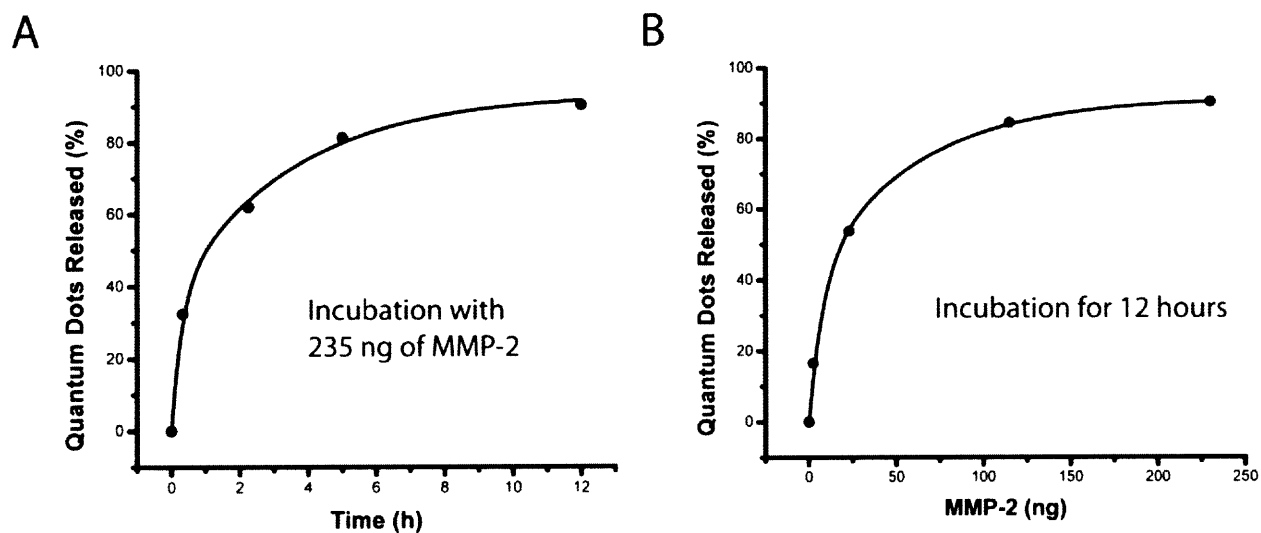


Figure 3.8. Kinetics of MMP-2 induced QD release from QDGelNPs (A) QD-release curve from incubation of 0.1 mg (0.16 μ M) of QDGelNPs with 230 ng of MMP-2 (B) QD release from incubation of 0.1 mg of QDGelNPs for 12 hours with varying amounts of MMP-2.

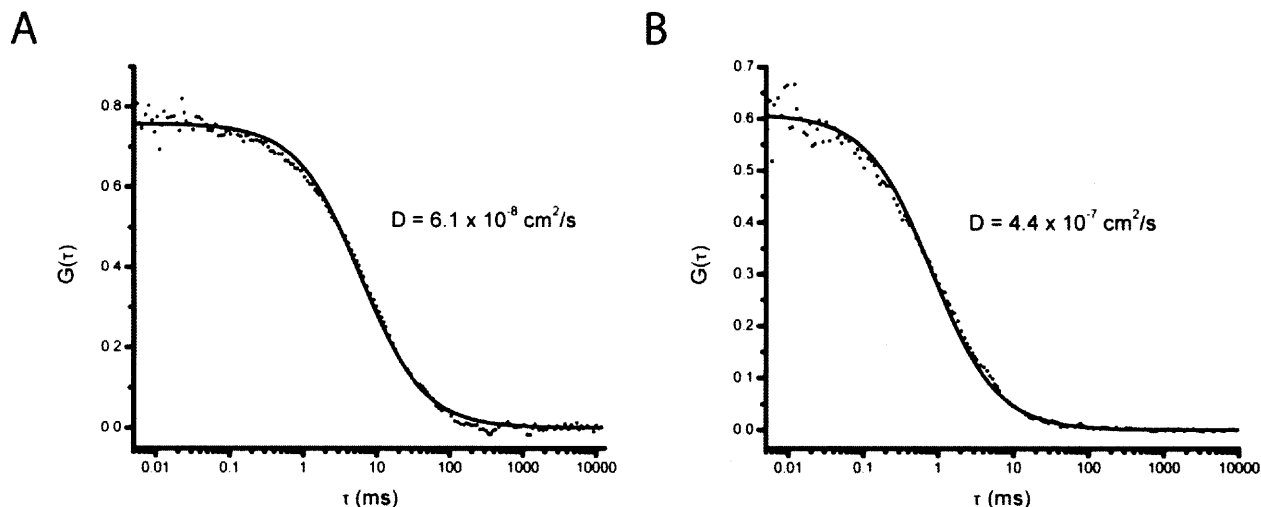


Figure 3.9. FCS cross-correlograms of QDGelNPs before (A) and after (B) incubation with MMP-2.

Summary of FCS Results

Diameter by FCS before MMP-2 (M \pm SEM, nm)	81.1 \pm 2.3
Diameter by FCS after MMP-2 (M \pm SEM, nm)	9.7 \pm 0.3
Diameter by DLS before MMP-2 (M \pm SEM, nm)	90.9 \pm 1.3
Percent Polydispersity by DLS	43.4%

Table 3.3. Mean value and S.E.M. of five FCS measurements for QDGelNPs before and after incubation with MMP-2. Hydrodynamic diameter obtained from DLS for QDGelNPs before incubation with MMP-2 is also provided.

We next evaluated whether the size change observed in GFC and FCS enhances diffusive transport in dense collagen environments resembling those in solid tumors. To simulate the interstitial matrix of a solid tumor, we prepared a collagen gel in a capillary tube at 0.74% (7.4 mg/mL) concentration, similar to the reported estimate of 9.0 ± 2.5 mg/(mL interstitial matrix) for interstitial collagen in both human colon adenocarcinoma (LS174T) and murine mammary carcinoma (MCalV) implanted in mouse dorsal chambers (3, 12). The collagen gel penetration of the QDGelNPs before and after cleaving with MMP-2 was compared to a non-cleavable, PEGylated, and QD-coated silica nanoparticles (10) control (Diam. = 105.6 ± 0.8 nm, ζ potential at pH 7.5 = -3.9 ± 0.2 mV) – designed to behave like QDGelNPs before cleaving. A mixture of SilicaQDs and QDGelNPs (before or after cleaving) were placed in contact with the gel and incubated for 12 hours. Infiltration of both particles into the collagen was determined using multiphoton microscopy with simultaneous second-harmonic generation (SHG) imaging of fibrillar collagen (Figure 3.10). The SilicaQDs and QDGelNPs before cleaving both had negligible penetration and were excluded from the collagen matrix (Figure 3.10a and 3.10b). However, after cleavage of QDGelNPs with MMP-2, the freed QDs were able to penetrate over a millimeter into the gel (Figure 3.10f and 3.10h). By fitting the concentration profile of the cleaved QDGelNPs to a one-dimensional diffusion model (2, 9), we obtained a diffusion coefficient of 2.3×10^{-7} cm² s⁻¹, the same diffusion coefficient obtained for individual QDs in the collagen gel before conjugation to the gelatin NP. The resulting diffusion coefficient ratio (D/D_o , where D_o is diffusion coefficient of freed QDs in solution obtained by FCS) in the collagen matrix is 0.49. This value agrees well with the expected value for D/D_o of ~ 0.52 derived from previous reports (see Methods for Collagen Gel) (3, 4). This result indicates that the diffusion coefficient of released QDs in dense collagen increases to that of ~ 10 nm particles and any residual gelatin/glutaraldehyde fragments remaining on the surface do not impede their diffusion.

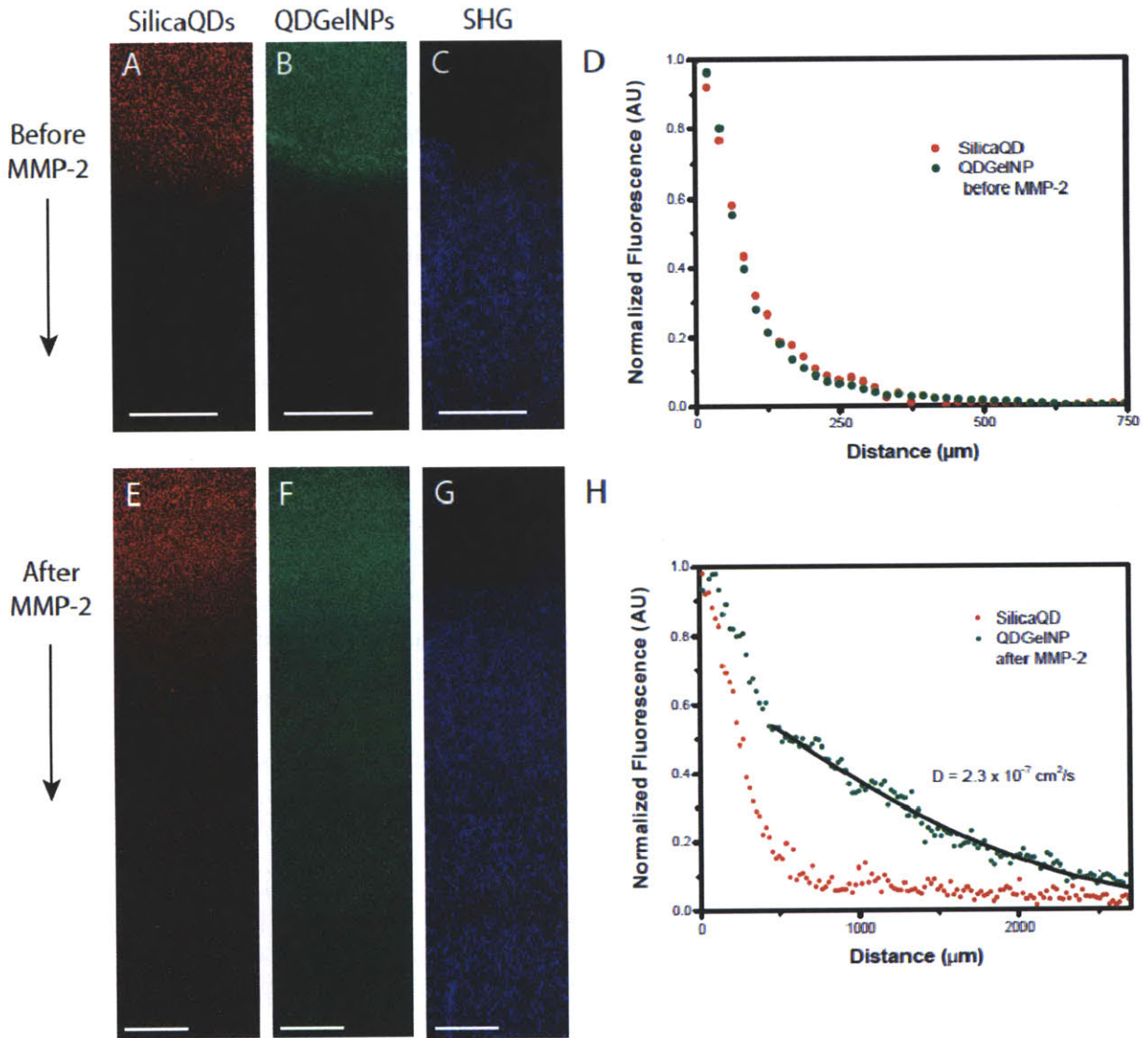


Figure 3.10. Diffusion of SilicaQDs and QDGeINPs (before and after MMP-2 cleavage) in a collagen gel. (A,B) Fluorescence images of SilicaQDs (A) and QDGeINPs before MMP-2 cleavage (B) penetrating into the collagen gel. (C) Second-harmonic generation (SHG) signal shows the corresponding location of the collagen matrix. Scale bars, 125 μm . (D) Normalized intensity profile of SilicaQDs and QDGeINPs in collagen gel. (E, F) Fluorescence images of SilicaQDs (E) and QDGeINPs after MMP-2 cleavage (F) penetrating into the collagen gel. (G) SHG signal shows the corresponding location of the collagen matrix. Scale bars 125 μm . (H) Normalized intensity profile of SilicaQDs and QDGeINPs after MMP-2 cleavage in collagen gel. Black line displays theoretical intensity profile for particles with diffusion coefficient of $2.3 \times 10^{-7} \text{ cm}^2 \text{ s}^{-1}$.

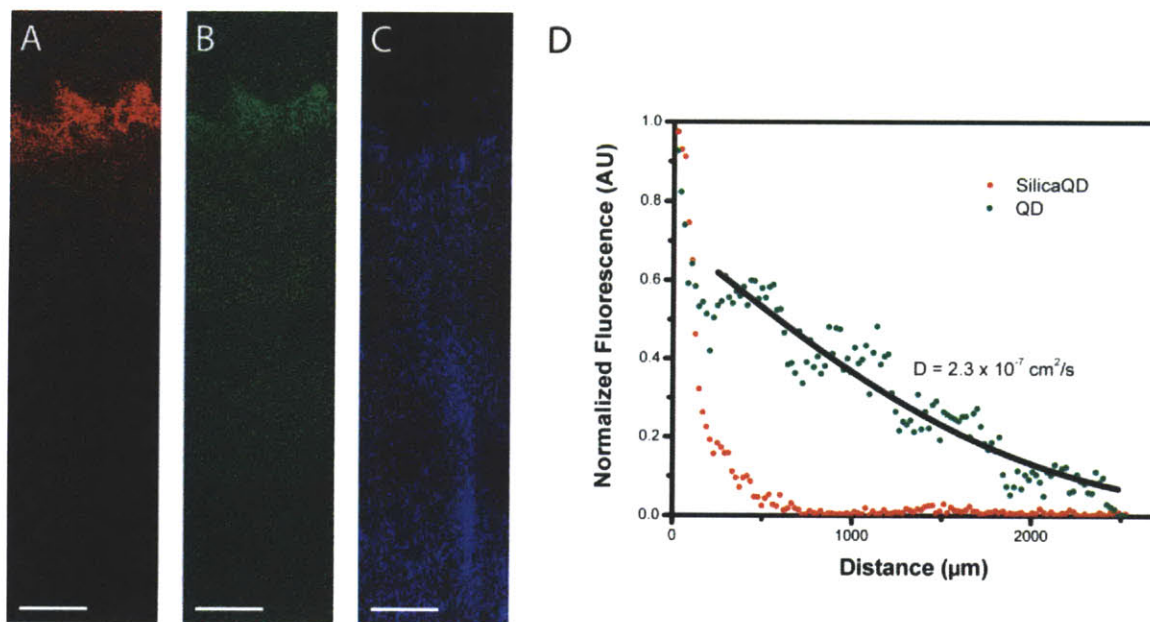


Figure 3.11. Diffusion of SilicaQDs and QDs in a collagen gel. (A,B) Fluorescence images of SilicaQDs (A) and QDs (B) penetrating into the collagen gel. (C) Second-harmonic generation (SHG) signal shows the corresponding location of the collagen matrix. Scale bars, 125 μm . (D) Normalized intensity profile of SilicaQDs and QDs in collagen gel.

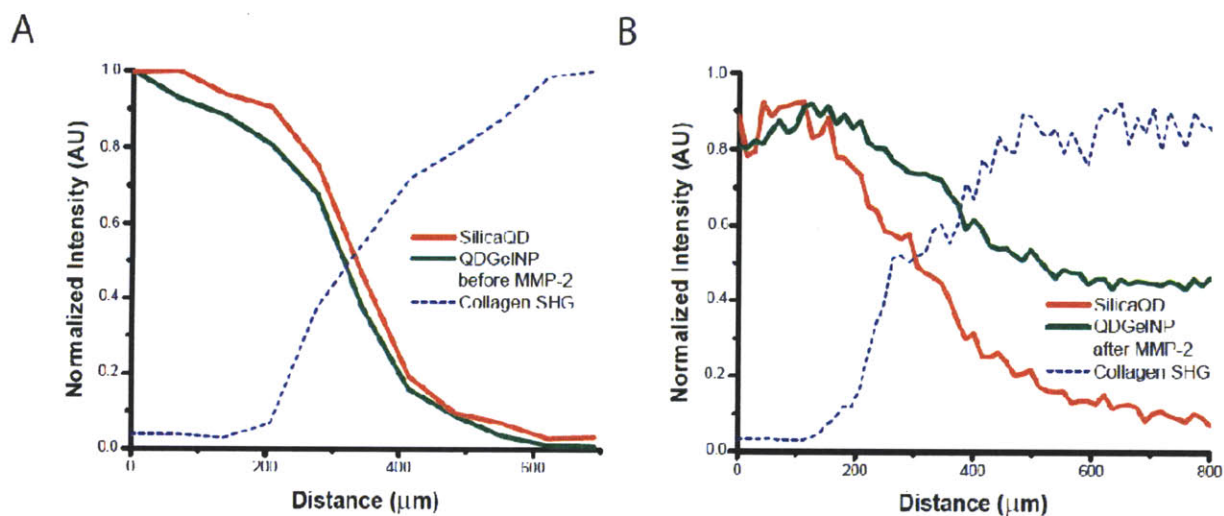


Figure 3.12. Particle distribution and second-harmonic generation (SHG) from collagen fibrils at collagen-solution interface in collagen gel experiment (Figure 3.10). (A) The intensity profile of SilicaQDs and QDGelNPs before cleavage in comparison with SHG indicates the exclusion of both sets of particles from the collagen matrix. (B) Intensity profile of SilicaQDs and QDGelNPs after cleavage in comparison with SHG shows penetration of QDGelNPs into the collagen but exclusion of SilicaQDs.

***In Vivo* Characterizations**

To test whether tumor secreted MMP-2 can change the size of QDGelNPs *in vivo*, we intratumorally co-injected QDGelNPs and SilicaQDs in the HT-1080 tumor implanted in the dorsal skin-fold window chamber of SCID mice. The HT-1080 tumor model was selected because of its reported high MMP-2 activity, which we confirmed by *in situ* gelatin zymography on a tumor tissue section (Figure 3.12). Multiphoton microscopy revealed a marked increase in QDGelNPs penetration into surrounding tumor tissue as compared with the non-cleavable SilicaQDs control, confirming a substantial enhancement in interstitial transport associated with size change (Figure 3.13 and 3.14). At 6 hours post-injection, the QDGelNPs had penetrated up to $\sim 300 \mu\text{m}$ from the injection site while the SilicaQDs control exhibited little or no dissemination from its initial location. We fitted the concentration profile to a model for substances diffusing from a spherical source to obtain an effective diffusion coefficient of $\sim 2.2 \times 10^{-8} \text{ cm}^2 \text{ s}^{-1}$ inside the tumor (Figure 3.15). This value is $\sim 10\%$ the diffusion coefficient obtained in the collagen gel, which can be explained by the increased time needed to cleave the particles, the geometric tortuosity of the interstitial space induced by cellular obstacles (6), and the possibly higher collagen concentration in the HT-1080 tumor than in the gel we prepared.

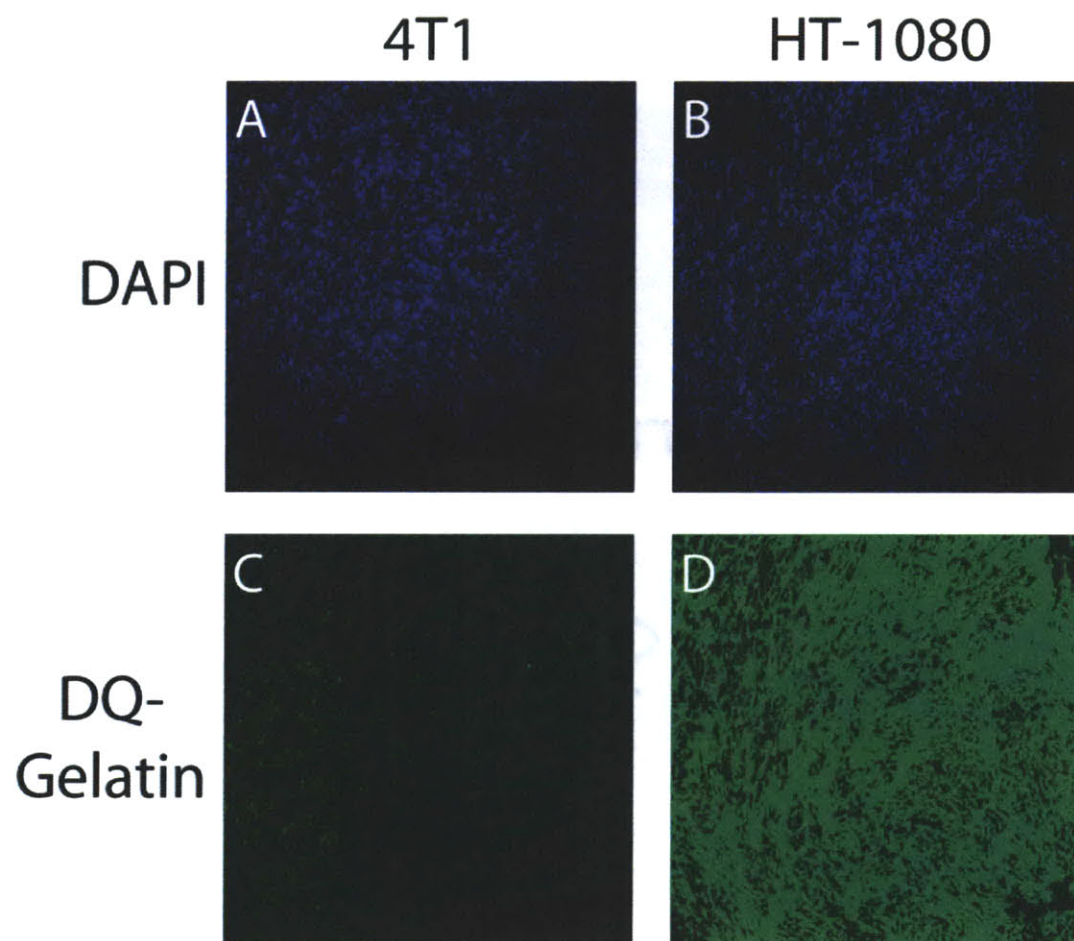


Figure 3.13. *In situ* zymography of gelatinase enzymatic activity in HT-1080 and 4T1 tumor models. DAPI stains for location of nuclei in 4T1 (A) and HT-1080 (B) tumors. Signal from cleaved DQ™ gelatin reveals location of gelatinase activity in 4T1 (C) and HT-1080 (D) tumors. The high DQ™ gelatin signal

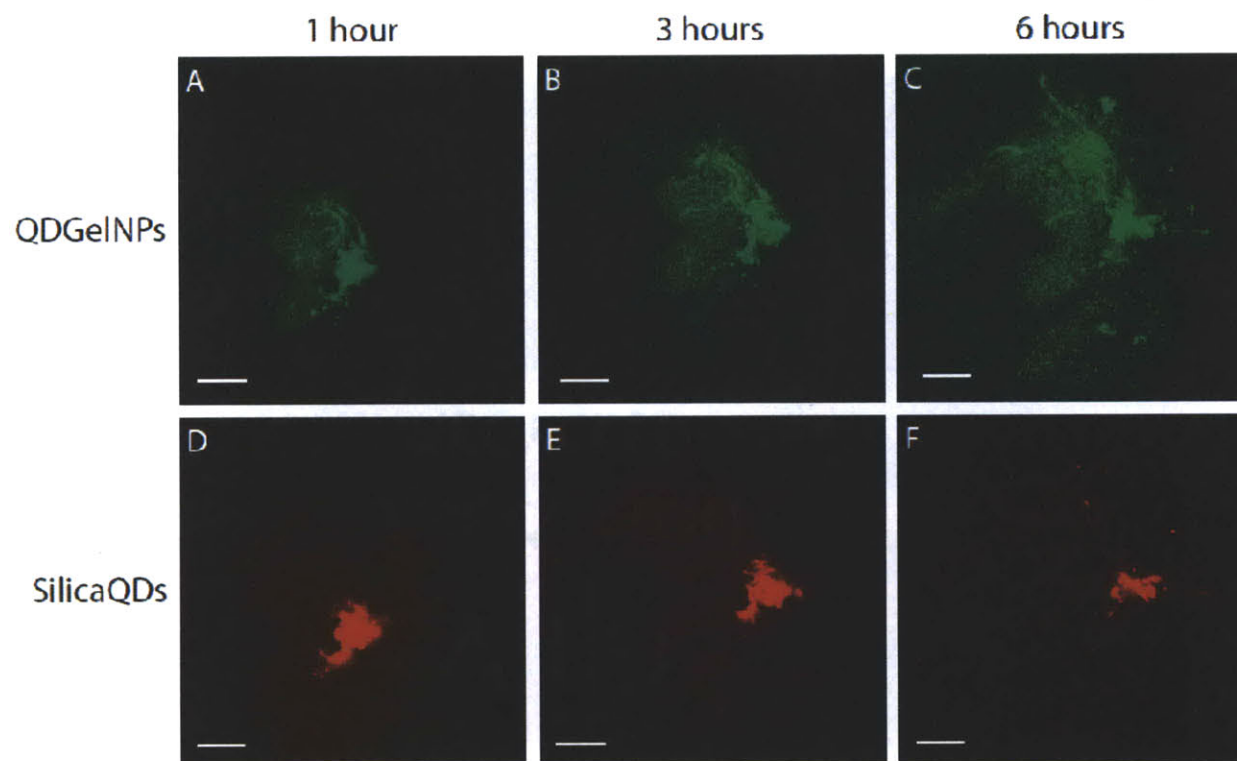


Figure 3.14. *In vivo* images of QDGelNPs and SilicaQDs after intratumoral co-injection into the HT-1080 tumor. QDGelNPs imaged 1 hour (A), 3 hours (B), and 6 hours (C) post-injection. SilicaQDs imaged 1 hour (A), 3 hours (B), and 6 hours (C) injection. Scale bar 100 μm .

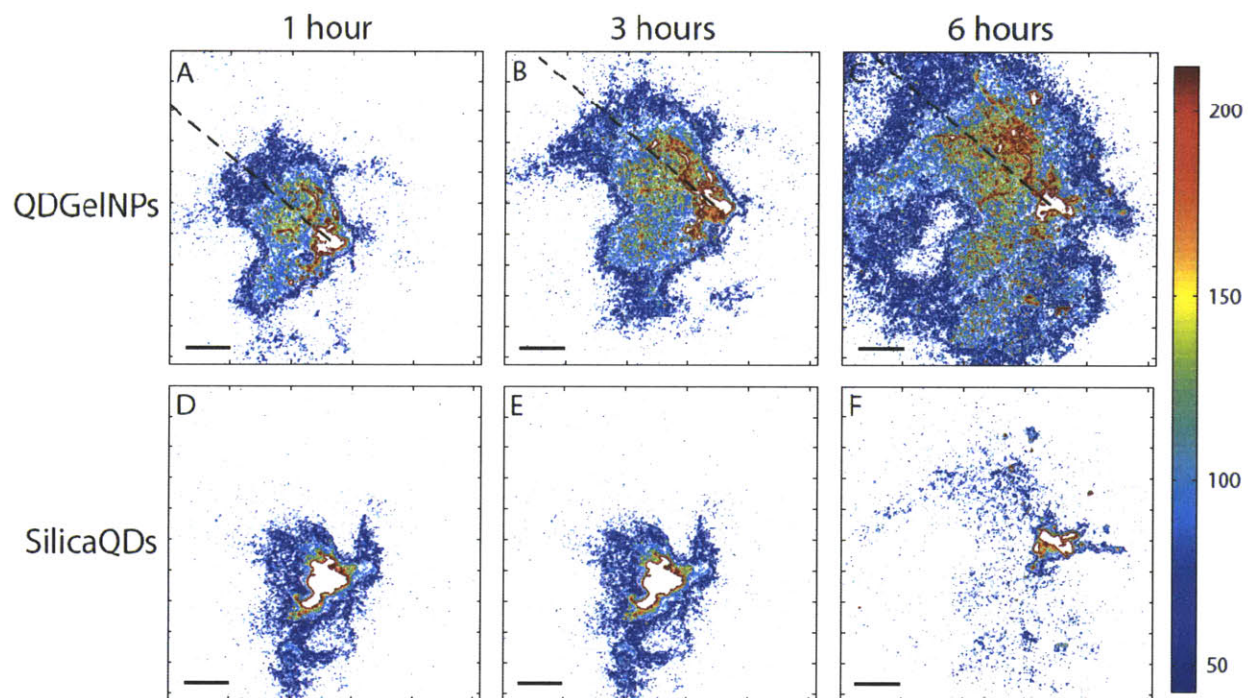


Figure 3.15. Heat map of QDGeINP and SilicaQD distributions after intratumoral co-injection into HT-1080 tumor. QDGeINP heat maps after 1 hour (A), 3 hours (B), and 6 hours (C). SilicaQD heat maps after 1 hour (A), 3 hours (B), and 6 hours (C). Scale bars 100 μm .

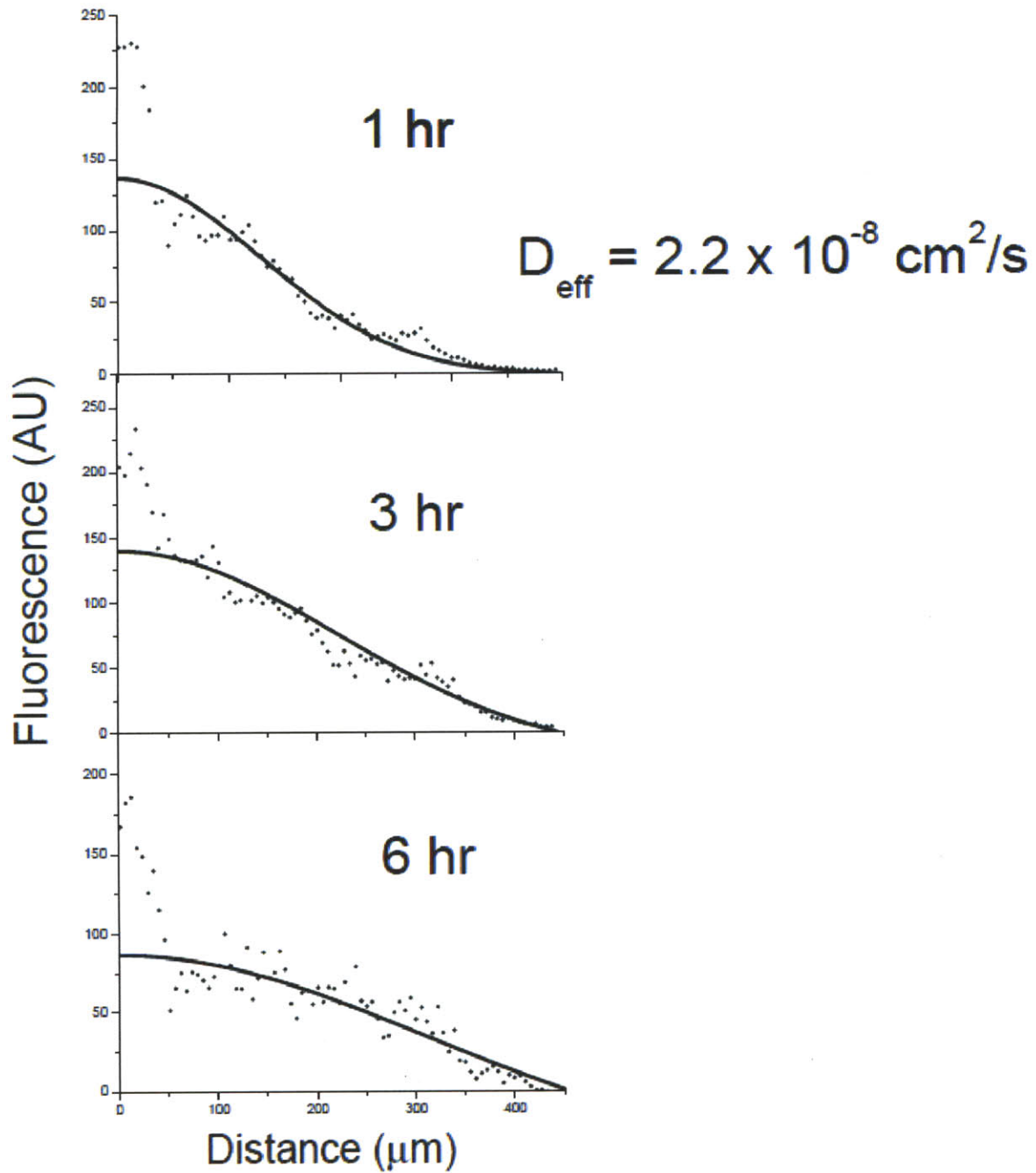


Figure 3.16. Radial intensity profiles of QDGelNP (along dotted line in Figure 3.14) after intratumoral injection in HT-1080 tumor and the corresponding fits from model of diffusing substance from a spherical source.

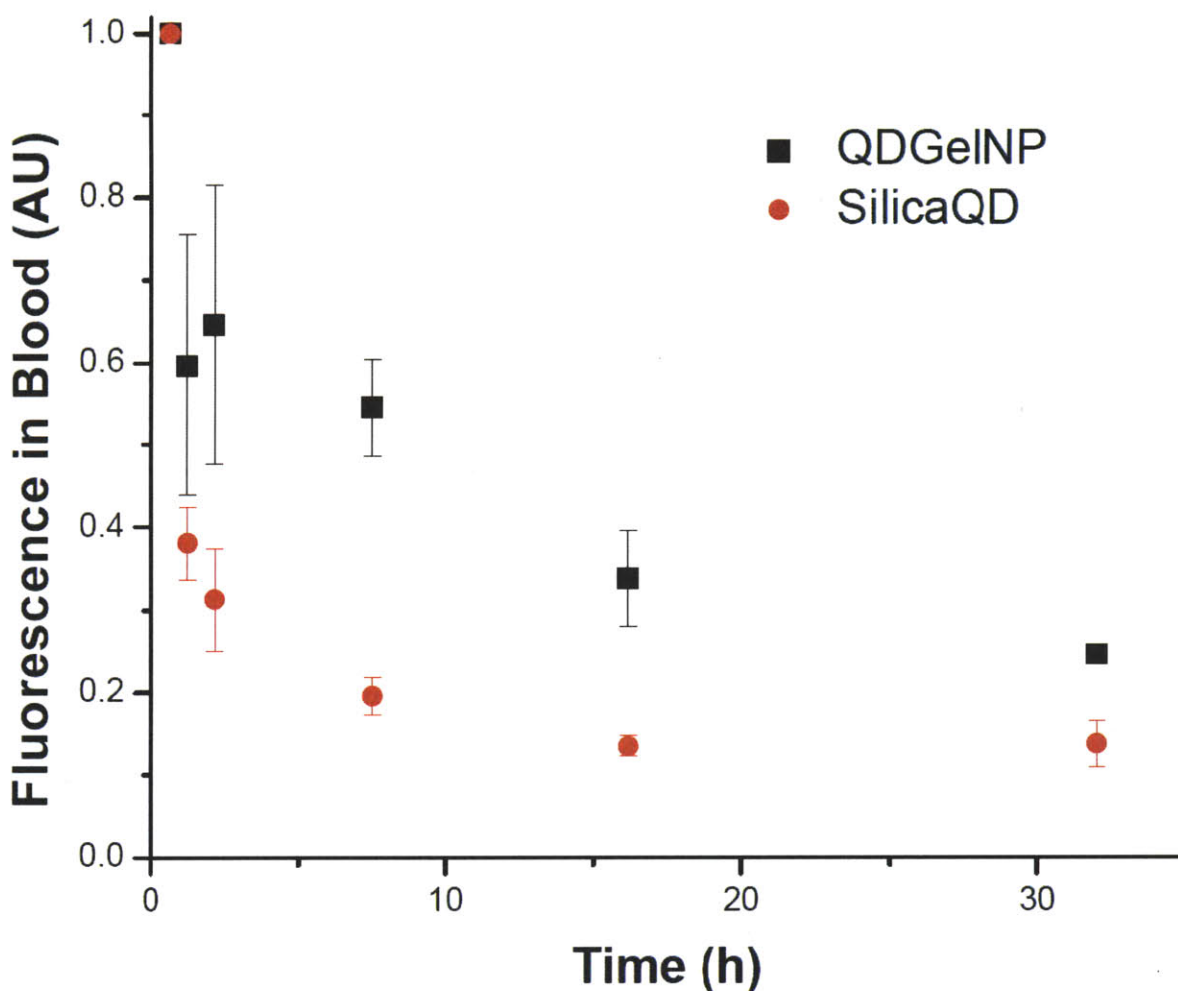


Figure 3.17. Blood concentration of QDGeINPs and SilicaQDs as a function of time post-injection. Error bars indicate standard error of three animals.

We next determined the QDGeINPs' blood half-life ($t_{1/2\beta}$) to show that the QDGeINPs are not rapidly removed from circulation by the reticuloendothelial system (RES). We systemically administered to non-tumor bearing mice a mixture of the QDGeINPs and SilicaQDs by retro-orbital injection and measured the decrease in fluorescence from both particles in the blood over time. The SilicaQDs exhibited a blood half-life of 12.9 ± 2.4 hours while the QDGeINPs had a half-life of 22.0 ± 3.4 hours (Figure 3.16). The difference in the half-lives may be due to variations in the QDGeINPs' surface chemistry that make it less immunogenic compared to SilicaQDs. These results established that QDGeINPs possess both the long circulation half-life and large 100-nm size necessary for preferential

extravasation from the leaky regions of the tumor vasculature as well as the deep interstitial penetration of a 10-nm particle required for delivery to the tumor's poorly accessible regions.

Our FBS incubation experiment suggested the QDGelNPs are stable in serum conditions but additional studies will be needed to verify that the QDGelNPs are not degraded in the blood by circulating MMPs (13) and other proteases. Circulating MMPs, however, have been reported to be inhibited by serum proteins such as α 2-macroglobulin that entrap the MMPs (14, 15). The degree of PEGylation on the surface of the QDGelNPs may need to be optimized such that there is minimal cleaving and opsonization in the blood while achieving the desired release rate in tumor tissue. However, MMP levels may vary in different tumor types/individuals causing inconsistent behavior. A strength of our method is the potential for customized delivery of nanoparticles using genomic and molecular data to achieve optimal delivery for a particular patient. For example, high levels of tumor-specific urinary MMPs measured noninvasively in an individual can be indicative of high levels of the MMPs in plasma and tumor tissues (16). This information can help us customize the QDGelNPs for lower sensitivity to proteases (e.g., by increasing the particles' cross-linking) to minimize degradation in the blood while maintaining the same desired release rate in the tumor.

3.4 Discussion

Multistage nanoparticle systems provide additional tunability in the spatial control of delivery to solid tumors. Due to the multiple physiological barriers that a therapeutic agent must encounter, a multistage nanoparticle system can enhance penetration by changing its size, charge, shape, flexibility and/or surface coating to suit the transport across each barrier. We can extend the utility of this approach by incorporating additional stages into the QDGelNPs to guide its delivery into tumor cells or even subcellular compartment(s). Such an approach may not only improve the efficacy of current anticancer drugs but also make available drugs that have previously been abandoned due to delivery problems. As

interest in increasingly sophisticated delivery systems grows, we face a corresponding challenge to synthesize nanostructures of increasing complexity. Innovative schemes will be necessary to assemble nanocomponents in complex configurations that keep the synthesis simple yet functional so that production can be scalable and cost-effective.

We have provided a proof-of-principle demonstration that a size-changing nanoparticle can facilitate delivery into the dense collagen matrix of a tumor. In future work, we plan to further characterize the particle's biodistribution, pharmacokinetics, and tumor-associated transport properties. Ultimately, the QDs will be replaced with a 10-nm nanocarrier of cancer therapeutics and its antitumor efficacy and survival benefits will be compared to that of conventional drugs and other nanoparticle-based treatments. The loading capacity per 10-nm nanocarrier is limited. Therefore, not only the penetration depth but also sufficient quantity of nanoparticles needs to be delivered.

The size of the nanocarrier we selected for the first and second stage, 100 nm and 10 nm, respectively, may not be the optimal size for transport across each of the physiological barriers the nanoparticles were intended for. The second-stage 10-nm nanocarriers, designed to diffuse in the interstitial space, would probably diffuse even better if they were smaller (e.g., 3-4 nm). The 100-nm nanoparticles used for the first-stage carrier were motivated by current FDA-approved nanomedicine such as the ~100 nm PEGylated liposomal nanotherapeutic Doxil®, which exhibited the EPR effect but does not penetrate well into the interstitial space. However, 100 nm may not be the optimal size for the EPR effect but may have been chosen because synthesizing smaller PEGylated liposomes, such as 10 nm, was not possible. In fact, 6-nm drug-polymer conjugate unimolecular micelles have already been shown to exhibit prolonged circulation time and reduced adverse effects associated with administration of the free drug (17). A 100-nm nanocarrier for the first stage may show even higher reduced adverse effects but more work is still needed to study the effects of nanoparticle size on accumulation in normal tissues such as the bone marrow and heart. 10-nm NPs will likely accumulate in the liver more rapidly due to the liver's 100-nm fenestrations; however, the liver is the endpoint for metabolism of the NPs anyways and is

a relatively robust organ. Thus, if 100-nm and 10-nm NPs have the same circulation half-life, the 10-nm NPs may not be at a disadvantage even if the 10-nm NPs have higher accumulation in the liver. In addition, the 10-nm NPs has higher transvascular flux into tumor tissue due to their smaller size suggesting that the 10-nm NPs will have higher accumulation in tumor tissue. We also demonstrated that 10-nm NPs can penetrate into the tumor's interstitial space quite well. Therefore, a single-stage nanoparticle delivery system that is ~10 nm, PEGylated, and releases drug once it reaches the tumor may already perform better than a 100-nm particle in both tumor accumulation and penetration (assuming they have the same half-life). Further work is necessary to investigate the biodistribution of the 10-nm and 100-nm NPs (along with other sizes) to obtain the optimal size for passive tumor targeting and reduced accumulation in normal tissue. If 10-nm NPs performs similar to 100-nm NPs in these two respects, then single-stage 10-nm NPs (or NPs > ~5 nm and < ~15 nm) may provide a good trade-off between preferential accumulation in tumor and high interstitial transport. In this case, a multistage system can also be designed with 10-nm NPs as the first stage carrier that perhaps releases 3-nm drug nanocarriers. In addition to size-change, a multistage system allows a multi-encapsulation strategy so that the drug is released only after multiple trigger mechanisms.

In addition to the size, the NPs' material and surface properties must also be considered. The very long half-life of 100-nm PEGylated liposomes is not only due to the 100-nm size but also because of the nature of PEGylated liposomes. Doxil® has a low clearance (mean: 0.03 liter/h/m²) and long half-life (mean: 36.4 h, some have reported times of 40-60 hours), typical of drugs encapsulated in PEGylated liposomes. However, we have observed that PEGylated ~100nm SilicaQD NPs only have a half-life of 12.9 ± 2.4 hrs. Even though both Doxil® and SilicaQD NP are approximately the same size and PEGylated, there are still differences in the surface moiety and perhaps compressibility that play a major role in the particles' pharmacokinetics. So one cannot realistically consider the design of a nanoparticle drug delivery system based on size alone but also take into account the material used for the core and the surface properties. The surface PEGylation is difficult to emulate on NPs of different materials. Since

most types of NPs can only be synthesized within a certain size range, compromises sometimes need to be made between the size, core material, and surface that are used to obtain the desired properties. In the case of a drug delivery particle, compromises need to be made regarding the many properties desirable in a drug nanocarrier (see section 1.4). A major obstacle with multistage drug delivery systems is that they must exhibit the desirable properties of drug delivery nanoparticles (high entrapment efficiency may be difficult) in addition to changing size.

3.5 References

1. O. R. F. Mook, C. Van Overbeek, E. G. Ackema, F. Van Maldegem, W. M. Frederiks, *J. Histochem. Cytochem.* **51**, 821 (2003).
2. M. A. Clauss, R. K. Jain, *Cancer Research* **50**, 3487 (1990).
3. S. Ramanujan *et al.*, *Biophysical Journal* **83**, 1650 (2002).
4. T. Stylianopoulos *et al.*, *Biophysical Journal* **99**, 1342 (2010).
5. M. Leunig *et al.*, *Cancer Research* **52**, 6553 (1992).
6. V. P. Chauhan *et al.*, *Biophysical Journal* **97**, 330 (2009).
7. T. D. McKee *et al.*, *Cancer Res* **66**, 2509 (2006).
8. E. B. Brown *et al.*, *Nature Medicine* **7**, 864 (2001).
9. J. Crank, *The mathematics of diffusion*. (Oxford University Press, USA, 1979).
10. Z. Popović *et al.*, *Angewandte Chemie International Edition* **49**, 8649 (2010).
11. H. Hatakeyama *et al.*, *Gene Ther* **14**, 68 (2007).
12. P. A. Netti, D. A. Berk, M. A. Swartz, A. J. Grodzinsky, R. K. Jain, *Cancer Research* **60**, 2497 (2000).
13. S. Zucker, R. M. Lysik, M. H. Zarrabi, U. Moll, *Cancer Research* **53**, 140 (1993).
14. J. F. Woessner, H. Nagase, *Matrix metalloproteinases and TIMPs*. (Oxford University Press, Oxford, UK, 2000).
15. Y. Chau, F. E. Tan, R. Langer, *Bioconjugate Chemistry* **15**, 931 (2004).
16. R. Roy, J. Yang, M. A. Moses, *Journal of Clinical Oncology* **27**, 5287 (2009).
17. L. H. Reddy, P. Couvreur, R. K. Jain, *Macromolecular Anticancer Therapeutics*. (Springer Verlag, New York, 2009), pp. xx, 623 p.

Chapter 4

Electrically Controlled Catalytic Growth of Nanowires

4.1 Introduction

One dimensional nanostructures such as nanorods, carbon nanotubes and nanowires are promising candidate materials for bottom-up assembly of electronic and optoelectronic devices. 1-D nanomaterials have demonstrated excellent electrical properties that rival conventionally-made materials, creating the possibility that they could function as building blocks for self-assembling nanoelectronic devices and circuits without having to resort to complex and costly semiconductor microfabrication facilities. Several groups have used these nanomaterials to demonstrate miniature sensors, light emitting diodes (LED), lasers, diodes, transistors (1), bioanalytical devices (2), etc. However, to realize bottom-up assembly of complex nanocircuitry based on 1-D nanocomponents, strategies have to be developed having the ability to organize large numbers of components in a massively parallel manner into predetermined functional architectures and electrically addressable nanoscale devices. While fluidic and electric field self-assembly methods can direct nanowires into limited scale structures such as ordered arrays, these techniques are not appropriate for maneuvering them in large numbers into an integrated nanowire circuit.

Several approaches have been developed to place a nanowire in between two electrodes. In this way, its electrical characteristics can be directly probed and used in a device. To place a nanowire in between two electrodes, the location and orientation need to be controlled. Aligning nanowires and nanorods with patterned electrodes could potentially be an inefficient and time-consuming process. DC and AC electric fields have been shown to align the growth direction of carbon nanotubes (3) and nanowires (4). Another method involves directing nanowires (5) and nanorods (6) in between electrodes using an electric-field based alignment method. When a voltage is applied between two micropatterned electrodes, charge carriers of opposite sign are accumulated at opposite electrodes and an electric field is produced. If a nanowire in solution approaches this field, the applied electric field induces a polarization within the wire and attracts the wire toward the electrode. The attraction results in the wire bridging the gap between the electrodes, which quenches the attraction and prevents a second wire from bridging the gap. In addition, magnetic fields have been shown to manipulate dielectric nanowires suspended in liquid media (7).

A microfluidic approach has also been used to direct the assembly of nanowires into functional arrays (8). Microfluidic channels are aligned under a microscope with electrodes which have been previously patterned on a substrate. A drop of nanowire suspension is flowed into the microchannels by capillary forces, and solvent evaporation aligns the nanowire at the edge of the channel.

The Langmuir-Blodgett (LB) transfer technique can be used to produce large two dimensional arrays of packed nanowires (9) and nanorods (10). This technique has been shown to transfer 1-D structures such as hydrophobized silver nanowires, which are found to float at a water-air interface. Compression of the interface increases the surface density of nanowires, and aligns them into ordered phases and controlling the pitch between the wires. This monolayer can be transferred onto a substrate by slowly withdrawing the substrate through the interface and by keeping the surface pressure constant. Multiple steps of LB assembly and deposition, followed by photolithography, have also resulted in hierarchical crossbar arrays (11).

We have developed a method of combining the synthesis and assembly of nanowires in a predetermined architecture in a single step (12). Our novel method first defines the position of nanowire growth by depositing catalytic particles on lithographically defined positions on a substrate and then induces nanowire growth from the catalytic particle using an applied electric field. The macroscopic flow of nanowire material is also guided by the applied electric field. Since the nanowires are grown to bridge the gap between electrodes, each nanowire device is already electrically addressable. Our technique can fabricate many nanowire devices in parallel and is thus highly scalable.

Semiconducting nanowires are commonly synthesized using the vapor-liquid-solid phase (VLS) technique (13). Precursor material from laser ablation of source material or feed gas delivers the source materials for nanowire growth. The source material is flowed and exposed to a heated catalyst particle. The source enters the catalyst and saturates the particle. When supersaturation of the catalyst is reached, the source element phase separates (solidifies) and grows outward out from the catalyst particle, forming a “nanowire”. A solution phase analog of the VLS mechanism is the solution-liquid-solid (SLS) growth (14). In SLS, the catalyst particle and source material are in solution. The SLS technique limits the catalyst particles to those that are active below the boiling temperature of the solvent. The Park group has demonstrated SLS nanowire growth from bismuth catalysts deposited on a substrate (15). We extend upon this technique by using voltage and electric field to influence the growth of the nanowires.

4.2 Materials and Methods

Note: The experiments were performed in collaboration with Dr. August Dorn.

4.2.1 Materials

Cadmium oxide (99.999%, Alfa Aesar), 1-tetradecylphosphonic acid (TDPA, 98%), and selenium shot (99.999%) were purchased from Alfa Aesar. Trioctylphosphine oxide (99%) was purchased from Sigma-Aldrich. Tri-n-butylphosphine (99%) was purchased from Strem Chemicals.

4.2.2 Experimental Setup

Schematic and images of the experimental setup are shown in Figure 4.1 and 4.2. The tube and clips used for mounting the sample were made of stainless steel and the wires were insulated with Teflon (Figure 4.2). Quartz or degenerately doped silicon with a 300nm oxide layer were used as sample substrates and electrodes were defined with optical lithography and typically consisted of a 5nm Ti adhesion layer, a 50 nm platinum layer, and a 20 nm bismuth layer.

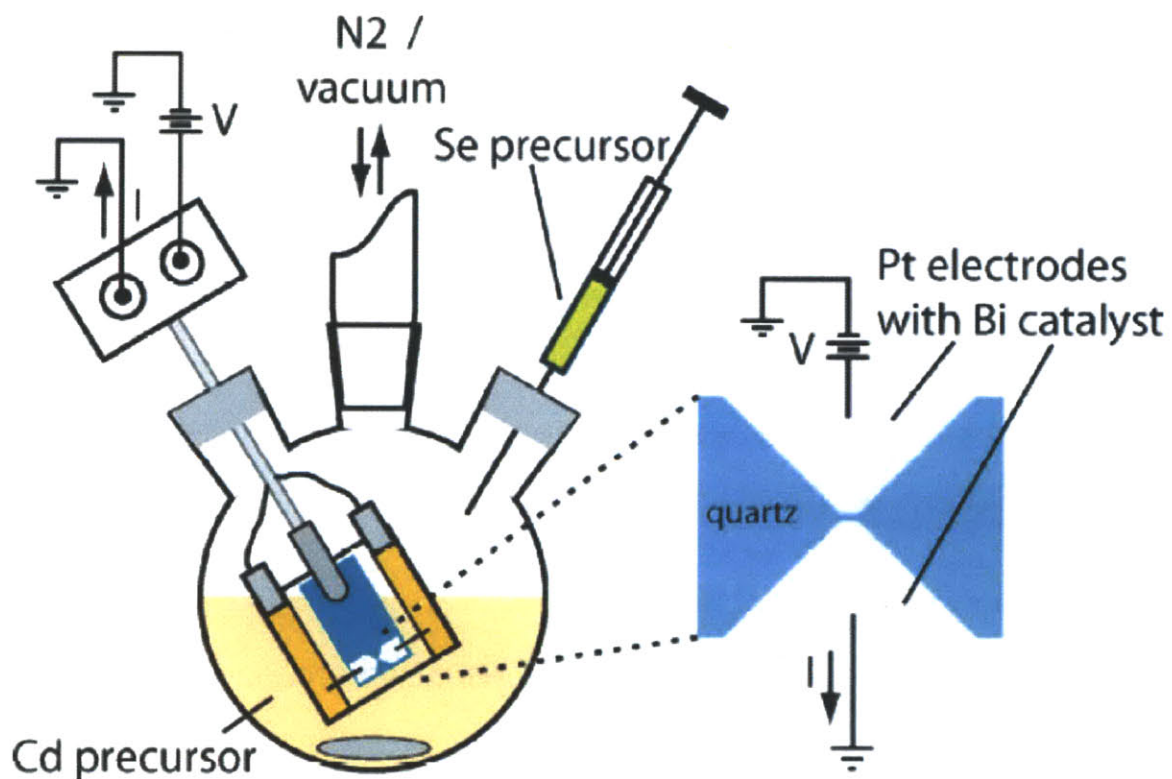


Figure 4.1. Schematic of the experimental setup. The actual flask has a fourth neck for inserting a temperature sensor which is not shown.

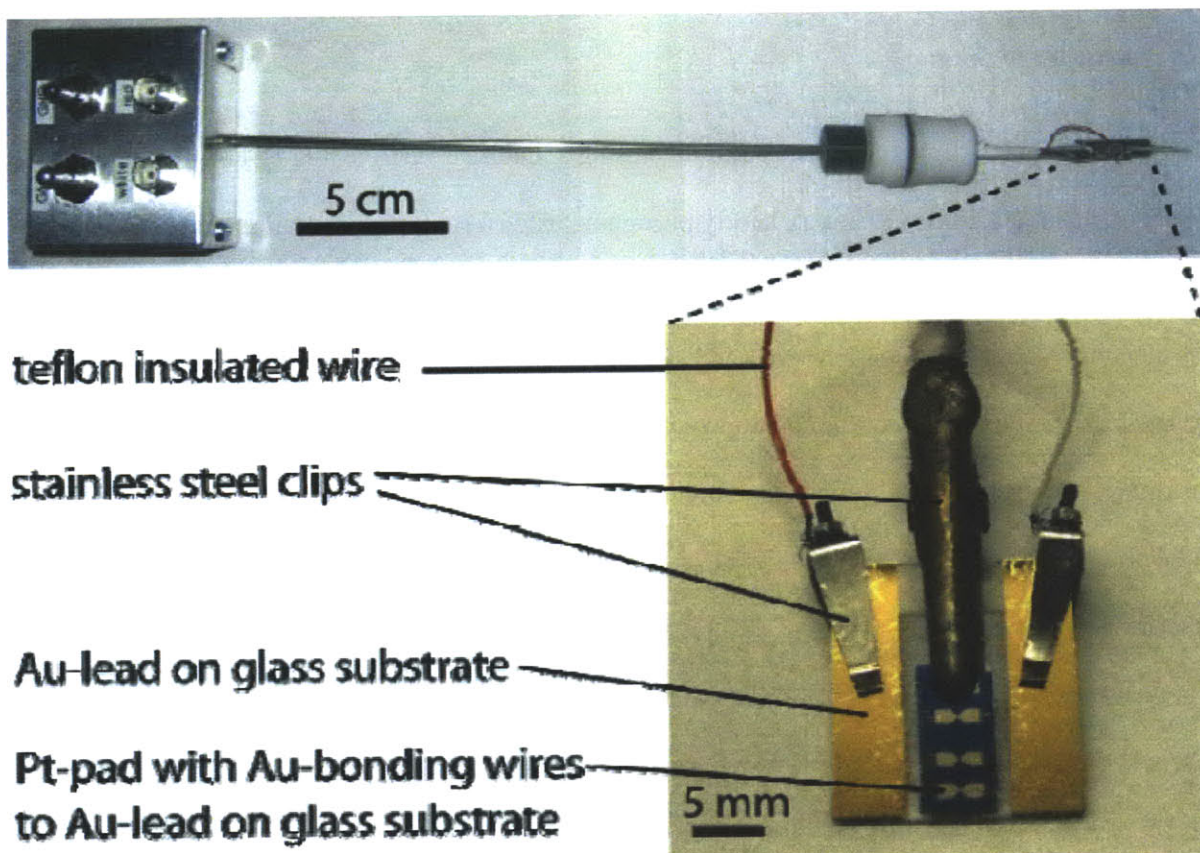


Figure 4.2. Images of the experimental setup used to apply bias voltages to the electrodes in the precursor solution

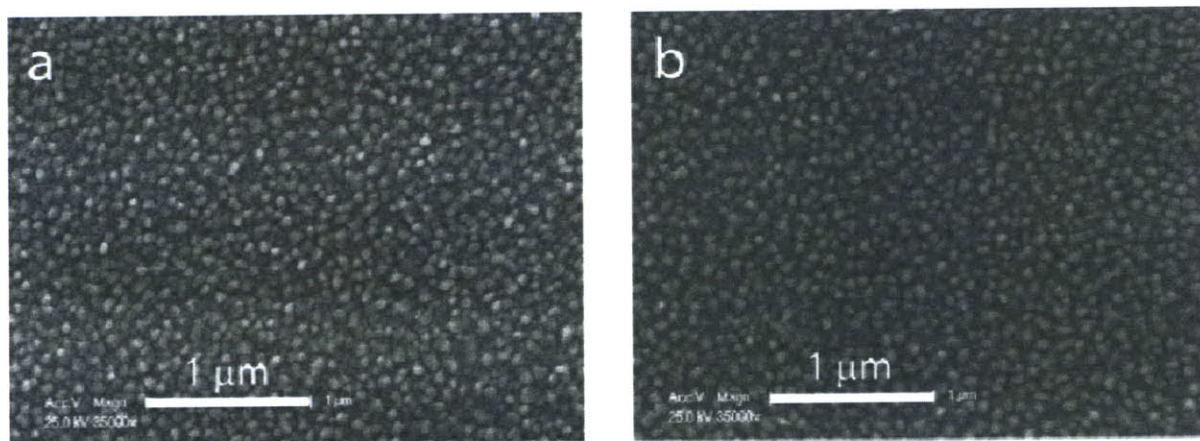


Figure 4.3. SEM images of 20 nm Bi layers thermally evaporated onto Pt electrodes a) before and b) after being exposed to wire synthesis conditions.

4.2.3 Nanowire Synthesis

CdSe nanowire synthesis was performed using a modified version of (15). For the cadmium precursor, cadmium oxide (19.2 mg), trioctylphosphine oxide (20 g), and 1-tetradecylphosphonic acid (85.6 mg) were loaded into a four-neck flask and heated to 140°C for 30 min under vacuum. The solution was then placed under 1 atm of nitrogen and heated to 300°C over the course of 1 hour. The solution turned clear upon formation of the cadmium–TDPA complex. For the selenium precursor, selenium shot was dissolved in tri-n-butylphosphine overnight in a glove box under nitrogen atmosphere, to form TBP–selenium (25 wt %), a clear colorless liquid. After the cadmium–TDPA complex was formed, the temperature was reduced to 285°C, the sample was lowered into the cadmium-precursor solution, the voltage was applied using a Yokogawa DC voltage source, and 80 μL of the selenium precursor were injected. After a period of typically 300 s, the sample was withdrawn from the solution and the voltage was set back to 0 V. Once the flask had cooled to below 150°C, the sample was removed and rinsed with hexanes.

4.3 Results and Discussion

The center of the experimental setup consisted of a substrate patterned with pairs of optical lithography defined platinum electrodes separated by a gap (Figure 4.1). The surface of the electrodes was covered with bismuth catalysts islands, which formed spontaneously when layers of bismuth were thermally deposited onto the platinum layer (Figure 4.3) (16). The substrate was attached to a custom-built pole that allowed electrical contact with the platinum electrodes (Figure 4.2) and submersion into a round bottom flask containing a solution of Cd precursors (cadmium-TDPA complex) at 285 °C. A voltage was applied (varied from 0 to 5 V) between the platinum electrodes and a selenium precursor (TBP-Se) was injected. CdSe nanowires were allowed to grow for 5 minutes before the substrate was withdrawn from solution and rinsed with hexane.

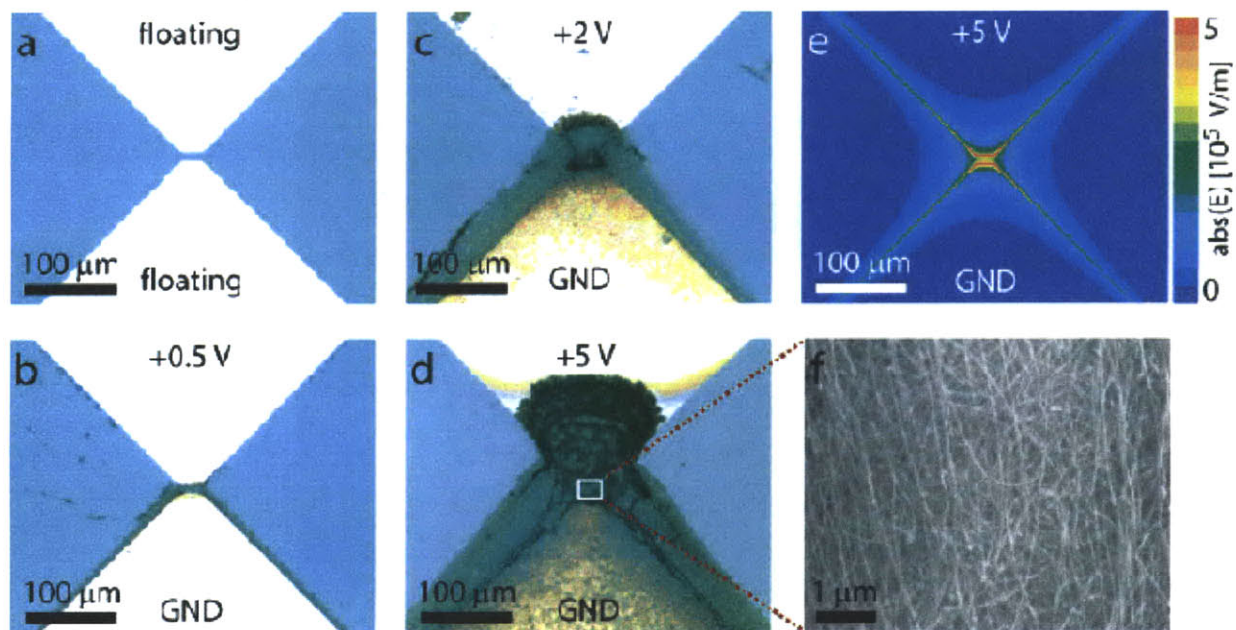


Figure 4.4. Voltage and electric-field dependence of CdSe-nanowire growth. (a-d) CdSe-wire growth off 5 nm Ti/50 nm Pt/20 nm Bi electrodes on quartz substrates at a series of voltages from 0 V to 5 V at 285°C for 300 s. (e) Finite element simulation of the magnitude of the electric field in the substrate plane (f) Scanning electron microscope image of the CdSe wire mat from (d)

Optical and scanning electron microscopy revealed that the nanowire growth was highly dependent on the applied electric potential and wire growth did not occur without an applied electric potential (Figure 4.4, 4.5a). This observation differs from previous reports that demonstrated nanowire growth in solution or on substrates without the need of an applied electric potential (17-19). This surprising result suggests electrically controlled catalytic nanowire growth can be used to selectively induce nanowire growth in predetermined locations only by applying a modest electric potential. Another surprising observation was that the nanowires only grew from the negative electrode. SEM images also revealed that the individual wires were randomly oriented. However, the macroscopic flow of nanowire material appeared to be guided by the applied electric field. We also tested the effect of applying an electric field perpendicular to the plane of the electrodes using a conducting back gate (Figure 4.9), but this did not have any noticeable effects on the nanowire growth.

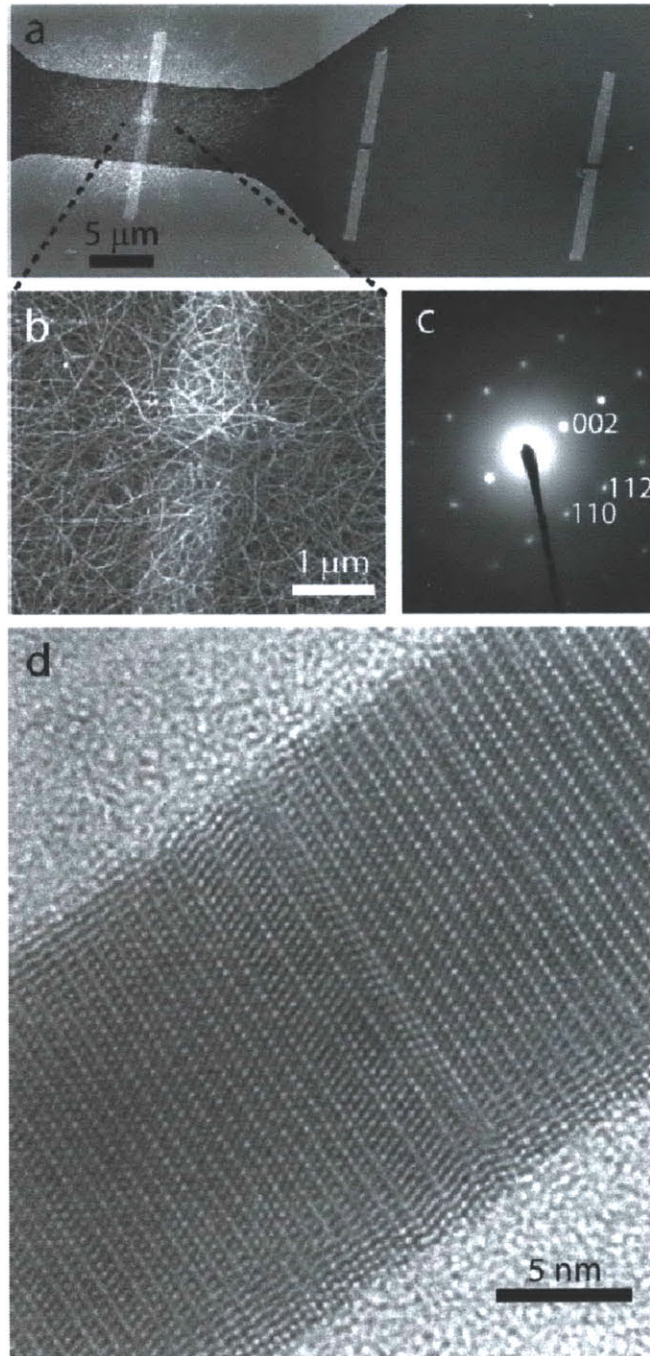


Figure 4.5. Morphology and crystal structure of CdSe nanowires grown by electrical excitation (a) Scanning electron microscope image of microstructured 5 nm Ti/50 nm Pt/20 nm Bi electrodes on a degenerately doped, conducting silicon substrate with a 300 nm layer of insulating thermal oxide after wire growth at 0.5 V at 285°C. Wire growth emanates from the grounded electrodes in the region of highest electric field in the gap, while two identical electrodes to the right, that are not biased, show no wire growth. (b) Close up of a). (c) Electron-diffraction pattern from a single wire recorded with a TEM in nanobeam mode, showing the typical wurtzite $\langle 001 \rangle$ growth direction. (d) High-resolution TEM image of a nanowire with stacking faults (20).

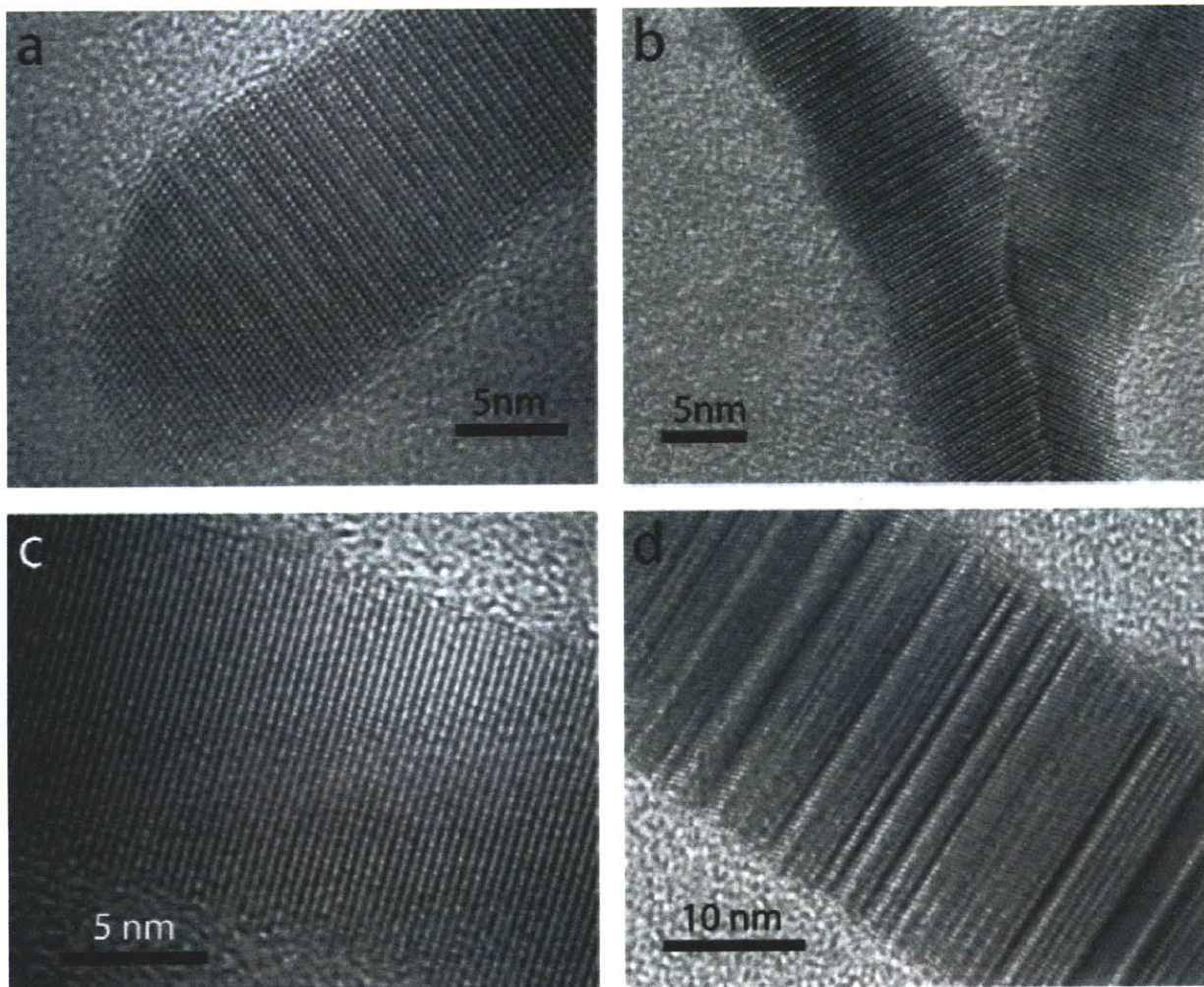


Figure 4.6. High-resolution TEM images of CdSe wires. (a) Tip of a wire (b) Example of a Y-branched wire. (c) example of a single crystalline segment. (d) wire segment with a high degree of twinning and phase changes along the axial growth direction.

We characterized the CdSe using high resolution transmission electron micrograph (HRTEM) and electron diffraction. The results indicated that the crystal structure of the wires were mainly wurtzite (Figure 4.6c) and the nanowires grew along the $\langle 001 \rangle$ direction (Figure 4.5c). Similar to previous reports of SLS growth of nanowires, HRTEM of the nanowires showed stacking faults, segments with zinc blende orientation (Figure 4.6d), and Y-branched structures (Figure 4.6b) (21). Scanning transmission electron microscopy of the nanowires with energy-dispersive X-ray (EDX) elemental analysis showed a 1:1 ratio composition of Cd to Se along the length of the wire (Figure 4.7), confirming that the nanowires were composed of CdSe. The diameter of the nanowire was found to correlate with the size of the bismuth island that it grew from, which can be controlled through varying the thickness of the bismuth film deposited (Figure 4.8). The average diameter of the wire was about 30% smaller than the diameter of the bismuth catalyst.

During the wire-growth process, the conductivity measured across the electrode was typically between $10 \text{ k}\Omega$ and $10 \text{ M}\Omega$. The conductivity remained the same or increased slightly after injection of the selenium precursor, possibly due to bridging of the gap between the electrodes by the nanowires. Moreover, the conductivity remained the same even as the selenium precursors became depleted from solution. The wire growth appeared to be dependent primarily on the applied voltage and not on the total charge that passed through the electrodes (as in electrodeposition).

We used Maxwell® Ansoft simulation software for finite-element modeling of the electric field in the substrate plane (Figure 4.4f). The TOPO precursor solution was modeled as an insulator with a dielectric constant of 2.5. The regions of wire growth from imaging were found to have a strong association with the locations in the simulation with high electric field strengths and the corresponding high surface charge density induced in the electrodes. The electrode asymmetry of nanowire growth in our experimental result compared to simulation was due to the nanowires only growing from the negative electrodes. The simulation showed the maximum electric field amplitude was located at the edge of the electrode due to electric field bunching (22), which was also the region of the highest nanowire growth.

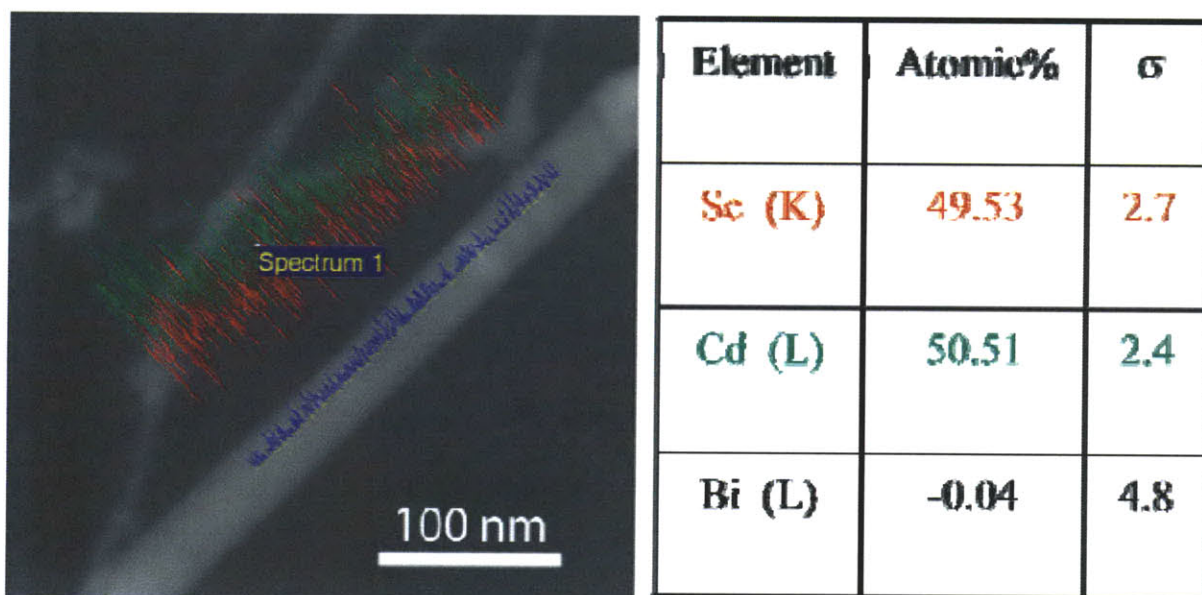


Figure 4.7. Elemental analysis of a wire with Scanning Transmission Electron Microscope (STEM). The red trace indicates the selenium concentration and the green trace indicates the cadmium concentration along the highlighted wire segment. The table lists the average percentage of selenium, cadmium, and bismuth atoms along the marked wire segment based on the integrated number of counts.

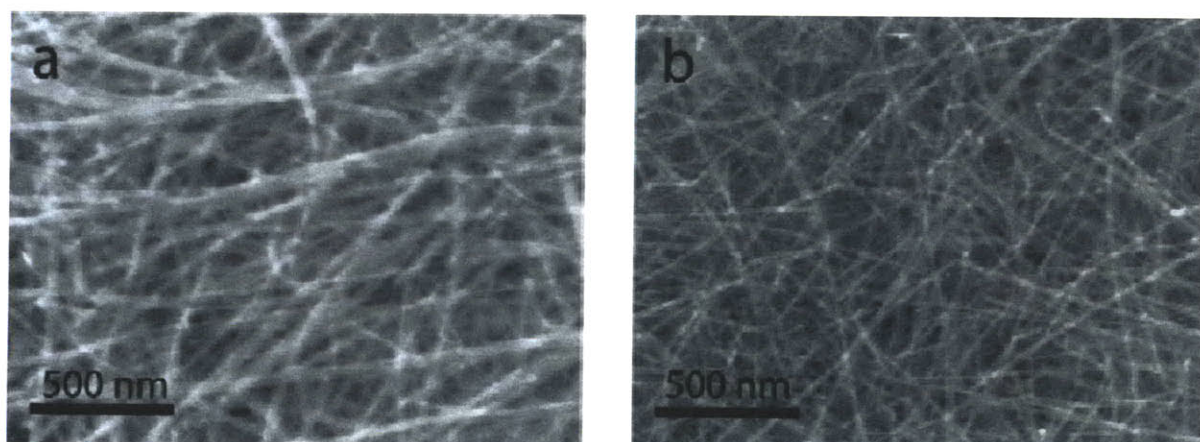


Figure 4.8. CdSe wires grown off bismuth layers with different thicknesses. Scanning electron microscope images of CdSe nanowires grown off Pt electrodes at 285 °C at a bias of 2 V for 300 seconds with (a) a 20 nm Bi layer and (b) a 2 nm layer.

We next characterized the fluorescent properties of the wire mat. The photoluminescence spectrum peaked at 713 nm, which corresponded to the bulk CdSe bandgap of 1.74 eV. Since the diameter of the wire ($\sim 20 \pm 10$ nm) was notably bigger than the Bohr diameter of bulk CdSe (11.2 nm), quantum confinement effects were negligible.

We next performed photoconductivity measurements to demonstrate that electrically controlled nanowire growth can be a potential method for fabricating devices such as a photodetectors. An Ar-ion laser (514 nm line) was used to illuminate the nanowire mat in between a 10 μm wide gap between the electrodes after nanowire growth and the I-V curve was measured (Figure 4.11). Over 80% of the devices showed photoconductivity without any additional post-treatment beyond hexane rinsing. The I-V curve showed high symmetry when voltage was applied in either direction, indicating the nature of the contacts on both electrodes was similar. The resistance of the wire mat in the dark was above 1 T Ω and the resistance near saturation (3×10^5 W m⁻² illumination) was ~ 20 M Ω , indicating an on/off ratio of $\sim 10^5$. The near-random orientation of the nanowire showed no polarization dependence in photoconductivity, similar to another predominantly random nanowire network from a previous report (23).

We attempted to create an electrically addressable single nanowire device by inducing the growth and alignment of a single nanowire to bridge the gap in between the electrodes. A single large bismuth particle was placed near the tip of each platinum electrode and an electric field was placed across the electrode as before. Several CdSe nanowires grew off the bismuth bead from the negative electrode; however, the applied electric field did not have an observable effect on the orientation of the nanowire and thus the wires did not preferentially bridge the gap (Figure 4.10). Perhaps the kinetics of the wire growth process was too fast or the temperature was too high for the forces from the applied electric field to have a significant effect. This problem may be a major limitation in applying this method for bottom-up assembly of nanocircuitry.

We proposed a possible mechanism for the strong dependence of nanowire growth on applied electric field. The large difference in work function between bismuth and platinum may result in extraction of electrons from the bismuth islands into the platinum substrate. The resulting lower work function of the bismuth (slight positive charge) and lower electron density may result in quenching of its catalytic activity, and in turn the inability to catalyze nanowire growth at zero bias. The lower electron density may hinder the ability for the catalytic particle to undergo redox reactions with the Cd^{2+} and Se^{2-} precursors. This proposed mechanism also explains the growth of wires only from the negative electrode as the applied negative voltage can offset the lower work function and compensate for the lower electron density. However, further modeling and characterization is necessary to investigate and validate the microscopic mechanism behind electrically controlled nanowire growth.

We demonstrated that growth of CdSe nanowires through the SLS mechanism under certain conditions can be strongly influenced by an applied electric field. This method adds to the arsenal of tools scientists can use to integrate nanocomponents for large scale integration. In addition to growth of CdSe nanowires, further works have demonstrated this technique can be applied to growth of InP nanowires (24) and conversion of CdSe nanowires into Ag_2Se nanowires (25). The low temperature necessary for the growth of nanowires via the SLS mechanism compared to VLS makes this a promising approach for incorporation with conventional silicon-based technology.

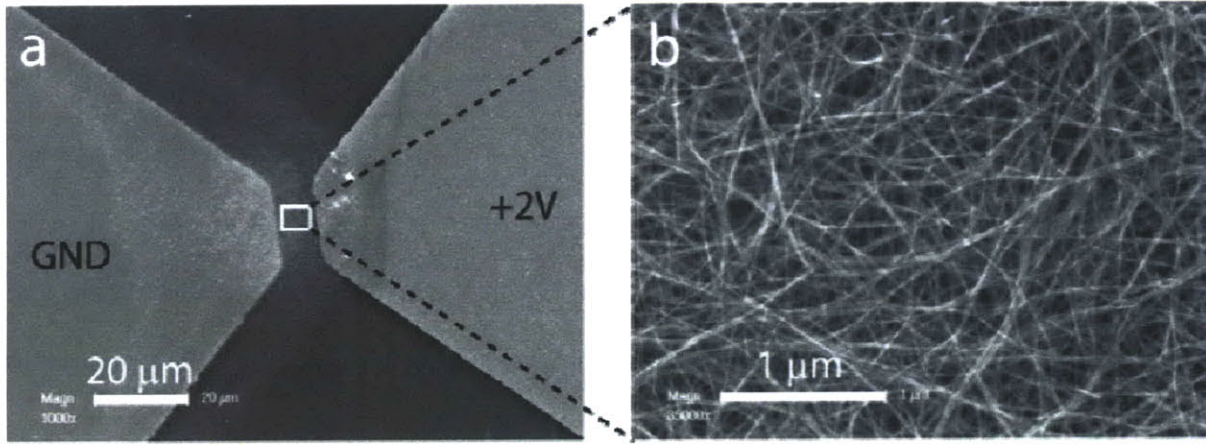


Figure 4.9. CdSe wires grown on a substrate with a conducting back gate. (a) CdSe wires grown at 285°C at a bias of 2V for 300 seconds on a doped silicon substrate with 300 nm of thermal oxide. The electrode geometry is the same as the one used in Figure 4.4. (b) Close up of the region highlighted in (a).

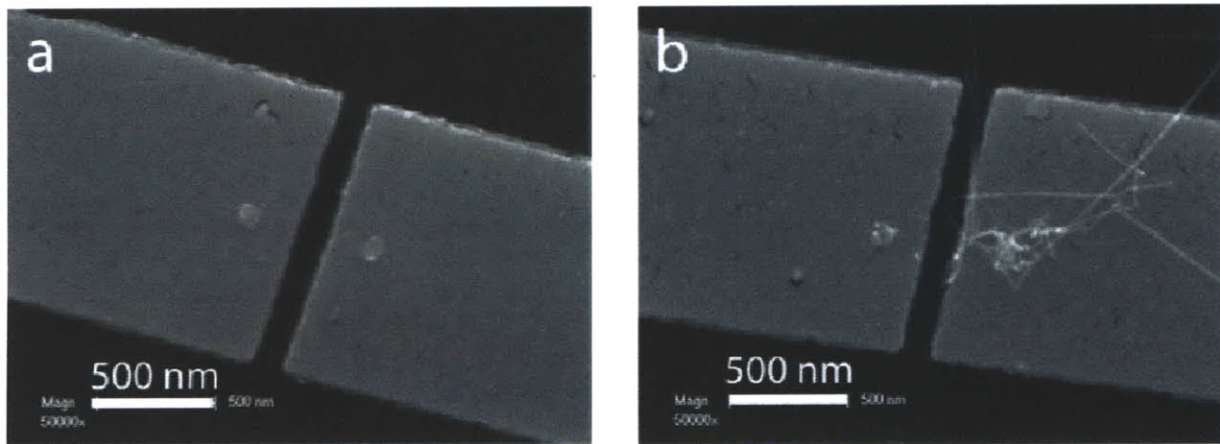


Figure 4.10. CdSe wires grown off single bismuth beads. (a) Two single Bi beads defined by electron beam lithography with a diameter of about 80 nm and a thickness of 50 nm on two platinum electrodes. (b) Sample similar to the one shown in (a) after CdSe wire growth at 275°C at a bias of +0.5V for 300s.

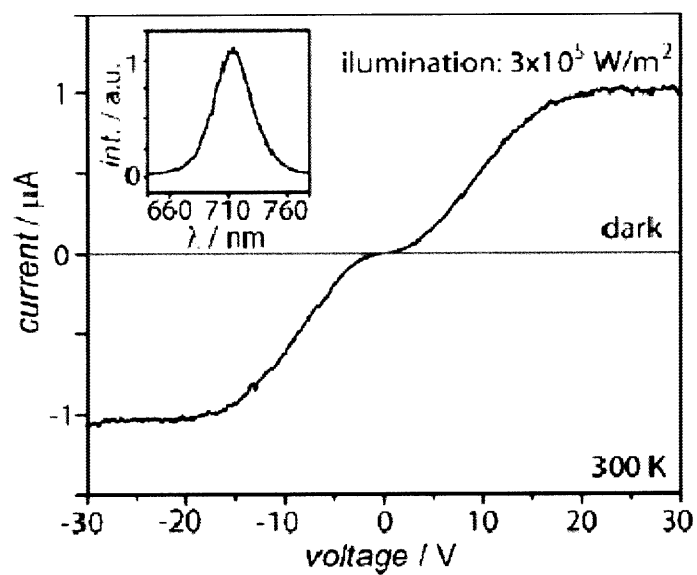


Figure 4.11. Photoconductivity. Current-voltage characteristic of a sample grown at 0.5 V, as shown in Figure 4.5b, under illumination with the 514 nm line of an Ar-ion laser at $3 \times 10^5 \text{ W m}^{-2}$, Inset: corresponding photoluminescence spectrum.

4.4 References

1. Y. Cui, Z. H. Zhong, D. L. Wang, W. U. Wang, C. M. Lieber, *Nano Letters* **3**, 149 (2003).
2. G. F. Zheng, F. Patolsky, Y. Cui, W. U. Wang, C. M. Lieber, *Nat Biotechnol* **23**, 1294 (2005).
3. E. Joselevich, C. M. Lieber, *Nano Letters* **2**, 1137 (2002).
4. O. Englander, D. Christensen, J. Kim, L. W. Lin, S. J. S. Morris, *Nano Letters* **5**, 705 (2005).
5. P. A. Smith *et al.*, *Appl Phys Lett* **77**, 1399 (2000).
6. K. M. Ryan, A. Mastroianni, K. A. Stancil, H. T. Liu, A. P. Alivisatos, *Nano Letters* **6**, 1479 (2006).
7. M. Tanase *et al.*, *Nano Letters* **1**, 155 (2001).
8. Y. Huang, X. F. Duan, Q. Q. Wei, C. M. Lieber, *Science* **291**, 630 (2001).
9. A. Tao *et al.*, *Nano Letters* **3**, 1229 (2003).
10. F. Kim, S. Kwan, J. Akana, P. D. Yang, *Journal of the American Chemical Society* **123**, 4360 (2001).
11. D. Whang, S. Jin, Y. Wu, C. M. Lieber, *Nano Letters* **3**, 1255 (2003).
12. A. Dorn, C. R. Wong, M. G. Bawendi, *Advanced Materials* **21**, 3479 (2009).
13. Y. Y. Wu, R. Fan, P. D. Yang, *Nano Letters* **2**, 83 (2002).
14. H. Yu, W. E. Buhro, *Advanced Materials* **15**, 416 (2003).
15. L. Ouyang, K. N. Maher, C. L. Yu, J. McCarty, H. Park, *Journal of the American Chemical Society* **129**, 133 (2007).
16. M. T. Paffett, C. T. Campbell, T. N. Taylor, *J Chem Phys* **85**, 6176 (1986).
17. F. D. Wang *et al.*, *ACS Nano* **2**, 1903 (2008).
18. F. Wang *et al.*, *Journal of the American Chemical Society* **129**, 14327 (2007).
19. J. Puthusseray, T. H. Kosel, M. Kuno, *Small* **5**, 1112 (2009).
20. J. W. Grebinski, K. L. Hull, J. Zhang, T. H. Kosel, M. Kuno, *Chem Mater* **16**, 5260 (2004).
21. K. L. Hull, J. W. Grebinski, T. H. Kosel, M. Kuno, *Chem Mater* **17**, 4416 (2005).
22. J. D. Jackson, *Classical electrodynamics*. (Wiley, New York, ed. 3rd, 1999), pp. xxi, 808 p.
23. A. Singh *et al.*, *Nano Letters* **7**, 2999 (2007).
24. A. Dorn, P. M. Allen, M. G. Bawendi, *ACS Nano* **3**, 3260 (2009).
25. A. Dorn, P. M. Allen, D. K. Harris, M. G. Bawendi, *Nano Letters* **10**, 3948 (2010).

Cliff R. Wong

M.I.T., 18-073, 32 Vassar St. Cambridge, MA 02139 Phone: 951-CLIFFRW email: cliff.r.wong@gmail.com
Nationality: U.S. Citizen

Education

MASSACHUSETTS INSTITUTE OF TECHNOLOGY
Ph.D. Physical Chemistry

Cambridge, MA
February, 2011

RICE UNIVERSITY

B.S. Chemical Physics and Applied Physics
B.S. Electrical Engineering- specialization in semiconductor devices

Houston, TX
June 2005

Profile/Skills

- ❖ Interdisciplinary research experience in fields of physics, chemistry, biology, medicine, electrical engineering, and computer science (bioinformatics/statistical inference).
- ❖ Spearheaded and completed collaborative project between MIT and Harvard Medical School. Demonstrated novel cancer treatment approach using semiconductor quantum dots. Nanoparticle optimizes transport into solid tumors using a multistage delivery system.
- ❖ Research experience in nanomaterials characterization, optical spectroscopy, electrical device characterization, and wet lab synthesis.
- ❖ Instrument Experience: (High Resolution) Transmission Electron Microscopy (4 yrs), Scanning Electron Microscopy, Semiconductor Parameter Analyzer, FTIR, ICP-AES, X-ray Photoelectron Spectroscopy, High Pressure Liquid Chromatography (4 yrs), and more.
- ❖ Computer Skills: Matlab (9 yrs), Mathematica (8 yrs), Java (3 yrs), C (3yrs), Perl, ImageJ, Unix, Illustrator, Photoshop, and AutoCAD.
- ❖ 2010 MIT 100K Elevator Pitch Contest Finalist
- ❖ Languages: Fluent in English & Cantonese Chinese

Experience

- ❖ Nov 2005-Sept 2010 **Graduate Researcher**
 - Mounji Bawendi Laboratory, Chemistry Department, MIT
 - Electrically controlled growth of CdSe semiconductor nanowires for *in situ* device fabrication. Technique aims to combine the complexity achievable with top-down lithographic patterning methods with the highly parallel and inexpensive bottom-up growth/assembly of nanocomponents
 - Designed, synthesized, and characterized Multi-Stage Nanoparticle Delivery System based on quantum dots for enhanced accumulation in solid tumors and deep penetration (increase diffusion) into tumor tissues. Project required a broad range of skills in physical characterization, wet lab chemistry, and image analysis to quantify the nanoparticles' unique diffusive transport properties.
 - Collaborated with world-renowned cancer researchers at Harvard Medical School/Massachusetts General Hospital for live animal experiments utilizing intravital multiphoton microscopy.
 - HPLC equipment steward: 2 years at Institute for Soldier Nanotechnologies at MIT & 2 years at Mounji Bawendi Lab, trained over 40 students and postdocs for proper use of instrument, performed system maintenance and repair.
- ❖ August 2005-December 2006 **Teaching Assistant**
 - Chemistry Department, MIT
 - TA for Graduate Level Quantum Mechanics and Advanced Undergraduate Physical Chemistry Laboratory. Responsibilities included holding tutorial sessions, conducting office hours, grading problem sets, and preparing solutions for problem sets.
- ❖ Summer 2003, January 2004-June 2005 **Undergraduate Researcher**
 - Junichiro Kono Laboratory, Applied Physics and Electrical Engineering Department, Rice University
 - Optical Modulation Spectroscopy of Carbon Nanotubes and Quantum Wells. Used pump laser to modulate population of excited charge carriers while probing intrasubband transitions using FTIR
 - Designed single-shot autocorrelator for detecting pulse-front tilt in ultrafast laser pulses (AutoCAD)

- ❖ Jan 2002-September 2003 **Undergraduate Researcher**
 - James Tour Laboratory, Chemistry Department, Rice University
 - Molecular Electronics Research. Organic synthesis of molecular device candidates and device characterization using probe station and semiconductor parameter analyzer.

Activities

Public Speaking (MIT Toastmasters), Treasurer for MIT Hong Kong Student Society, Meditation and Yoga (MIT Art of Living)

Publications

Wong CR, Stylianopoulos T, Cui J, Martin J, Chauhan VP, Jiang W, Popovic Z, Jain RK, Fukumura D, Bawendi MG. Multistage Nanoparticle Delivery System Demonstrates Deep Penetration into Tumor Tissue through MMP-activated Size Change. (submitted).

Popovic Z, Liu W, Chauhan VP, Lee J, Wong CR, Greytak AB, Insin N, Nocera D, Fukumura D, Jain RK, Bawendi MG. A Nanoparticle Size Series for *in vivo* Fluorescence Imaging. *Angewandte Chemie International Edition* 2010, **46**: 8649–8652.

Liu W, Greytak AB, Lee J, Wong CR, Park J, Marshall LF, Jiang W, Curtin PN, Ting AY, Nocera DG, Fukumura D, Jain RK and Bawendi. Compact Biocompatible Quantum Dots via RAFT-Mediated Synthesis of Imidazole-Based Random Copolymer Ligand. *Journal of the American Chemical Society* 2009, **132**: 472-483.

Dorn A, Wong CR, Bawendi MG. Electrically Controlled Catalytic Nanowire Growth from Solution. *Advanced Materials* 2009, **21**: 3479.

Patents

U.S. Patent Application Number: 2010/0148152, Electrically Controlled Catalytic Nanowire Growth
Co-inventors: August Dorn, Mounqi Bawendi
Filing Date: 2/12/09

U.S. Patent Number: 2009/0016962, Compositions and Methods for the Treatment of Cancer
(being added as co-inventor)
Co-inventors: Dai Fukumura, Lance L. Munn, Rakesh K. Jain, Triantafyllos Stylianopoulos, Mounqi Bawendi
Pub. Date: 1/15/09

Acknowledgements

I am very fortunate and grateful for the opportunity to study at the MIT Department of Chemistry under Prof. Mounqi Bawendi. Working in Mounqi's group has exposed me to an incredibly broad range of knowledge and skills. It's a pleasure and privilege to work with someone as brilliant, composed, and caring as Mounqi. He provided us with a stable environment to conduct research and grow as scientists.

I wish to thank the physical, emotional, and mental support from fellow Bawendi group labmates: August, Jorge, Jing, Ou, Jie, David S, Euan, Juwell, Jian, Liang-Yi, Raoul, Gyu Weon, Daniel, Russ, JM, Jenn, Jose, Hee-Sun, Numpon, Scott, Lisa, Brian, Darcy, He Wei, Tara, Peter, Andrew, Wenhao, Jongnam, Zoran, Katie, Gautham, Juan, John H, Hao, Binil, Jean-Michael, David O., Venda, Xavier, Yinthai, and Preston. I also wish to thank Li Miao for her administrative support and sharing a bit of her life with me each Thursday as I wait outside Mounqi's office. I need to specifically acknowledge August, Jian, Juwell, and Zoran for their help/collaboration with the projects discussed in this thesis. I want to thank my officemates Juwell and Tara for making our office a center of intellectual discussions, creative brainstorming, and outrageous insanity. I thank Yinthai for teaching me how to make QDs, work with silica sol-gels, and give me guidance throughout the grad school process. I also can't forget the brutal Street Fighter tournaments of Blanka vs. Zangief with Gautham. READY, Fight!

I am grateful we have such incredible collaborators at MGH led by Prof. Dai Fukumura and Prof. Rakesh Jain. Dai came up with the idea for the size-changing "smart" nanoparticle project which became the bulk of this thesis. The exciting data from animal experiments came from work done by the very talented postdocs and grad students at MGH: Fylos, John Martin, Vikash, and Wen Jiang. I had a great time working with and learning from them.

My work at MIT would not be possible without the abundant resources on campus provided by the ISN, CMSE, DCIF, and Koch Institute. In addition, the great classes taught by MIT faculty were of great help. These classes opened my eyes to the world of biology/medicine and sparked my interest through the faculties' passion for their research.

I wish to thank my family, especially my mother and grandmother, for their love and hard work to provide me the opportunity to get the best education available. And I thank to the highest degree the mentors and advisors who inspired me to pursue a career in science including Prof. James Tour, Prof. Jun Kono, Prof. Jake Ciscek, Dr. Diane Larrabee, and Prof. Jigang Wang.